

UNIVERSITÀ DEGLI STUDI DI PARMA  
FACOLTÀ DI SCIENZE MATEMATICHE, FISICHE E NATURALI

DOTTORATO DI RICERCA IN FISICA – XIII CICLO

SPIN-POLARIZED EPITHERMAL MUONS:  
CONSTRUCTION AND TEST OF A PULSED SOURCE  
WITH APPLICATIONS TO FILMS AND NANOSTRUCTURES

TONI SHIROKA

ANNO ACCADEMICO 1999-2000





UNIVERSITÀ DEGLI STUDI DI PARMA  
FACOLTÀ DI SCIENZE MATEMATICHE, FISICHE E NATURALI

DOTTORATO DI RICERCA IN FISICA  
XIII CICLO

**Spin-polarized Epithermal Muons:  
Construction and Test of a Pulsed Source  
with Applications to Films and Nanostructures**

Supervisor: Prof. CESARE BUCCI  
Prof. ROBERTO DE RENZI

Candidato: TONI SHIROKA

ANNO ACCADEMICO 1999-2000

This document was typeset in Adobe® Utopia and Computer Modern Roman  
by the author using the L<sup>A</sup>T<sub>E</sub>X2<sub>ε</sub> software.  
The file in Portable Document Format was generated with pdfT<sub>E</sub>X version 13c.

---

© Copyright 2000 by Toni Shiroka. All Rights Reserved.

AUTHOR'S ADDRESS

Toni Shiroka  
Dipartimento di Fisica  
Università degli Studi di Parma  
Parco Area delle Scienze 7A, I-43100 Parma, Italy  
E-MAIL: [shiroka@fis.unipr.it](mailto:shiroka@fis.unipr.it)  
URL: <http://www.fis.unipr.it/~toni>

## ABSTRACT

THE most recent advances in the physics of low-dimensionality systems have been accompanied by the need for new methods of investigation or the extension of the existing ones. The muon ( $\mu^+$ ) is proven to be an excellent magnetic probe of matter and the Muon Spin Rotation ( $\mu$ SR) a good tool, complementary to NMR or neutron scattering. However the *surface muons*, characterised by a mean *range* of  $\sim 150$  mg/cm<sup>2</sup>, with a typical *straggling* of  $\sim 20$  mg/cm<sup>2</sup>, are suitable for bulk studies only.

The challenge offered by the study of thin films, surfaces, interfaces and nanomaterials has motivated the efforts to extend the potentialities of the  $\mu$ SR method to the low energy range. Thus, at the Rutherford Appleton Laboratory (RAL), Chilton, UK, a new pulsed source of slow polarised muons has been developed, using the so-called *moderator technique*. It relies on the particular mechanisms of thermalisation that charged particles undergo in van der Waals insulators, as e.g. Ar or N<sub>2</sub>, characterised by considerable electronic gaps ( $E_g \sim 10$  eV) and at the same time by low phonon frequencies ( $\hbar\omega \sim 5$  meV).

The slow (or epithermal) muon beam, tunable in the energy range from several eV to 20 keV, is generated when surface muons with a momentum of 26.5 MeV/c are moderated in a 100 nm layer of frozen rare gas deposited over an aluminium substrate at 7 K.

Measurements of moderation efficiencies in case of films of frozen Ar, Kr, Xe, N<sub>2</sub> and CO<sub>2</sub> gases as well as with bare diamond and aluminium substrates, have shown that argon is the best moderator with an efficiency of  $10^{-5}$  relative to the incoming particles.

The initial energy distribution of slow muons, measured by applying retarding potentials to the substrate, gives a FWHM of 25 eV in case Ar and of 55 eV for N<sub>2</sub> moderators. It displays a constant behaviour within the band gap energy of the moderator followed by an exponential decrease. The measured dependence of moderation efficiency on film thickness shows a modest peak around 100 nm.

Thanks to the pulsed feature, the implantation time is automatically determined which, together with the possibility of energy tuning, have permitted the first successful applications of the epithermal muon beam. Thus, slicing experiments across a 20 nm copper film on quartz substrate, have evidenced a 2 nm copper oxide surface layer. Other preliminary experiments on a hexagonal cobalt film have suggested the existence of muon precession in the local magnetic field.

Taking advantage of the pulsed nature of the ISIS facility we have also developed two new methods dedicated to future LE- $\mu$ SR experiments. They rely on the possibility to apply external magnetic field, synchronous to the muon pulse and as short as 20  $\mu$ s. The external pulsed magnetic field and/or field gradient are generated by a laminar current-loop method. Whereas field gradients seem more appropriate for a straightforward imaging of the implantation depth of positive muons in metals, the pulsed uniform magnetic fields are shown suitable for the direct measurement of the sudden-to-adiabatic cross-over. The latter method is also expected to be applicable to the study of the delayed muonium formation.

## RIASSUNTO

I più recenti sviluppi nella fisica dei sistemi a bassa dimensionalità hanno messo in luce sia la necessità di nuovi metodi d'indagine che l'ampliamento di quelli già esistenti. Il muone ( $\mu^+$ ) si è rivelato un'eccellente sonda magnetica della materia e la tecnica di Muon Spin Rotation ( $\mu$ SR) uno strumento utile, complementare al NMR e allo scattering neutronico. Tuttavia, i cosiddetti muoni di "superficie", caratterizzati da percorsi medi (*range*) di  $\sim 150$  mg/cm<sup>2</sup>, con sparpagliamenti (*straggling*) tipici di  $\sim 20$  mg/cm<sup>2</sup>, sono appropriati solo per studi delle proprietà del *bulk*.

La sfida posta dallo studio di film sottili, superfici, interfacce e nanomateriali ha motivato notevoli sforzi, aventi come scopo l'estensione della tecnica  $\mu$ SR anche nell'ambito delle basse energie. Così al Rutherford Appleton Laboratory (RAL), Chilton, UK, una nuova sorgente pulsata di muoni lenti polarizzati è stata sviluppata utilizzando la *tecnica del moderatore*. Essa sfrutta i particolari meccanismi di termalizzazione che le particelle cariche subiscono negli isolanti di van der Waals (tipicamente Ar o N<sub>2</sub>), caratterizzati sia da rilevanti gap elettronici ( $E_g \sim 10$  eV) che da basse frequenze fononiche ( $\hbar\omega \sim 5$  meV).

Il fascio di muoni lenti (o epitermici), con energia accordabile da alcuni eV fino a 20 keV, viene generato quando i muoni di superficie aventi un momento di 26.5 MeV/c sono moderati in uno strato di 100 nm di gas nobile depositato su un substrato di alluminio a circa 7 K.

Misure di efficienze di moderazione su film di Ar, Kr, Xe, N<sub>2</sub> e CO<sub>2</sub> solidi, così come su alluminio o diamante puro, hanno mostrato che l'efficienza massima di  $10^{-5}$  muoni lenti per particella incidente, si ottiene utilizzando l'argon come moderatore.

La distribuzione iniziale di energia dei muoni lenti, misurata applicando potenziali ritardanti al substrato, fornisce un valore di 25 eV (FWHM) per Ar e di 55 eV per N<sub>2</sub>. Essa mostra un andamento costante entro il gap energetico del moderatore, seguita da un decremento esponenziale. La misura dell'efficienza di moderazione al variare dello spessore del moderatore stesso sembra invece mostrare un lieve massimo attorno ai 100 nm.

La natura pulsata del fascio permette la rilevazione automatica del tempo d'impiantazione. Ciò, assieme alla possibilità di accordare l'energia, hanno permesso le prime applicazioni del fascio di muoni epitermici. Così esperimenti di scansione su un film di 20 nm di rame su quarzo, hanno dimostrato la presenza di uno strato superficiale di 2 nm di ossido di rame. Altri esperimenti preliminari hanno rilevato la precessione dei muoni nel campo magnetico locale in un film di cobalto esagonale.

Due nuovi metodi, dedicati a esperimenti futuri di LE- $\mu$ SR, sono stati sviluppati sfruttando la natura pulsata del fascio di ISIS. Essi si basano sulla possibilità di applicare campi magnetici esterni di breve durata (20  $\mu$ s), in sincronia con l'arrivo del fascio di muoni. Sia i campi che i gradienti di campo sono generati ricorrendo ad una spira piatta dove scorre una corrente laminare pulsata. I gradienti si sono rivelati più appropriati per l'*imaging* immediato delle profondità d'impiantazione dei muoni nei metalli, mentre il campo pulsato si è mostrato uno strumento interessante per lo studio del passaggio dal regime adiabatico a quello improvviso. L'ultimo metodo potrebbe inoltre essere utilizzato per lo studio della formazione ritardata del muonio.

# Contents

<b>1</b>	<b>Introduction</b>	<b>1</b>
1.1	Overview of muon physics . . . . .	1
1.2	Scope and purpose of present thesis . . . . .	3
<b>I</b>	<b>Generation, properties and experiments with epithermal muons</b>	<b>9</b>
<b>2</b>	<b>Muon properties and experimental techniques</b>	<b>10</b>
2.1	Properties of muon . . . . .	10
2.1.1	Un peu d’histoire . . . . .	10
2.1.2	Main properties of muon . . . . .	11
2.2	Muon decay . . . . .	13
2.3	Production of spin polarised muon beams . . . . .	16
2.4	Basics of Muon Spin Rotation . . . . .	18
2.5	$\mu$ SR vs. NMR . . . . .	24
<b>3</b>	<b>Low energy muons: Production, transport and detection</b>	<b>27</b>
3.1	Techniques to generate low energetic muons . . . . .	27
3.2	Generation of LE muons at ISIS . . . . .	34
3.2.1	The DevA beam area . . . . .	34
3.2.2	The pulsed epithermal muon beam line . . . . .	37
3.2.2.1	General UHV and temperature requirements . . . . .	40
3.2.2.2	Slow muon generation target . . . . .	42
3.2.2.3	High voltage focusing and transport . . . . .	45
3.2.2.4	Experimental station for LE- $\mu$ SR Studies . . . . .	48
3.2.2.5	Electronics and Data Acquisition System . . . . .	52
<b>4</b>	<b>Properties of the pulsed low energy muon source</b>	<b>55</b>
4.1	Beam spot size and slow muon yield . . . . .	55
4.2	Efficiency dependence on temperature and pressure . . . . .	58
4.2.1	Deposition temperature dependence . . . . .	59
4.2.2	Efficiency dependence on heat treatment . . . . .	59
4.2.3	Surface adsorbates and film ageing properties . . . . .	62
4.2.4	Efficiency dependence on pressure . . . . .	63
4.3	Energy distribution of slow muons . . . . .	65
4.4	Efficiency dependence on film thickness and escape depth . . . . .	67
4.5	Efficiency dependence on moderating material . . . . .	69
4.6	Theoretical overview of muon moderation processes . . . . .	70

4.6.1	Stopping processes for low energy muons . . . . .	70
4.6.2	Solid rare gases as muon moderators . . . . .	74
<b>5</b>	<b>Experiments on thin films using epithermal muons</b>	<b>76</b>
5.1	Implantation profile of epithermal muons . . . . .	76
5.2	Investigations on magnetic thin films . . . . .	82
<b>II</b>	<b>Developments dedicated to low energy <math>\mu</math>SR</b>	<b>86</b>
<b>6</b>	<b>Projected Range Imaging (PRI)</b>	<b>87</b>
6.1	Introduction . . . . .	87
6.2	Principles of the PRI method . . . . .	91
6.2.1	Magnetic field gradients in metallic films . . . . .	92
6.3	Experimental Results . . . . .	93
6.3.1	Range measurements by conventional methods . . . . .	95
6.3.2	PRI results on Al, Cu and Pb . . . . .	97
6.3.3	Notes on thin films . . . . .	100
6.4	Conclusions . . . . .	101
<b>7</b>	<b>Muons in pulsed magnetic fields</b>	<b>103</b>
7.1	Introduction . . . . .	103
7.2	Analytical aspects of the adiabatic transition . . . . .	105
7.3	Experimental details . . . . .	108
7.4	Measurements and data analysis . . . . .	111
7.5	Discussion and conclusions . . . . .	116
<b>8</b>	<b>Conclusions and outlook</b>	<b>118</b>
<b>A</b>	<b>Energies in pion and muon decays</b>	<b>120</b>
A.1	Maximum energy for decay positrons . . . . .	120
A.2	Energy of surface muons . . . . .	121
A.3	Energy threshold for single pion production . . . . .	121
<b>B</b>	<b>Some formulae for the fits</b>	<b>123</b>
	<b>Acknowledgements</b>	<b>135</b>

# Chapter 1

## Introduction

### 1.1 Overview of muon physics

THE development and the continuous extension of the different branches of physics has given rise to an ever growing number of intersections and therefore to the birth of truly cross-disciplinary research areas. Muon Science is such a field, which can be located at the borders of elementary particle, nuclear and solid state physics research.

Since the muon discovery in cosmic rays in 1937 by Kunze [74], continuing with the early studies in 1957 by Garwin, Lederman and Weinrich [49], which fully realised its considerable potential as a probe particle, the muon has played an important role in our understanding of nature. Extensive studies have been carried out to determine the muon properties and interactions, but at the same time it has also been used as a probe to reveal the nature of other particles and systems.

As for the first type of research, namely that which has the muon as its *object* of study, it was this heavy lepton to give us the first indication that nature replicates particles in a similar pattern, now known as generations. Yet, the existence of generations still persists as a big mystery after over 50 years, so that the famous question of I. Rabi “Who ordered that?”, related to the muon, still sounds topical.

Nevertheless, the muon as a heavy lepton has been a tool of primary importance in searches for new physics at *low energies*. All-leptonic systems like the muonium ( $\text{Mu} \equiv \mu^+e^-$ ) have offered unrivalled opportunities for precision measurements of fundamental constants. The determination of the ground state hyperfine structure splitting, that of the  $1s-2s$  level separation of muonium and of the anomalous magnetic moment of the muon, together with searches for rare particle decays, not included in the standard model, have been among the main interests in this area of elementary particle physics.

There is a renewed interest in basic muon physics, also in the *high energy* range, since physicists have been seriously considering the design and construction of a muon collider,

which once completed, will potentially become a ‘‘Higgs Factory’’, as well as will achieve a much higher collision energy than all of the existing electron colliders.

Regarding the second type of research, that which uses the muon as an investigative *tool*, with its  $\sim 2.2 \mu\text{s}$  mean lifetime (one of the longest of all the unstable elementary particles), the muon is among those few ‘‘exotic’’ particles to have found a relevant place in condensed matter physics. This very special status of the muon can be traced back to two classical violations of the parity invariance which take place during its production and decay, leading respectively to a very large *spin polarisation* and to a *direct correlation* between muon spin and that of his decay positron.

Apart from its intrinsic properties, the use of muons depends of course also on the availability of intense, highly polarised muon sources. One of these is the ISIS Pulsed Muon Facility at RAL (Rutherford Appleton Laboratory) located near Oxford (UK), where all the experiments described in this thesis were performed<sup>1</sup>.

Implanted muon studies have shed new light on problems in condensed matter physics, including those concerning magnetism, superconductors, semiconductors and quantum diffusion<sup>2</sup>.

The main experimental technique that uses muons as probe particles is called with the acronym  $\mu\text{SR}$ , which stands for *Muon Spin Rotation/Relaxation/Resonance* where the most appropriate *R* is used, depending on which of these three variants is employed. The basic idea of all of them consists in following the muon spin evolution in time, which will depend both on the internal (microscopic) and on the external (macroscopic) magnetic field distribution, thanks to the detection of the flux of decay positrons.

A key difference between this technique and those involving neutrons and X-rays is that scattering is not involved. Neutron diffraction methods use the change in energy and/or momentum of a scattered neutron to infer details about a particular sample. In contrast muons are implanted into a sample and reside there for the rest of their lives.

Besides the use of the muon as an accurate microscopic magnetometer, revealing the distribution and fluctuations of magnetic and hyperfine fields, a vast class of  $\mu\text{SR}$  studies rely on the muon’s lighter mass compared to that of the proton.

In semiconductors, virtually all that is known about the crystallographic location and local electronic structure of isolated hydrogen defect centers comes from studies of muonium.

The similarity between the positive muon and the proton is exploited also in a large number of muon diffusion studies, where it provides a good isotope test for the models describing the hydrogen behaviour in metals.

---

<sup>1</sup>For a complete list of muon facilities around the world, their type, energy, luminosity, etc. see e.g. [27] or, for an updated listing, the online version [150].

<sup>2</sup>A simple introduction about the use of muons in these research fields is given in reference [13].

Finally, there is a whole field of studies called muonium chemistry, in which one takes advantage of the unique capability to follow the history of the implanted muons up to their final state, to study radicals, catalytic processes or to characterise adsorbates.

## 1.2 Scope and purpose of present thesis

A big step forward in muon science was the discovery of the so-called *surface muons* originating from pions which decay at rest at the surface of the production target [16]. Muons generated through this technique have a *minimum* energy of  $\simeq 4.12$  MeV to which corresponds a momentum of 28 MeV/c. They offer decisive advantages over decay-in-flight muons including high degree of polarisation, high stopping rates and limited penetration depths (a fraction of a millimetre to 1 mm equivalent to 150 mg/cm<sup>2</sup>) [96, 95].

Although quite convenient in exploring the bulk properties of matter, the surface muons are not suitable for the study of surfaces, interfaces and thin films, mainly because of their still high kinetic energy and of the relevant range straggling. This should be clear from the following table, where typical values of the range and straggling (e.g. in glass) are shown as a function of muon energy, with the last line referring to surface muons:

<b>Energy (<math>E_k</math>)</b>		<b>Range (<math>R</math>)</b>		<b>Straggling (<math>\Delta R</math>)</b>	
[eV]	10.0	[Å]	5	[Å]	3
	100.0		21		13
[keV]	1.0	[nm]	13.1	[nm]	5.4
	10.0		75.0		18.0
	30.0		244.0		36.0
[MeV]	4.1	[ $\mu m$ ]	710	[ $\mu m$ ]	100

**Table 1:** Muon range and straggling as a function of kinetic energy.

The development of a tunable slow muon beam with an energy ranging from a few eV to several keV will advance the  $\mu$ SR technique by providing a new investigative tool to the growing field of thin film and surface physics, as well as to the high precision and fundamental physics experiments. Below we enumerate some of the possible applications of slow muons:

- A low energy muon beam is among the most appropriate tools for studies of surfaces, solid interfaces and thin films. These investigations are expected to shed new light into the complex phenomena taking place at these “sites”, important both for the pure research as well as for the applied physics.

- The study of fundamental processes in atomic physics including the ionisation, the diffusion, the electron capture and the energy loss in matter. Muon data, when compared to those available for protons will allow the analysis of variation of cross sections for different particle masses and scaled velocities. This is quite an important test for the theoretical models describing these phenomena, especially in the low energy range, where there is a considerable lack of experimental data.
- Slow muons passing through a thin foil or gas target are neutralised with large probability and hence generate a muonium beam. At these low energies, the muonium atoms are formed mainly in excited states, like e.g. in the  $2s$  state, which is a preferred system for high precision tests of quantum electrodynamics (QED) since, due to the absence of hadronic corrections, a direct comparison with theoretical calculations is possible.
- The possibility to vary the muon implantation energy allows to perform delicate *depth slicing* experiments related to the magnetic flux penetration in type II superconductors, like probing the internal field distribution as a function of depth below the surface of a superconductor [61], or more generally will enhance the systematic study of the interplay between magnetism and superconductivity both in ceramics and intermetallic materials.
- Closely related to the previous point is the study of magnetically ordered surfaces. This could be achieved by delivering a narrow low energy  $\mu^+$  beam at a grazing angle, in quite a similar fashion to an analogous technique which uses deuterium. For antiparallel electronic spin ordering, half of the muonium atoms (if present) are formed in a triplet state and half in a singlet state, which is promptly depolarised due to the hyperfine interaction. In case of parallel electronic spins instead, the muonium will be formed in triplet states only, which therefore retain the initial spin polarisation. As a consequence, a measure of muon polarisation could give information about the electronic spin ordering in the sample [93].
- The chemistry of surfaces, the catalysis and the dynamics of the impurities also could be investigated by the standard use of muonium as a light isotope of hydrogen.

Part of the work described in this thesis was done within the framework of a project for the development of a slow muon beam at the ISIS pulsed muon facility (RAL). This project started in 1996 and involved an international collaboration among the Rutherford Appleton Laboratory and the universities of Heidelberg, Parma, Stuttgart and University College London. In the relevant chapters, reference and acknowledgement to written reports and thesis concerning collaborative work and findings, are given.

The epithermal muons may be generated through different approaches, but the less complex and, at the same time the most promising one, seems to be the so called *moderator technique*. It closely follows analogous techniques [55,88], widely used to produce low energy positrons, and can provide slow muons with an efficiency up to  $\sim 10^{-4}$ – $10^{-5}$ .

At ISIS the generation of the epithermal muon beam<sup>3</sup> was achieved by using cryogenic films of rare gas solids (typically Ar) or solid N<sub>2</sub>, which exhibit the highest efficiencies among the known moderators [57,56]. The superior moderation properties of these van der Waals solids, characterised both by considerable electronic gaps ( $E_g \sim 10$  eV) as well as by low phonon frequencies ( $\hbar\omega \sim 5$  meV), is supposed to be due to the particular mechanisms of thermalisation of charged particles in them.

By taking into account the available rate of surface muons at ISIS ( $\sim 4 \cdot 10^5 \mu^+ / s$  [39]), the moderation yields a few epithermal muons per second which, although not adequate for a permanently installed slow muon source, were sufficient for performing preliminary experiments and also for demonstrating some applications. This was made possible firstly because of the intrinsically low background and secondly because of the pulsed beam structure.

Indeed, in doing  $\mu$ SR the availability of a trigger signal is crucial to correlate the arrival time of a slow muon with its decay time. The pulsed character of the ISIS facility automatically provides this signal through its narrow time-structure (82 ns FWHM pulse width), therefore allowing for a slow muon source which will retain its initial narrow energy distribution. This is a key feature of a pulsed beam and constitutes its main advantage over a continuous slow muon beam, because experiments where muons can be stopped within a few (top) atomic layers of a given sample are possible and, by an additional electrostatic acceleration, delicate *depth slicing* investigations can be performed.

In fact, at the other slow muon source at PSI<sup>4</sup>, also based on frozen rare gas moderators, the intrinsic lack of a triggering signal is solved by the insertion, into the continuous muon beam, of a very thin carbon foil ( $\sim 3.3 \mu\text{g}/\text{cm}^2$ ) to detect the incoming muons via secondary electrons. This however, gives rise to a  $\sim 0.5$  keV decrease in the energy resolution of the 16 keV muon beam and to a simultaneous increase in the background level, due to muonium formation in the trigger detector [94]. On the other hand, while this approach destroys the initial energy bandwidth of 25 eV FWHM, it gives a more accurate timing resolution as compared to that obtained at ISIS, which is limited by the finite pulse width. In some sense the two facilities should be regarded as complementary to each other.

As can be seen from a quick inspection of the contents, this thesis consists essentially of two parts which are related to each other by sharing the same central topic, the generation

---

<sup>3</sup>Here the terms epithermal and slow muons are used as synonyms. For a brief description of the terminology used to describe these beams according to their energy ranges, see for example the page 344 of [95].

<sup>4</sup>Paul Scherrer Institut, Villigen, Switzerland.

and use of slow muons. In the first part of the thesis, regarding the collaborative work, we discuss the design, construction and testing of the apparatus for the generation of slow muons at ISIS, and also some of the experiments performed using the newly developed beam.

The second part instead describes an autonomous work, mainly related with the possible future applications of slow muons. The experiments which led to the development of two new measurement methods, were performed by using “normal” surface muons. Since the motivation and the ideas dealt with in the first part were explained somewhat in detail, let us now give a brief outline of the concepts involved in the second one.

As was pointed out above, the mapping of the epithermal muon implantation profile is of great practical and theoretical value. However, the method actually used for measuring the range of surface muons, namely that of the variable degrader, would fail in case of slow muons due to the large straggling introduced by the degrader itself. This problem was solved by introducing a *new* method of measurement named PRI (*Projected Range Imaging*), which allows the study of the range curves in metallic films in a “single shot” experiment, by making use of *magnetic field gradients*. These latter were generated by a laminar current-loop, where the loop itself serves as the object of measurement due to the high field gradient which are established in it.

A remarkable feature of the current loop device, which takes full advantage of the pulsed nature of the polarised source of muons, is the possibility to apply the external fields, synchronous to the muon pulse arrival, with a duration as short as a few muon’s life-times ( $\sim 20 \mu\text{s}$ ). This, apart from greatly reducing the thermal dissipation due to the significant narrowing of the duty cycle, opens the way for another type of applications.

Namely, one can make use of the *uniform magnetic field* created in the air gap between the two current carrying loops, where a thin sample can be positioned. The time evolution of the muon spins, both as free muons and as muonium, can therefore be studied in response to the pulsed magnetic field with two interesting consequences:

a) An appropriate delay in the application of the pulsed field, can significantly extend the intrinsic frequency bandwidth (6.2 MHz at ISIS) due to the finite muon pulse width.

b) Moreover, the joint application of the pulsed and of a steady magnetic field allows the detection of transition between two precession regimes: sudden and adiabatic. In this case, the adiabatic cross-over is observed just by scanning the longitudinal static field. This latter method is expected to be applicable to the experimental study of the muonium-radicals and to the “delayed” muonium formation.

In closing this introductory chapter we describe the structure of the present work. The first part, related to the generation of epithermal muons and experimental measurements with them, begins with chapter 2, where we introduce the muon properties and the basic concepts of the  $\mu\text{SR}$  technique.

An overview of the different approaches to the problem of muon moderation is given in chapter 3. Next we focus the attention on the moderator technique and give a detailed description of the generation of low energy (LE) muons at ISIS.

Chapter 4 is dedicated to the exposition of the properties of the pulsed LE muon beam, including the energy and angular distribution of slow muons, the beam polarisation and the dependence of moderation efficiency from temperature and pressure. This chapter closes with an account on theoretical aspects of muon moderation.

The following chapter 5 focuses on the experimental measurements performed with epithermal muons. Here, after a description of the procedures used to characterise our samples, including X-ray diffractometry, AFM microscopy, etc., two significant examples are reported. One concerns slicing experiments across a 20 nm copper film on quartz substrate with evidence for a 2 nm copper oxide surface layer. The other is a preliminary experiment on a hexagonal cobalt film which suggested the existence of muon precession in the local magnetic field.

The second part describes two possible  $\mu$ SR developments dedicated to LE- $\mu$ SR.

It starts with chapter 6, where the problem of measuring range and straggling of muons in matter is introduced. The main ideas involved in the generation of a pulsed magnetic field, together with its practical implementation are explained in this chapter. Then we continue with the first application i.e. the projected range imaging method and present the results obtained in some metallic samples.

Chapter 7 deals with the narrowly confined pulsed magnetic fields and the problem of the sudden-to-adiabatic cross-over. The experiments carried out by appropriately delaying the pulsed magnetic field are also discussed. Possible applications to studies of delayed muonium formation are envisaged.

In the last chapter (chapter 8), the most significant results of the present work are summarised and some possible future developments are suggested.

Finally, in the appendices various calculations are carried out in detail. In appendix A some formulas involving energetic relationships during decays are inferred. Furthermore, in appendix B the formula used to perform the fits of straggling data is deduced.



## Part I

# Generation, properties and experimental measurements with epithermal muons

## Chapter 2

# Muon properties and the $\mu$ SR experimental technique

THIS chapter is intended as an introduction to the basic concepts of  $\mu$ SR, so we begin by giving some definitions and by explaining the basic techniques used when performing experiments with muons. Since several excellent general references are available in the literature [27, 32, 124, 125], the reader is referred to them for a more detailed account on the various aspects of this technique.

### 2.1 Properties of muon

#### 2.1.1 Un peu d'histoire<sup>1</sup>

The discovery of muon by Kunze in 1933 [74], in the tracks of a Wilson cloud chamber exposed to cosmic rays, went almost unobserved, perhaps because the origin of the tracks was completely unknown nor had such a particle been suggested yet by any theory.

The experiments by Neddermeyer and Anderson [102] four years later confirmed the existence of the new particle, but the closeness of its mass to that of the pion, theoretically predicted by Yukawa [157] as the carrier of the strong interaction, made them mistake the true identity of muons.

Finally, they were Powell and collaborators in 1947 [77] who, by direct experimental verification of pion decay into the non strongly interacting muon, ultimately determined its identity as a lepton.

However it was only tens years later, in 1957, that muon spin rotation technique was born. In experiments to establish the violation of parity conservation during muon decay Garwin

---

<sup>1</sup>For a broader historical overview including also possible future developments in muon science, refer to the excellent online resource [20]. See also [24] for reprints of some of the original papers.

et al. suggested that it was just the parity non-conservation that might furnish a sensitive general-purpose probe of matter, hence opening the way for the modern  $\mu$ SR science.

The work in the successive twenty years, dedicated mainly to the rigorous testing of quantum electrodynamics, was useful for producing the basic experimental apparatus and techniques needed to perform the first  $\mu$ SR experiments. But, more importantly, it generated an ever increasing interest in the unavoidable environmental effects which influenced the fundamental measurements. In fact, quite quickly scientists realised that these secondary effects were interesting areas of study in their own right, for which the muon was either the best or the only available probe.

In the seventieth the  $\mu$ SR research received a major boost with the construction of a number of dedicated intermediate-energy accelerators known as “meson factories”. These facilities with their high-intensity muon fluxes are now systematically used in the current research. In future other, even more intense, muon beams will allow new, sophisticated type of experiments to be carried out, which are supposed to deepen our current understanding on structure of matter.

In conclusion of this short historical overview one must say that “while the properties of the muon have been well established, why many of these are what they are still remains a mystery” [40]. However, this has not prevented the physicists from successfully using the muons as a tool in materials science and in fundamental studies.

### 2.1.2 Main properties of muon

Electrons ( $e^-$ ), muons ( $\mu^-$ ), taus ( $\tau^-$ ) and the accompanying neutrinos ( $\nu_e, \nu_\mu, \nu_\tau$ ), together with the respective anti-particles make up the class of leptons, which are all unaffected by the strong interactions [30, 65]. The modern Standard Model theory [30] considers muons, together with the muonic neutrinos and the strange and charmed quarks to form the second generation of fundamental fermions.

For leptons no internal structure is known so far. Scattering experiments have established that charged leptons behave like point-like particles down to dimensions of  $10^{-18}$  m [83, 84]. Purely leptonic hydrogen-like systems like muonium ( $\text{Mu} \equiv \mu^+ e^-$ ) offer therefore a unique opportunity for precision experiments to investigate bound state QED without the complications arising from nuclear structure [60]. The aim of these experiments is to search for deviations from present models and to test fundamental symmetry laws like that of electron–muon universality, which is assumed in the QED theory (see [73] for a recent review).

Since these type of studies are mainly subject of particle physics, we will not delve further into them. In solid state physics on the other hand, muons are used to investigate the properties of matter. Thus, they are used as a research tool rather than being the object of research itself.

Average lifetime	$\tau_\mu = 2.19703(4) \cdot 10^{-6} \text{ s}$
Mass	$m_\mu = 105.65839(34) \text{ MeV}/c^2$ $= 0.113428913(17) \text{ u}$
Charge	$q_\mu = e = 1.60217733(49) \cdot 10^{-19} \text{ C}$
Spin	$J = \frac{1}{2}\hbar$
Magnetic moment	$\mu_\mu = 1.001165923(8)e\hbar/2m_\mu$ $= 3.183347(9)\mu_p$
Gyromagnetic ratio	$\gamma_\mu/2\pi = 13.553420(51) \text{ kHz G}^{-1}$

**Table 2:** Main muon properties [52].

The muon properties are shown in table 2. The muon lifetime of  $2.2 \mu\text{s}$ , is quite long if compared to those of other unstable elementary particles. It allows a relatively wide time window for  $\mu\text{SR}$  studies, during which a sufficient quantity of information can be gathered.

One should note that the mass of the muon is approximately 1/9 of the proton mass and almost 207 times that of the electron. Furthermore, its magnetic moment is about 3.18 times that of the proton but only 0.00484 that of the electron. From these figures it is clear that the intermediate physical properties of the muon induce one to consider it some times as a “light” proton and others as a “heavy” electron [19, 153].

However, it is the first viewpoint which is more appropriate to consider when studying condensed matter with muons. In fact, the behaviour of  $\mu^-$  resembles more that of the electron. Once implanted inside matter, the negative muons will interact through coulombian forces and consequently will be attracted by the nuclei, forming a bound state with them in just  $\simeq 10^{-14} \text{ s}$ . Due to the much larger mass with respect to the electron,  $\mu^-$  finds itself in average 207 times nearer the nucleus than the electron (Bohr radius  $a = n^2\hbar^2/Ze^2m$ ) and thus, by weak interaction with the nucleus, it will promptly decay.

On the other hand, positive muons  $\mu^+$  are repelled by nuclei and usually sit in interstitial sites of the lattice where, under suitable conditions, will catch an electron and form a muonium atom  $\text{Mu} \equiv \mu^+e^-$ . In many respects, the latter is almost identical to a common hydrogen atom. This close resemblance is further clarified if one takes into account that it is the reduced mass to govern most of the formulae used to determine the quantum mechanical characteristics of a hydrogenoid system. Indeed, the reduced masses of H and Mu almost coincide (they differ by less than 0.4%), since both the proton and muon masses are much larger than that of the electron. Positive muons are also easier to produce and use, thus most of the contemporary research is carried out with them. Hence, from now on when speaking about muons it will imply positive muons. Important exceptions are given by e.g. studies on muon catalysed fusion  $\mu\text{CF}$  or those related to muonic nuclear capture, both of which make use of negative muons.

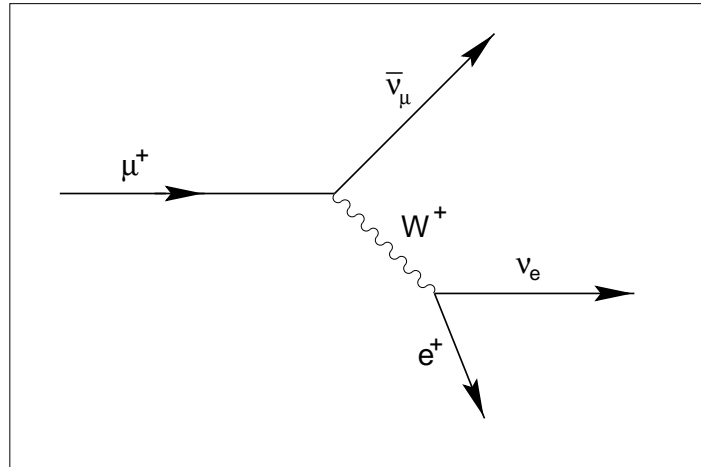


**Figure 1:** Feynman diagram for muon decay.

## 2.2 Muon decay

The use of muons in solid state physics and material science research depends upon the particularity of their production and decay (cfr. section 2.4).

We begin by considering first the muon decay, a purely leptonic weak process with a mean life time  $\tau_\mu = 2.19703(4) \mu\text{s}$ , which gives a positron and two neutrinos according to the well known scheme<sup>2</sup>:

$$\mu^+ \longrightarrow e^+ + \nu_e + \bar{\nu}_\mu \quad (1)$$

The Feynman diagram for the decay is shown in figure 1. Since there are three bodies involved in this decay, it follows that the energy  $E$  of the emitted positrons will continuously span a range going from a minimum of zero up to a maximum of  $E_{\text{max}} = 52.831 \text{ MeV}$  (refer to appendix A for the detailed calculations).

However, the most important fact about muon decay is the presence of a strong *correlation* between muon spin direction and that along which the decay positron is emitted. Let us first try to give a qualitative explanation. The main point is that in weak interactions, because of the parity violation, left-handed particles are coupled only to right-handed antiparticles [82]. Hence, the massless neutrinos will always exhibit a well defined helicity (i.e. their helicity constitutes a “good” quantum number). On the other hand, particles of non-zero mass like the positron, in general may have either type of helicity. At very high energies, though, definite helicities are again privileged, which is just the case of the highly relativistic positrons

<sup>2</sup>Other decays [52] like e.g.  $\mu^+ \longrightarrow e^+ + \nu_e + \bar{\nu}_\mu + \gamma$ , etc. occur with too low a probability and consequently can be safely disregarded for our purposes. Nevertheless, the search for rare and/or forbidden muon decays is of special interest in unified gauge theories because they can provide accurate tests of speculative models, extensions to the present Standard Model.

arising from the muon decay. Since for them  $E_{e^+} \gg m_{e^+}$ , the positron emission will occur preferentially along the muon spin direction.

A more quantitative approach is based on the weak interaction Hamiltonian which has the form of a current–current interaction [53, 125]:

$$\mathcal{H} = \frac{G_F}{\sqrt{2}} j_W \cdot j_W^*, \quad \text{where} \quad \frac{G_F}{(\hbar c)^3} = 1.16 \cdot 10^{-5} \text{ GeV}^{-2}. \quad (2)$$

Here  $G_F$  is the Fermi constant for the weak interaction, whereas  $j_W$  represents the current, which in the V-A picture is given by:

$$j_W = \bar{\psi}_\mu \gamma_\mu (1 + \gamma_5) \psi_{\bar{\nu}_\mu} + \bar{\psi}_e \gamma_\mu (1 + \gamma_5) \psi_{\nu_e}, \quad (3)$$

where  $\psi$  are the spinor wave-function and  $\gamma_\mu$  are the Dirac matrices. From the Fermi golden rule, by integrating over the neutrinos momenta, one can easily find the probability  $dW(\epsilon, \theta)$  that a positron of a given energy  $\epsilon$  will be emitted in a certain direction  $\theta$  with respect to the muon spin direction [53, 107]:

$$\begin{aligned} d^2W &= dW(\epsilon, \theta) d\epsilon d\theta = \\ &= \frac{G_F^2 m_\mu^5}{192 \pi^3} \cdot (3 - 2\epsilon) \epsilon^2 \cdot \left[ 1 + \frac{2\epsilon - 1}{3 - 2\epsilon} \cos \theta \right] d\epsilon d\theta, \end{aligned} \quad (4)$$

where  $\epsilon = E/E_{\text{max}}$  gives the relative positron energy ( $0 \leq \epsilon \leq 1$ ). The asymmetry in the angular distribution can be traced back to the parity violating terms in the interaction Hamiltonian (2). The integration of equation (4) over  $\cos \theta$  alone will give the *energy spectrum*  $W = W(\epsilon)$  of the emitted positrons:

$$W(\epsilon) = dW(\epsilon)/d\epsilon = 2(3 - 2\epsilon)\epsilon^2/\tau_\mu \quad (5)$$

The integration over both  $\epsilon$  and  $\cos \theta$  gives the total decay probability for the muon:

$$W = \frac{1}{\tau_\mu} = \frac{G_F^2 m_\mu^5}{192 \pi^3} \quad (6)$$

where  $\tau_\mu$  is the muon lifetime. The energy dependent factor in front of cosine in equation (4) is called the *decay asymmetry*. It is given by:

$$a(\epsilon) = \frac{2\epsilon - 1}{3 - 2\epsilon}, \quad (7)$$

and will be the more different from zero the higher the positron emission energy.

The energy spectrum of the positrons as well as the asymmetry factor dependence on emission energy, are both shown in figure 2. One notes that the asymmetry factor can be either positive or negative, even though its mean value is positive:

$$\bar{a} = \int_0^1 n(\epsilon) a(\epsilon) d\epsilon / \int_0^1 n(\epsilon) d\epsilon = 1/3. \quad (8)$$

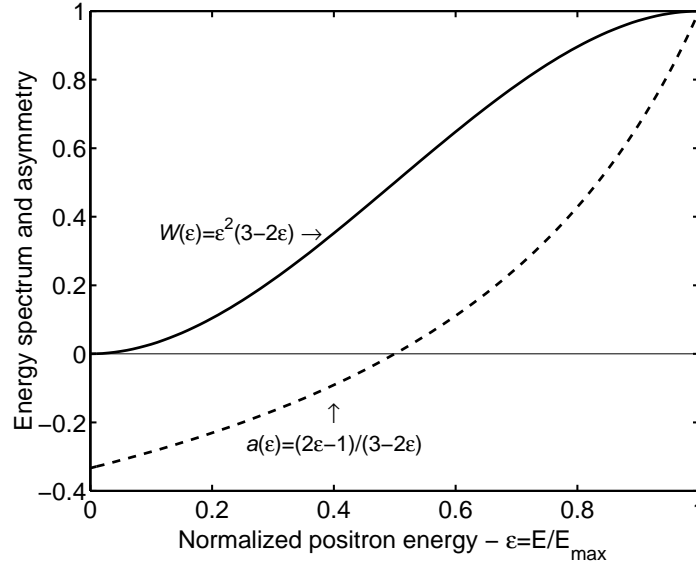


**Figure 2:** Energy spectrum of positrons generated during muon decay  $W=W(\epsilon)$  and the dependence of their asymmetry factor  $a=a(\epsilon)$  on emission energy.

In practice, the exact value  $\bar{a} = 1/3$  is rarely obtained, typical experimental values lying in the range 0.2–0.3 [19]. The most important reasons for this include: the stopping of low energy positrons before they reach the scintillators, the finite acceptance angle of the detectors and, in presence of high magnetic fields, the deviations in positron trajectory.

Figure 3 shows the *angular distribution* of decay positrons, where one can notice that the anisotropy of emission varies as the positron energy changes. Thus, the maximum value of anisotropy ( $a = 1$ ) is reached for the most energetic positrons ( $E = E_{\max}$ ), the minimum one ( $a = -1/3$ ) for the lowest energy positrons, whereas those having intermediate energies ( $\epsilon_m = 1/2$ ) will be emitted isotropically ( $a = 0$ ) (see also figure 2).

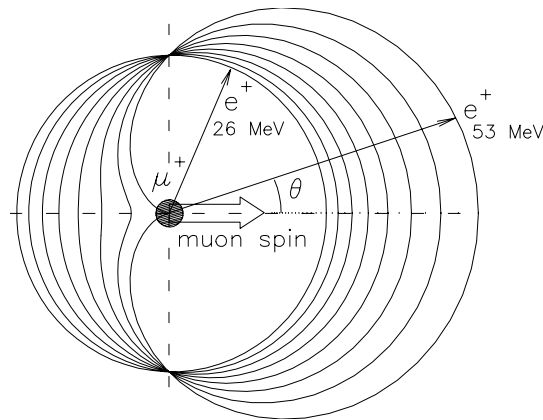
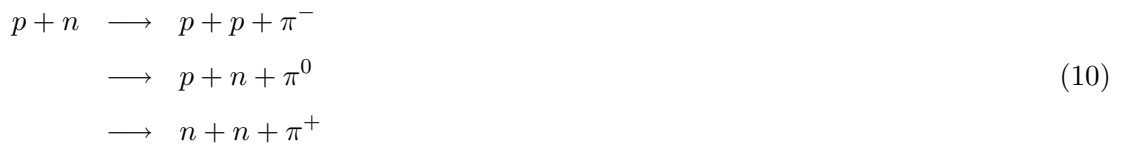
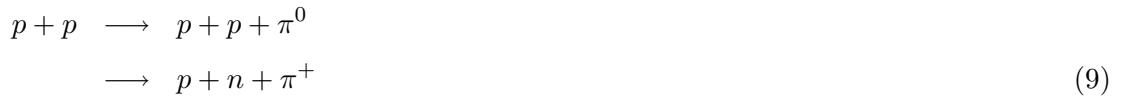


**Figure 3:** Angular distribution of positrons from the  $\mu^+$  decay. In particular, for positrons of maximum energy  $\epsilon = \epsilon_{\max}$  the asymmetry factor is maximum too, whereas for those having  $\epsilon = \bar{\epsilon}$  it is zero (isotropic emission).

### 2.3 Production of spin polarised muon beams

Muons are easily found in nature since they are a dominant constituent of the cosmic rays arriving at sea-level [17, 2] (in fact the first muons were discovered just in cosmic rays<sup>3</sup>). However, due to their very high energies, totally random arrival times and, most importantly, to the absence of any polarisation, they are practically useless for laboratory purposes.

As mentioned at the beginning of section 2.2, a necessary condition for performing experiments with muons is the availability of spin polarised muon beams. In this case all the muons implanted into a sample will have the same initial spin direction and it would be possible to follow the time evolution of the ensemble. Thus, intense beams of muons are artificially prepared at a number of locations in the world. All of these facilities rely upon the muon production [41, 39] through pion decay<sup>4</sup>, which implies that proton accelerators of sufficiently high energy for pion production are required. Pions are obtained through high energy nucleon–nucleon collisions during which they can escape the nuclear potential. Practically, one directs a high energy proton beam to a target characterised by a low atomic  $Z$  number (usually beryllium or pyrolytic carbon are used because they ensure low multiple scattering of the proton beam), where the following reactions take place:



It is not difficult to estimate the threshold energy for single pion production, which follows from the condition that the available centre-of-mass energy should equal the pion’s rest mass. From detailed calculations (see appendix A) it turns out to be  $\sim 180$  MeV. However, to obtain higher production rates it is useful to have protons of  $\geq 500$  MeV due to the increased cross section at these energies. The 800 MeV ISIS proton beam not only optimises single pion production but allows also for double pion production, their energy threshold being  $\sim 600$  MeV.

---

<sup>3</sup>The abundant muon presence in the cosmic rays is a well-known consequence of time-dilation effects in special relativity [123, 7] and of the fact that they do not undergo the nuclear interactions of the protons, neither do they suffer the conspicuous ionisation energy losses of the electrons. With a flux of  $\sim 10^{-2} \text{ cm}^{-2} \text{ s}^{-1} \text{ sr}^{-1}$  and a mean energy of 2 GeV, muons make up for more than half of the charged particles present in cosmic rays which reach the earth surface.

<sup>4</sup>There are other types of decay as e.g.  $K^+ \longrightarrow \mu^+ + \nu_\mu$ , which also yield positive muons  $\mu^+$ , but with too a high energy to be of any use in condensed matter studies.

After a mean lifetime of 26.03 ns the pions will decay by a purely leptonic process into muons and muon neutrinos according to the well known scheme:



This process is illustrated in figure 4.

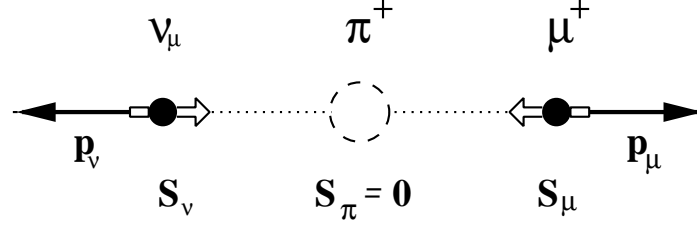


**Figure 4:** Muon production through pion decay. The decay of pion is shown in its own rest frame. From the conservation laws both the linear and angular momenta (spins) of  $\mu^+$  and  $\nu_\mu$  should be collinear and opposite.

In the pion's rest frame, where  $\mathbf{p}_\pi = 0$ , the linear momenta of neutrino and muon must be antiparallel since this is a two body decay (see figure 4). This implies that the muon momentum and energy should have a *fixed* value. Simple calculation reported in appendix A give  $p_\mu = 29.78 \text{ MeV}/c$  and  $E_\mu = 4.12 \text{ MeV}$ .

Moreover, since also the spin of  $\pi$  is zero, the  $\mu^+$  and  $\nu_\mu$  angular momenta should be equal but opposite in direction. This, together with the fact that neutrinos have a fixed helicity ( $\mathcal{H} = -1$  due to non conservation of parity), implies that muons are generated with their spin antiparallel to their momentum. Therefore, if muons having a certain momentum direction were collected into a beam, this would be both 100% spin polarised and also monochromatic.

It is interesting to note here that pions decay into muons, even though the phase-space factor is more favourable to a decay into electrons. This can be traced back to the existence of a fixed helicity for neutrinos, which implies that the other lepton too will have the same helicity. Since the probability of this process goes as  $\sim (1 - v/c)$ , the much heavier muons will be largely favoured.

The muons produced from pion decay can be divided into three main categories:

**Subsurface muons:** Some of the generated pions will stop into the muon production target before reaching its surface. Muons originating from such decays are called subsurface muons. Their momentum is lower than  $29.8 \text{ MeV}/c$  due to the preliminary degrading by the passage through the target. The rate  $N_\mu$  of these muons at the end of the channel follows from the range-momentum relationship  $R \simeq a \cdot p^{-3.5}$  [112]. It depends strongly on muon momentum according to [151, 6]:

$$N(p_\mu) = N_s \cdot \left( \frac{p_\mu}{29.8} \right)^{3.5} \cdot \exp \left( - \frac{m_\mu l}{p_\mu \tau_\mu} \right) \quad (12)$$

where  $N_s$  is the number of muons at the target surface,  $p_\mu$  the muon momentum expressed in MeV/c,  $\tau_\mu$  the muon life time,  $m_\mu$  the muon mass and  $l$  the length of the beam line. An important consequence of this dependence is a strong decrease in muon beam intensity if the magnetic transport system were tuned to lower momenta. Consequently, an intense highly polarised muon beam of low energy cannot be efficiently produced in such a way.

**Surface muons:** Are called the muons originating from pions which stop and decay at the surface of the production target. Essentially they behave as the subsurface muons and formula (12) still holds. They too have the advantage of being monoenergetic and present also a 100% polarisation. Furthermore, for (sub)surface muons a small beam spot size is achievable, provided that the proton beam focus at the production target is small. Sometimes they are called Arizona muons since they were observed for the first time at LBL, Berkeley from scientists of the University of Arizona [112].

**Decay muons:** Are called the muons originating from pions decaying in flight just outside the target. Since in this case the pions are moving during their decay, these muons display a continuous energy distribution and much higher momenta (typically  $\sim 100$  MeV/c) [125]. The pions are introduced into a section consisting of a long superconducting solenoid providing a high magnetic field ( $\sim 5$  T), such that at the end of it almost all of them have decayed. The exit of the solenoid acts as a diffuse source of muons. The subsequent muon extraction system collects and transports the muons to the sample. Due to the finite acceptance of the transport system the polarisation of such a decay muon beam reaches  $60 \div 80\%$ .

Decay muons provide the only way to produce negative muons. Indeed, if they were produced like surface muons they would be immediately captured and bound to the atomic nuclei of the production target.

## 2.4 Basics of Muon Spin Rotation

The characteristics of muon production and decay are crucial to the  $\mu$ SR technique. Indeed the success of  $\mu$ SR, as clearly pointed out in [32], relies heavily on two circumstances:

- The *intrinsic spin polarisation* of the muons during their production from pions, and
- The *anisotropy* of the positron emission in the subsequent muon decay.

Both of them are expressions of the violation of parity conservation in processes where particles subject to the weak interaction are involved.

But there is also another important factor which makes  $\mu$ SR possible. It is the fact that the intrinsic initial polarisation can be substantially preserved throughout the transport of the muons and, more importantly, also during implantation and thermalisation into the sample.

The various processes by which muons lose their initial energy and thermalise in a medium are fast, having a typical duration of  $10^{-12} \div 10^{-10}$  s [21] and, moreover, they are predominantly electrostatic in nature. Indeed, the muon depolarisation  $\Delta P$  in the scattering process with electrons and nuclei can be caused only by spin-dependent forces and its value is estimated to be [47]:

$$\Delta P \propto \beta^2 \frac{m_e}{m_\mu} \sin^2 \frac{\alpha}{2}, \quad (13)$$

where  $\beta = v/c$  and  $\alpha$  is the scattering angle. Since the factor  $\beta^2(m_e/m_\mu)$  is quite small for muons, the loss of the original polarisation will be irrelevant.

The subsequent evolution of the muon polarisation within the sample may then be monitored, because the muon indicates its spin direction at the moment of the decay by emitting a positron preferentially in this direction (see fig. 5). The various experimental techniques with muons can be divided into three main groups by following a simple criterion: one considers the angle between the initial muon spin polarisation  $\mathbf{P}_0$  and the direction of the externally applied magnetic field  $\mathbf{B}_{\text{ext}}$ . When these two vectors are perpendicular the experiment is said to be performed in a *transverse field* (TF) geometry, in case they are parallel one speaks about *longitudinal field* (LF) geometry and, finally, if there is no externally applied field one speaks about *zero field* (ZF) measurements (the last geometry may be considered a particular case of the LF) (for more details refer to [22]).

Most of the measurements presented in this work were performed in the TF geometry. However, in chapter 7 we will deal with a much more complex case where two fields were applied simultaneously: a longitudinal field of fixed value and a time varying transverse one.

In the most general case, whenever the implanted muons sense a magnetic field  $\mathbf{B}$  (to which both external and internal fields contribute), the muon magnetic moment will begin to precess about it at the Larmor frequency, determined by the muon gyromagnetic ratio (see figure 5.b):

$$\omega_\mu = \gamma_\mu \cdot B, \quad \text{where} \quad \frac{\gamma_\mu}{2\pi} = 13.553 \text{ kHz/G}. \quad (14)$$

Together with the magnetic moment of the muon also its positron emission pattern will precess, as shown in figure 5.c. If one puts a simple scintillation detector anywhere near the sample and measures the positron count rate as a function of time following the implantation, one will find:

$$N(t) = N_0 \exp(-t/\tau_\mu) [1 + AG_x(t) \cos(\omega_\mu t + \phi)] + N_B, \quad (15)$$

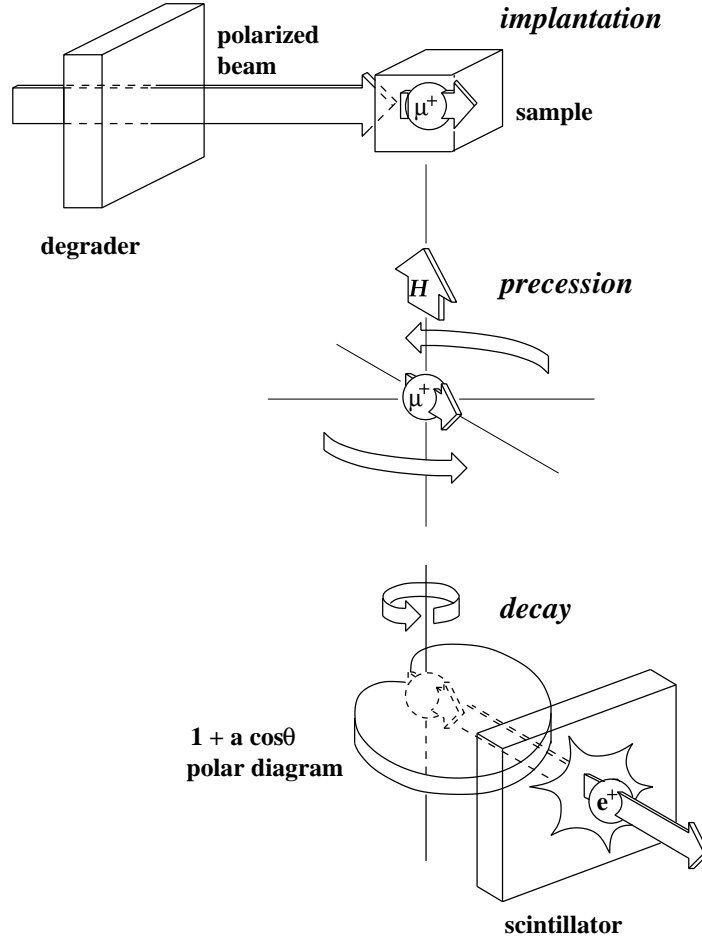


**Figure 5:** Schematic illustration of a  $\mu$ SR experiment. It can be divided into the implantation of muons into the sample (top), their precession in the presence of a magnetic field  $H$  (the sum of local and externally applied fields) (middle) and the detection of the decay positrons, highly correlated with the muon spin direction (bottom) (from [32]).

where  $N(t)$  and  $N_0$  represent the number of decay positrons detected at the times  $t$  and  $t_0 = 0$  respectively,  $\tau_\mu$  and  $\omega_\mu$  are the muon mean lifetime and angular frequency of precession,  $A$  is the asymmetry,  $N_B$  are counts due to the background positrons (not correlated and therefore constant) and  $G_x(t)$  is a relaxation function. To better illustrate the behaviour of the count rate described by equation (15) a typical spectrum is shown in figure 6. A closer look at the histogram represented in the figure reveals three main characteristic features:

1. The overall exponential decrease in the positron count rate due to the finite lifetime of muons ( $\tau_\mu \simeq 2.2 \mu\text{s}$ ). This is observable in every kind of experiments with muons be it *TF*, *LF* or *ZF*.
2. The oscillation of the signal due to the periodical sweep of the *anisotropically* emitted positrons over the positron detector ( $[1 + a(\epsilon) \cos \theta]$ , where  $\theta = \omega_\mu t + \phi$  in equation (15)).

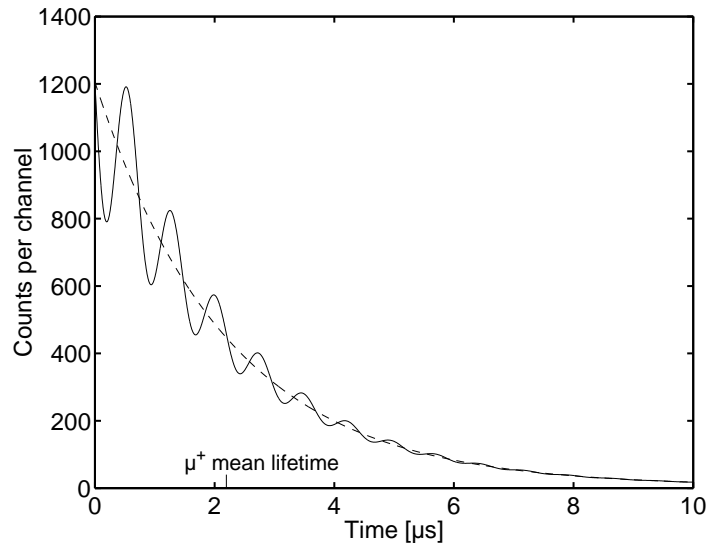


**Figure 6:** Time spectrum of a TF- $\mu$ SR experiment. The exponential decay reflects the finite lifetime of the muon, whereas the oscillatory behaviour is related to the muon spin precession in the magnetic field ( $B=100$  G).

This oscillation reflects the muon angular frequency  $\omega_\mu = \gamma_\mu B_\mu$ , where  $B_\mu$  is the magnetic field sensed by the muons at the site where they stop.

3. The possible background  $N_B$  caused by various sources like: cosmic ray muons, positrons from the muon beam, etc. Today in all the muon facilities worldwide, both pulsed or continuous ones, the background can be kept at almost negligible levels.

To extract some information, more interesting than the obvious precession frequency, it is useful to consider the signal *asymmetry*. For a couple of opposite detectors  $i, j$  placed in the precession plane and having identical detection efficiencies, it is given by:

$$A_{ij} = \frac{N_i(t) - N_j(t)}{N_i(t) + N_j(t)} \quad (16)$$

$$= AG_x(t) \cos(\omega_\mu t + \phi) \quad (17)$$

As defined, the asymmetry will be devoid of the exponential component, the only “memory” of it remaining in the statistical error bars, which will increase at long times. The dimensionless maximum asymmetry  $A$  is determined both by the geometry of the detectors and by their sensitivity to the emitted positrons (see figure 2). The smaller the acceptance angle of the detector and the higher its detection threshold the higher will be the asymmetry.

If the muons stop in equivalent sites within the lattice where the magnetic fields are identical, they will precess in phase and the magnitude of the initial polarisation will be preserved during rotation. However, most of the time the fields at different sites will be different and, as a consequence, there will be a gradual loss of polarisation due to dephasing. The relaxation function  $G_x(t)$ , which describes this progressive depolarisation will reflect the

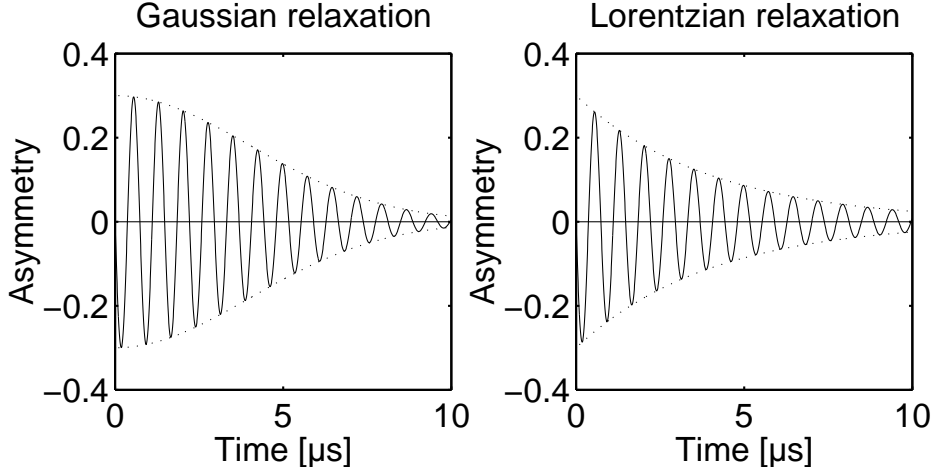


**Figure 7:** Asymmetry spectra obtained from the data of figure 6 after having subtracted the background and discarded the exponential dependence. Both the Gaussian and the Lorentzian envelopes have a decay parameter  $\sigma = \lambda = 0.25 \mu\text{s}^{-1}$ , the applied magnetic field is  $B=100 \text{ G}$ .

autocorrelation function for the precessing muons and hence is of paramount importance in most  $\mu\text{SR}$  experiments. It is similar to the well known Free Induction Decay (FID) signal in NMR (see section 2.5) and can be experimentally extracted from equation (17).

Generally, the shape of the relaxation function can be quite complex, depending on the exact origin of the depolarisation. However, in case of a TF measurement, there exist two simple functions which account for a large number of experimentally observed cases [27]. Thus, for a continuous and isotropic distribution of *static* magnetic fields the relaxation is characterised by a Gaussian shape given by  $G_x(t) = \exp(-\frac{1}{2}\sigma^2 t^2)$ . On the other hand, for local fields rapidly *fluctuating* in time, the relaxation will follow a Lorentzian curve  $G_x(t) = \exp(-\lambda t)$ . Both of them are depicted in figure 7 where typical values for the relaxation constants are assumed.

It is interesting to note that the relaxation function is very sensitive to dynamical effects as e.g. thermally activated muon diffusion, where one observes a change of the shape toward a slow exponential decay referred to as “motional narrowing” (similar to the analogous NMR phenomenon). Moreover, chemical reactions of the muons with the stopping medium and spin exchange interactions will be also detectable by a careful analysis of the relaxation function.

Depending on its chemical environment, the muon can thermalise and pick up an electron to form a neutral atomic state called muonium ( $\text{Mu} \equiv \mu^+ e^-$ ). This hydrogen-like atom has very different properties with respect to the “bare” muon  $\mu^+$ , because in the muonium atom the electron and muon spins are coupled through a hyperfine interaction. Since the latter has quite a high value, the muonium precession frequency is rather high. Indeed, there is a

factor of approximately 103 between the two gyromagnetic ratios [32, 153]:

$$\frac{\gamma_{\text{Mu}}}{2\pi} \simeq 103 \cdot \frac{\gamma_{\mu}}{2\pi} = 1.394 \text{ MHz/G} \quad (18)$$

Muonium formation is observed in a great variety of substances: gaseous, liquid and solid, but it is by no means formed in every material. Paradoxically, in metals the muon is found as  $\mu^+$  even though the number of electrons with which it can potentially form Mu is quite large. It is just this high concentration of conduction electrons to shield very effectively the muon electrostatic potential, thus preventing the formation of bound states [76]. In insulators, on the other hand, the electrons needed to form muonium are captured from those in the ionisation wake created by muons during their thermalisation.

The hyperfine interaction between the 1/2 spins of the muon and electron in a muonium atom leads to two energy levels, a lower singlet state  $^{\text{S}}\text{Mu}$  ( $S = 0$ ) and a higher triplet state  $^{\text{T}}\text{Mu}$  ( $S = 1$ ). The application of an external magnetic field will remove the triplet degeneration giving rise to three separate levels, typical of a Breit–Rabi diagram (see also figure 33.b). Since the electrons of a stopping medium usually are not polarised, the muonium is formed with equal probability in states with spin parallel or antiparallel to the muon spin, of which only the first represent eigenstates of the hyperfine interaction. The others display very fast (4463 MHz for Mu in vacuum) hyperfine oscillations between the  $|\uparrow\downarrow\rangle$  and  $|\downarrow\uparrow\rangle$  states (where  $\uparrow$  and  $\downarrow$  refer to the electron and muon spins respectively), so that half of the muon polarisation appears lost in most experiments. Finally, because the hyperfine interaction is finite, the muonium triplet transition  $\omega_{\text{Mu}}$  will split into two frequencies  $\omega_{12}$  and  $\omega_{23}$  for fields  $B \gtrsim 20 \text{ G}$ .

To take into account the behaviour of muons in different local environments (including also muonium formation), the evolution of spin polarisation can be described by an extended version of equation (15):

$$N(t) = N_0 \exp(-t/\tau_{\mu}) [1 + \sum_i A_i G_{xi}(t) \cos(\omega_i t + \phi_i)] + N_B, \quad (19)$$

where the meaning of the various symbols is the same as before.

In closing this paragraph we mention briefly the two other techniques, namely the Muon Spin Relaxation and Muon Spin Resonance.

Muon Spin Relaxation is performed either as a *LF* or as a *ZF* technique. In this case, the detection is made by using just a forward and a backward detector. The muon spin evolution is determined by the presence of internal magnetic fields with nonvanishing components perpendicular to the initial polarisation. In the particular case of *static* fields, randomly distributed according to a Gaussian curve of width  $\Delta/\gamma_{\mu}$ , one obtains a relaxation function known as the Kubo–Toyabe curve:

$$G_z(t) = \frac{1}{3} + \frac{2}{3} (1 - \Delta^2 t^2) \exp(-\Delta^2 t^2/2), \quad (20)$$

valid for a  $ZF$  experiment. The further application of a longitudinal field basically affects the asymptotic tail by raising its original  $1/3$  value toward 1. There exists a large variety of relaxation functions arising both from the possibility of dynamic fields or from different static field distributions. Nevertheless, in all cases the obtainable information is entirely contained in the dependence of the relaxation function  $G_z(t)$  on magnetic field and temperature.

In Muon Spin Resonance muons are implanted in the presence of a longitudinal magnetic field and a transverse RF field of appropriate frequency is used to induce transitions between the Zeeman levels. This technique allows to investigate the full range of final state spectroscopy, like chemical reactions and diffusion processes inside the sample. At lower fields the study of paramagnetic species such as muonated radicals is possible. When operated at pulsed muon sources, besides a substantial decrease in the RF power (due to the low duty cycle of the beam), also an extension of the frequency bandwidth of the facility is possible (for more details refer to e.g. [31]).

## 2.5 $\mu$ SR vs. NMR

To better evidence the particularities of the  $\mu$ SR technique, a comparison with other experimental methods is quite useful [36, 66, 153, 67]. Of these, nuclear magnetic resonance (NMR) is the one that bears the major resemblance with  $\mu$ SR. Since the basic principles of the NMR technique are covered in a series of excellent textbooks [1, 139], here we just state the main idea behind it.

In a sample, the interaction of the nuclear magnetic moments  $\boldsymbol{\mu}_n = \gamma_n \hbar \mathbf{I}$ , with a polarising magnetic field  $\mathbf{B}$ , described by the Hamiltonian:

$$\mathcal{H} = \gamma_n \hbar \mathbf{I} \cdot \mathbf{B}, \quad (21)$$

will give rise to  $2I+1$  Zeeman energy levels (here  $\mathbf{I}$  is the nuclear spin and  $\gamma_n$  its gyromagnetic ratio). If next, an RF field  $\mathbf{B}_1$  is applied, whose frequency  $\nu_1$  is such that the energy  $h\nu_1$  equals the separation  $\Delta E$  between the quantum states of (21), a resonant energy absorption will occur.

Let us now proceed to the comparison between NMR and  $\mu$ SR:

- First of all, the two techniques employ quite different probes: NMR uses the nuclei of the sample, a natural probe, whereas  $\mu$ SR the muons, an implanted particle. Due to the almost universal muon implantability it is possible to study samples whose nuclei do not exhibit a magnetic moment.
- When both techniques are possible, there is complementarity with NMR concerning the explored sites: muons usually will stop in the interstitial sites, whereas nuclei reside always in the crystalline lattice nodes.

- The muon precession in a typical muon spin rotation experiment is quite the same as the free induction decay (FID) signal in NMR, the main difference consisting in the detection method employed: in NMR one has a *macroscopic* detection, whereas in  $\mu$ SR what is recorded are *single events*. Since these are nothing but highly energetic positrons, which readily penetrate cryostat walls, shieldings, etc., complicate sample environments are possible in  $\mu$ SR.
- The magnetic field also plays quite a different role in the two techniques: in NMR its value should be high due to its spin-polarising function, whereas in  $\mu$ SR it is not strictly necessary (as e.g. in ZF- $\mu$ SR). Since the muon's initial polarisation is independent of the state of its environment, it is rather easy to study metallic or superconducting samples, in which performing NMR is more problematic, mainly because of an only partial penetration of RF or magnetic fields.
- Since in a common NMR experiment the nuclear susceptibility is of the order of  $\sim 10^{-6}$ , the detection of the nuclear magnetisation through the FID signal requires the presence of something like  $\sim 10^{15}$  nuclear spins. On the other hand, muons are available in almost 100% spin polarised beams and a typical asymmetry parameter is around  $\sim 20\%$ . Hence, it will suffice to collect as few as  $10^5$  muon decay events to have a comparable detection of the spin precession in  $\mu$ SR.
- The noise too has a different origin in the two cases: in NMR it is present usually in the form of thermal and electronic noise ( $\propto f^{-1}$ ); in  $\mu$ SR instead, the noise is mainly of statistical nature (and hence  $\propto \sqrt{N}$ ).
- Since in a sample muons are present only as a very dilute probe, with practically no interactions among them, the theoretical interpretation of most  $\mu$ SR experiments is straightforward. This simplicity is further enhanced by the absence of a muon quadrupolar moment. In NMR, the ordinary presence of strong nuclear couplings and of quadrupolar momenta, quite often requires the use of complex pulse sequences to extract the relevant information.
- Although true muon spin resonance experiments are possible, a common  $\mu$ SR experiment does not represent a genuine resonant process. This is in contrast to the NMR, which is a direct and an intrinsically resonant phenomenon.
- A drawback of muons as compared with nuclei is given by their finite mean lifetime ( $\tau_\mu \simeq 2.2 \mu\text{s}$ ), which restricts the possibility of studying the spin precession at long times (in practice one is restricted to 5–8 muon lifetimes ( $\sim 15 \mu\text{s}$ ), which will limit somehow the frequency resolution).

- Further interesting analogies exist also between magnetic relaxation parameters as measured with these two techniques and their link with the space and time fluctuation of the local magnetic fields. Any dephasing in a typical muon spin *rotation* experiment is evidence for either an inhomogeneous internal field distribution or spin-spin relaxation, analogous to the one given by the  $T_2$  parameter in NMR. The longitudinal field  $\mu$ SR leads to spin *relaxation* whose parameter depends on the internal field distribution or on spin-lattice relaxation processes, described by  $T_1$  in NMR.

## Chapter 3

# Low energy muons: Production, transport and detection

IN this chapter, after a short overview of the various techniques available for epithermal muon beam production, we will concentrate on the use of the moderator technique. Its implementation at the ISIS pulsed muon facility is described in detail including the production, transport and detection of epithermal muons. These topics are preliminary to the characterisation of the most relevant properties of the slow muon source, to which the next chapter is devoted.

### 3.1 Techniques to generate low energetic muons

The generation of low energy (LE) muons is a rather challenging task because of the severe limitations inherent in the physics of muon beam generation. Due to the limited lifetime of the muon and to the spatially extended muon source, one rarely can get beams with a divergence less than 100 mrad and a spot size less than a fraction of  $\text{cm}^2$ . This, associated to the relatively low (typically in the range  $10^5$ – $10^8 \mu^+/\text{s}$ ) intensity of surface muon beams, implies that even at state-of-the-art facilities the LE muon beam intensity does not exceed some hundreds of particles per second.

Nonetheless, the potentialities opened by the use of LE muon beams have boosted in recent years the efforts of various research groups worldwide, which have devised a host of different techniques for producing slow muons. The ideal beam should be characterised by good phase space properties, particularly by low energy spread, low divergence and also by a high degree of polarisation. The most promising technique up to the present day seems to be the so-called moderator technique which makes use of muon moderation in thin films of solid rare gases. However, for completeness we briefly review the salient points of the other techniques also (see [95] for more details).

## Beam line tuning

The simplest and most straightforward way to generate a low energy muon beam is to tune a surface muon beam to lower momenta by changing the magnetic field of the transport system. In this case the drop in intensity follows a power law, i.e.  $N(p) \propto p^{3.5}$  (cfr. equation (12)). The method has been tested down to 3 MeV/c (equivalent to  $E_\mu \simeq 40$  keV) at LAMPF [6] during experiments for the observation of the Lamb shift in muonium atoms.

Even though the measured rates were in good agreement with the prediction of formula (12) in a broad momenta range between 5 MeV/c and 28 MeV/c, the method should be discarded due to the very low efficiency in slow muon production. Indeed, if one assumes a typical surface muon intensity of  $10^6 \mu^+/\text{s}$ , the formula (12) yields less than one muon per second at an energy of  $\sim 100$  keV.

But still worse, at lower energies a significant deviation from the  $p^{3.5}$  law sets in, mainly due to multiple scattering and energy straggling into the degrader. Moreover, there is an additional intensity drop related to the decrease in efficiency of the transport and focusing elements at low momenta and also to the increased relative weight of positron contamination.

Finally, the lower the energy the higher the probability of electron capture and muonium formation, which below  $E_\mu \lesssim 1$  keV definitely rules out the possibility of using this method to generate LE muon beams.

## Phase space compression (PSC)

Following methods of electronic and stochastic cooling [98], which have been successfully applied to beam quality improvement of proton, antiproton and heavy ion beams [92], phase space compression has been tested also for slow muon production [146].

Beam cooling is a technique whereby the physical size and the energy spread of a particle beam is reduced without any accompanying beam intensity loss. During the process the phase space density, which can be used as a figure of merit for the beam, will increase considerably. There is an apparent violation of Liouville's theorem regarding the conservation of phase space volume, but the point is that this theorem only applies to "conservative" systems and cooling, by definition, is not a conservative process.

The cooling electronics acts on the beam through a feedback loop to alter the beam's momentum or transverse oscillations according to the cycle:

- An electrode pick-up recognises the position of the particle.
- The error signal is amplified through an amplifier.
- The signal is then applied to a kicker electrode, which deflects the particle by an angle proportional to the deviation error.

In case of muons, the phase space compression (PSC) is performed by trapping the particles into a solenoid with a magnetic field of  $\sim 5$  T and, through the detection of the individual positions and velocities, one can bring them to the centre of the axis of solenoid. The successive PSC stages comprise a transverse electric field that rotates in phase with the muons at their cyclotron frequency and will result in the required deceleration. Since the corrections are applied to individual particles, the rate of incoming muons is restricted to  $\lesssim 10^4 \mu^+/\text{s}$ .

The main drawback of this, otherwise extremely effective method, consists in its relative slowness, which implies significant modifications in case of application to beams of short lived particles like muons. The need for rapid action within a particle's lifetime span requires the use of formidable electronics and represents a true technological challenge. Nonetheless, the method could be used in future as an improvement stage of a pre-cooled beam.

### Cyclotron trap

The operation of the cyclotron trap [35,34] relies upon the action exerted by a weak focusing cyclotron field produced by superconducting ring coils, which winds up the range path of the stopping particles inside a moderator.

Guided by the field, the particles stop in the central region of the device where are successively extracted with an axial electric field into a magnetic transport channel, which eventually transports them to the target region.

Since the long deceleration path remains concentrated within a relatively small volume, low density targets (typically 1 mbar  $\text{H}_2$ ) can be used. The moderation can be also carried out by employing suitably arranged thin foils ( $10\text{--}200 \mu\text{g}/\text{cm}^2$ ) [138].

This deceleration method has been successfully used in the past at PSI<sup>1</sup> and LEAR<sup>2</sup> for experiments with muonic, pionic and antiprotonic atoms [5,137,4,126,59].

Its main drawback when applied to positively charged particles is represented by the high cross section for electron capture in the keV energy range [63,51] and also by the more general problem of the presence of fringe magnetic fields.

### Beam foil degradation

The deceleration of muons in matter can be achieved by the use of thin metallic foils [3], in a way similar to that occurring in the production target during beam line tuning.

At LAMPF, a subsurface muon beam of 10 MeV/c with a momentum spread of  $\Delta p/p = 10\%$  incident on gold or beryllium foils, was shown to give muons with energies in the range 0–20 keV at a rate of  $\sim 10^{-5}$  per incoming muon [72].

---

<sup>1</sup>Paul Scherrer Institut, Villigen, Switzerland

<sup>2</sup>Low Energy Antiproton Ring, CERN, Geneva, Switzerland

The drawback of the technique, apart from the modest efficiency, is given by the very broad spectrum of the generated slow muons. The formation of muonium and  $\text{Mu}^- (\equiv \mu^+ e^- e^-)$  through processes of electron capture in the last layers of the target foil, will result in an increased background rate. Both these factors degrade the beam quality making it unsuitable for thin films studies.

### Frictional cooling

The method of beam foil degradation can be improved by a simultaneous use of an accelerating electrostatic potential along the trajectory of the particle, which goes under the name of frictional cooling [100]. The method relies upon the fact that at very low energies (below 10 keV in case of muons) the stopping power of matter becomes larger the higher the particle energy. Once one sets a given electrostatic field, all the lower-energy muons will be accelerated since they gain more energy from the electrostatic field than they lose during the interaction with the moderator, whereas the muons with higher energy will be decelerated since the opposite is true for them. The advantage with respect to the previous method consist in the considerably reduced spread in energy and momentum.

Frictional cooling has been tested in the case of negative muons  $\mu^-$  of 10 MeV/c, where a stack of thin graphite foils of  $\sim 5 \mu\text{g}/\text{cm}^2$  each was used as a moderator in presence of a strong longitudinal magnetic guiding field [100]. As theoretically predicted, a significant increase in spectral density around some keV and a decrease in the angular spread was observed.

There are also some more elaborate variants of frictional cooling. One is the so-called *frictional accumulation* [147] which is expected to convert an intermediate-energy negative muon beam into a low-energy one.

The other one is the *ionisation cooling*, which is foreseen to be used in the future muon colliders [29, 109]. Here the beam loses both transverse and longitudinal momentum as it passes through a material medium, but whereas the longitudinal momentum is restored by a coherent re-acceleration, the transverse one is constantly reduced to a negligible value through the different moderation stages.

To achieve a substantial cooling something like 20 stages are needed, each of which consisting of two components. The first component performs a cooling in transverse phase space by reducing the particle energy in a degrader (typically liquid hydrogen) in a strong focusing environment alternated with linac accelerators to restore the longitudinal component. The second component instead consist of a dissipative lattice, with absorbing material wedges introduced to interchange longitudinal and transverse emittance.

The normalised transverse emittance is reduced by almost three orders of magnitude whereas the longitudinal emittance by a factor of 10. The final acceleration is estimated to be ap-

proximately 6 GeV and the fraction of muons remaining at the end of the cooling system is expected to be about 60%.

### **Ionisation of thermal muonium**

Different studies [88, 89, 8] have revealed that in selected materials, such as hot noble metals (Pt, Ir, Re or W) or low density silica powders ( $\text{SiO}_2$ ), 5–10% of the implanted surface muons is re-emitted as thermal muonium. The technique of ionisation of thermal muonium consists in the use of lasers to induce multiple photon excitation so as to produce ultra slow muons which are subsequently collected and transported to the sample station. The ionisation is obtained by exciting the  $1s$  electron state into a  $2p$  state and from here to continuum [101] with the laser pulse synchronised with the muon bunch arriving from the accelerator. This method of generation of ultra slow positive muons is carried out at UT-MSL/KEK<sup>3</sup> [101].

In practice a 2 mm thick boron nitride/tungsten (BN/W) target is inserted in the pulsed 500 MeV primary proton beam. The first BN layer of the target is used for pion production and decay, whereas muon diffusion and thermalisation together with the successive muonium formation and release do take place at the second hot (2300 K) tungsten layer<sup>4</sup>. The produced ultra slow muon beam is characterised by a residual energy of 0.2 eV, with a sharply pulsed time structure of 49 ns FWHM and a rate of  $\sim 0.2 \mu^+/\text{s}$ .

The advantage of this method consists in the very low energy of the produced muons and in its high degree of monochromaticity. However, there are also significant drawbacks. Due to muonium formation, the polarisation of the ultra slow muon beam is limited to 50%. Furthermore, the application of the method is restricted only to pulsed muon facilities where the laser synchronisation is possible. Finally, the high required costs, technical efforts and maintenance, especially because of the presence of the laser system, make this approach not very appealing for use in long term experiments or in future pulsed slow muon facilities.

### **Moderation by films of rare gas solids**

The moderation of particles in a material medium, although similar to the deceleration which occurs in common degraders, has some very remarkable features which makes it the preferred technique for slow muon production.

When using degraders to slow down particles the effect is a mere reduction of their energy through random collisions and ionisation processes, which results in broadly distributed energy spectra and very low production efficiencies.

---

<sup>3</sup>University of Tokyo, Meson Science Laboratory for High Energy Physics, KEK, Tsukuba, Japan.

<sup>4</sup>The use of tungsten is preferred to more efficient muon to muonium converters like silica powders because of its higher endurance in the harsh environment of the primary proton beam.

The specific properties of the moderators, on the other hand, come into play during the interaction and the transport of thermal or epithermal particles, leading to a highly efficient energy conversion process and to an unusually large emission probability characterised by narrow, low energy spectra. Up to the present date the moderation in frozen noble gas layers represents the most promising method for generation of slow muons.

The use of moderators is long known as an efficient method to produce low energy positrons [55, 88]. This has permitted the development of positron beams, once adequate positron moderators in the range of eV energies has been discovered. Typical production efficiencies, defined as  $\epsilon = N_{\text{eV}}^{\text{out}}/N_{\text{MeV}}^{\text{in}}$ , are of the order of  $10^{-4}$  in case of  $e^+$  [129].

The experience gained over the years with positrons represented a precious guidance also in the work with muons. However, some fundamental differences between  $\mu^+$  and  $e^+$ , in particular with regard to their masses, lead to rather diverse physical and dynamical behaviour and, as a consequence, to significantly different interaction with the moderator material.

In 1987 a collaboration at TRIUMF [57, 56], showed that very slow muons in the eV energy range are directly emitted from appropriate moderator materials, namely solid rare gases, with an efficiency up to  $10^{-5}$ .

There seems to be a direct correlation between the energy gap of the insulating rare gas solid and its moderation efficiency. Indeed, the highest efficiency has been found for solid Ar films (see figure 8) deposited over a thickness optimised cold ( $T \sim 15$  K) Al foil, whereas the other noble gas solids, having lower energy gaps, give lower efficiencies. Surprisingly, common positron moderators like single-crystal LiF, quartz and polycrystalline copper, gave significantly worse performance.

The discovery of suitable muon moderators together with the demonstration of the full conservation of spin polarisation (up to  $87 \pm 3\%$ ) during the moderation process [96], made the successive development of low energy muon beams possible, first at the continuous muon source at PSI [97] and then at the pulsed muon facility at ISIS [149]. The latter, being among the subjects of the present thesis, will be described in much more detail in the following chapters.

What makes the moderation technique appealing for use in dedicated low energy muon beams is given by its relatively simple technical requirements and by its long-term stability (cfr. chapter 4). Moreover, the present slow muon production efficiencies are the highest among all the previously described methods.

To better understand the experimental technique and the principles of the muon moderation, we give a very brief theoretical overview, addressing the interested reader in section 4.6.2, where a more extended discussion will be given.

The models which try to explain the mechanisms of slow muon generation and the ob-

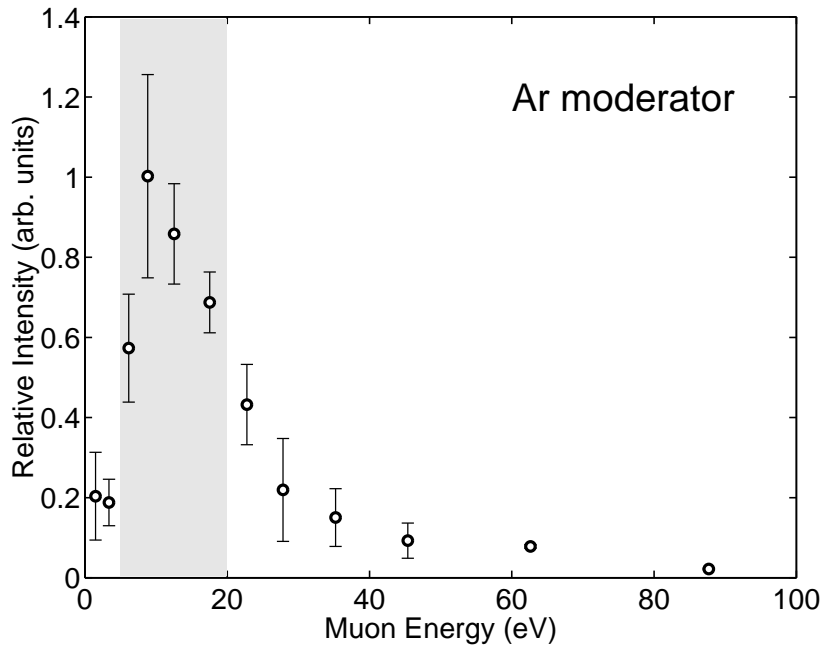


**Figure 8:** Energy distribution of epithermal muons emitted from a solid Ar moderator (from [99]). Note the peak of emission in the highlighted area corresponding to  $\sim 10$  eV (comparable with the energy gap of argon  $E_{\text{gap}}(\text{Ar}) \simeq 14.16$  eV) and the tail extending at higher energies.

served energy spectra are essentially two: the *spur model* and the *hot muon model*. There is however, an ever increasing evidence that only the hot muon model describes the experimental results in a satisfactory way, even though not in their entire completeness.

**The spur model** [90, 111, 91] assumes that towards the end of the muon path inside the material a charge recombination takes place. The products in the muon ionisation trail (free electrons, ions and radicals) are then bound to the already low energy muon to give muonium. The muonium atom successively diffuses to the surface where, due to recombination with a hole, it breaks and releases a free, low-energy  $\mu^+$ .

**The hot muon model** [56], as its name suggests, assumes that muons will leave the material while they are still “hot”, i.e. not yet thermalised. This is mainly ascribed to the absence of energy losses during the transport of muons whose energy is sufficiently low.

After the initial ionisation regime, fast charge exchange processes take place when the energy drops below  $\sim 10$  keV. These become the most important dissipative mechanisms [130, 131] in the lower energy range. The charge exchange is not anymore effective as an energy loss channel once the muon’s kinetic energy falls below a threshold level of some tens of eV. The only dissipative process remains the excitation of phonon spectra, which is highly ineffective too due to the very small phonon energies (5–10 meV in case of van der Waals solids [69]). Since in wide band gap insulators, such as rare gas solids, the energy threshold is higher than in most other materials, this model explains fairly well the correlation between the muon moderation efficiency and the size of the band gap of the moderator.

## 3.2 Generation of LE muons at ISIS

### 3.2.1 The DevA beam area

As pointed out in section 2.3 in all the muon facilities worldwide, the muon beams are generated through pion decay. Therefore, we begin with a quick overview of the high energy proton production at RAL<sup>5</sup>.

#### The synchrotron and the extracted proton beam

The principal component of the ISIS facility at RAL consists of a rapid cycling proton synchrotron which is used in conjunction with a heavy stopping target to create intense beams of pulsed neutrons by the spallation process, as well as for feeding the ISIS pulsed muon facility (see figure 9). From a preliminary injector, negatively charged hydrogen ions enter a linear

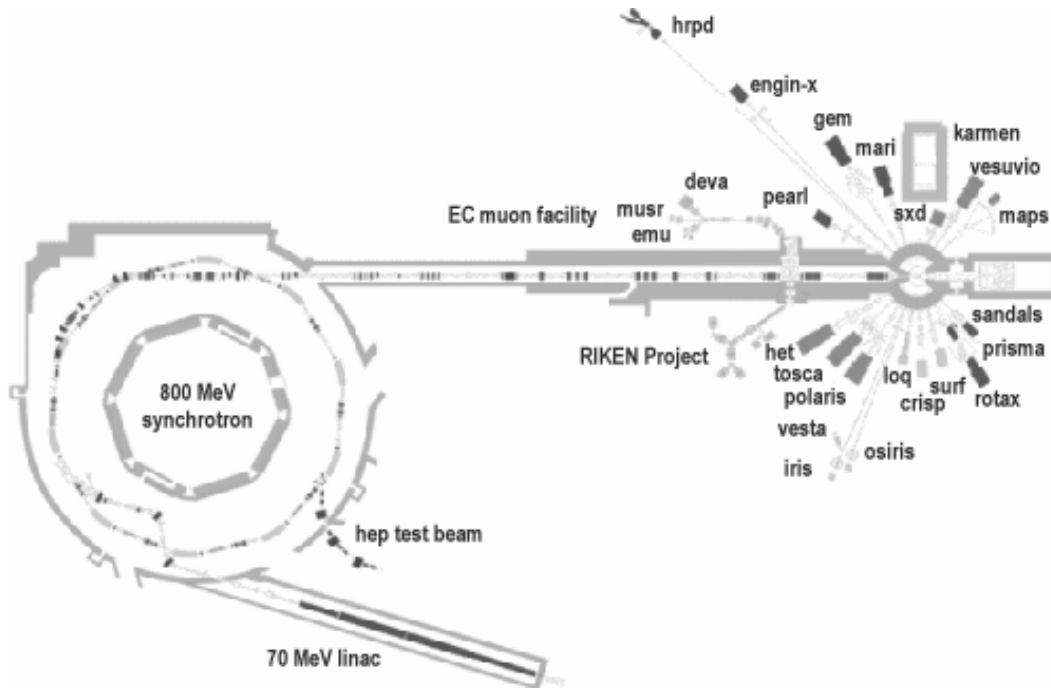


**Figure 9:** Layout of the ISIS experimental hall at RAL, showing the linac injector, synchrotron, extracted proton beam and spallation neutron target. Muons are produced in the thin graphite target 20 m upstream of the neutron target and feed the EC and RIKEN muon facilities. The slow muon experiment is carried out in the DevA area.

accelerator where they reach an energy up to 70 MeV. This serves as an injector for the synchrotron where, after being stripped from the electrons, the protons are accelerated by RF cavity sections until they reach almost 800 MeV. A fast pulse from a deflecting magnet

<sup>5</sup>Most of the material of this section is taken from several sources [41, 39, 43, 40], where a detailed account on the operation of the ISIS pulsed facility is given.

There is also a vast amount of literature regarding particle beam production, acceleration, focalisation and transport. For a more general survey the reader is addressed to e.g. [155, 154].

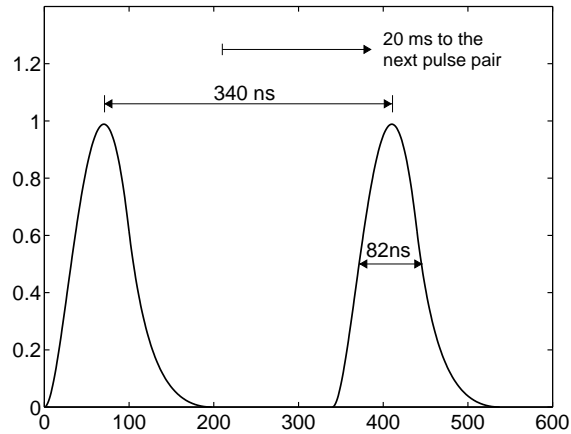


**Figure 10:** Time-structure of the double muon pulse at RAL (two pulses 82 ns FWHM, 340 ns apart). It closely reflects the structure of the 50 Hz pulsed proton beam. Note the asymmetric distortion in the shape of each pulse due to the convolution with the pion lifetime (26 ns).

extracts the protons in the beam channel. The proton beam thus generated has an intensity of 180 A (equivalent to  $1.2 \cdot 10^{15}$  protons per second). The synchrotron produces pulses at 50 Hz, but since the machine operates at twice the circulation frequency of the protons, it generates a double pulsed proton beam.

### The muon target station and surface muon beam lines

At approximately 20 m upstream the spallation source, a muon production target is inserted into the beam, consisting of a thin slab of pyrolytic graphite, which optimises both for high pion production rates and simultaneously induces low multiple scattering of the proton beam.

Since the muons are born from the decay of pions generated in nucleon-nucleon reactions, the muon pulses will reproduce the time-structure of the proton beam, although broadened by the pion decays occurring in the muon production target. Thus, the muon pulse width is 82 ns FWHM with a peak-to-peak separation of 340 ns, as shown in figure 10.

The surface muons emitted within an angle of 0.13sr are collected by two quadrupole magnets close to the production target and then transported toward the experimental areas. However, they are first momentum analysed by two magnets which also bend the beam direction by  $90^\circ$ . In between the two magnets a quadrupolar triplet creates a dispersed focus which allows the selection of the *momentum spread* by means of a horizontal collimator.

To reduce the positron contamination a cross field separator is used. It acts as *velocity selector* which can discriminate muons ( $\beta_{\mu^+} = 0.24$ ) from positrons ( $\beta_{e^+} \simeq 1$ ).

The double-pulse structure of the muon beam is highly undesirable in many experiments, so a fast electrostatic kicker [15, 42] is used to deliver a single muon pulse on each station (K in figure 11). For a proper operation of the kicker the synchronism with the pulse arrival and the fast response of the electric field are of primary importance.

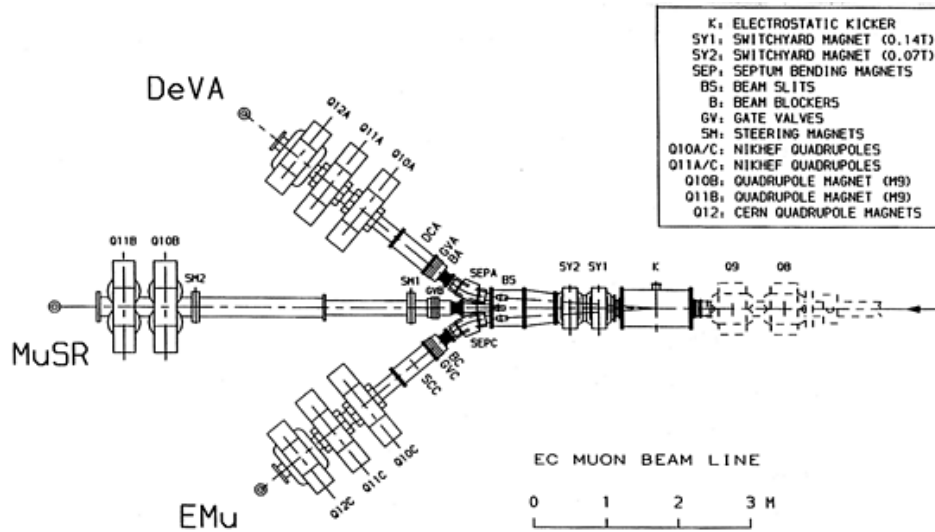


**Figure 11:** Layout of the three EC muon beam lines DevA, MuSR and EMU, showing the electrostatic kicker, denoted by K, and the two septum magnets SEPA and SEPC. The first muon pulse is divided in two by the kicker and sent to DevA and EMU stations, whereas the second pulse is transmitted undeflected to MuSR. The incoming muons are depicted by the small arrow at the right.

### The DevA beam area

We close this section by giving the main characteristics of the muon beam available at DevA (*Development Area*) station, which was employed for the experiments regarding the slow muon production.

- The vacuum system of the muon beam line and that of the extracted proton beam are separated by a  $100\ \mu\text{m}$  aluminium window 15 cm from the production target. As a result of energy degradation occurring in this window the muon momentum for all the three beam lines is reduced at  $26.5\ \text{MeV}/c$  [41, 39], slightly less than the nominal surface muon momentum of  $28\ \text{MeV}/c$ .
- The beam is 100% spin polarised with the muon spin antiparallel to the propagation direction, except for a very slight upward rotation of approximately  $6^\circ$ , induced by the electrostatic kicker.
- The muon spot size of the DevA beam line is  $27 \times 10\ \text{mm}^2$  FWHM in case of fully opened momentum slits, resulting in a momentum bite of  $\Delta p/p = 10\%$  [42].
- The number of muons per pulse in the DevA area when using the 7 mm thick production target<sup>6</sup> is approximately  $3000 \pm 300$  which, taking into account the 50 Hz synchrotron frequency gives  $1.5 \cdot 10^5\ \mu^+/\text{s}$ , roughly one fourth of the total muon production rate [39].

<sup>6</sup>During some of the measurements of thin film samples a 10 mm target was inserted into the proton beam increasing the muon rate by  $\sim 32\%$ .

### 3.2.2 The pulsed epithermal muon beam line

As previously mentioned, the epithermal muon beam at ISIS is based on the principle of muon moderation in condensed van der Waals gases, which is schematically illustrated in figure 12. The surface muon beam strikes the metallic predegrader, where muons lose most of their energy. The moderation to some tens of eV occurs in the thin layer of frozen rare gas deposited on the cold substrate.

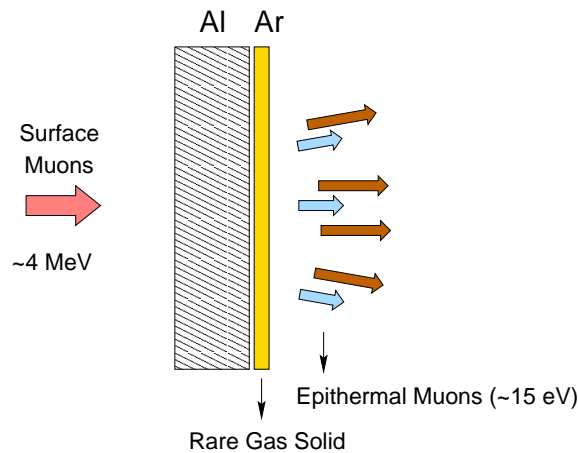


**Figure 12:** Principle of slow muon generation using the moderation technique. The metallic predegrader serves as a cold substrate where the gas layer is deposited. At the downstream side there is a flux of slow muons which are successively collected and transported (not shown) to the experimental area (adapted from [95]).

The apparatus for the generation of the tertiary slow muon beam, similar to the analogous one at PSI [96], is shown in figure 13. It is composed by three main sections: the slow muon generation area, the transport and focusing, and the experimental station. First we give a short overall description of the apparatus and next we focus on the most important aspects of its operation like: the ultra high vacuum (UHV), the temperature requirements, the high voltage focusing and transport, the electronics and data acquisition, etc. (for a considerably more detailed account the reader is referred to e.g. [148, 86, 18], from which most of the technical specifications of the epithermal muon apparatus are taken).

The muons coming from the DevA area with a momentum of  $26.5 \text{ MeV}/c$  hit first a rotatable degrader. It is a Kapton<sup>®</sup> foil disk having a diameter of 120 mm and  $30 \mu\text{m}$  thick, which can rotate freely around a horizontal axis. Its purpose is to slow down the incoming muons in such a way that the peak of the muon stopping profile can be adjusted on the moderator target. A  $60^\circ$  angle relative to the beam direction provides the maximum stopping distribution at the downstream side of the substrate.

The following  $50 \mu\text{m}$  thick scintillation beam counter provides the timing signal of the incoming muon pulse, to be successively used in all the time-of-flight measurements (see also figure 22).

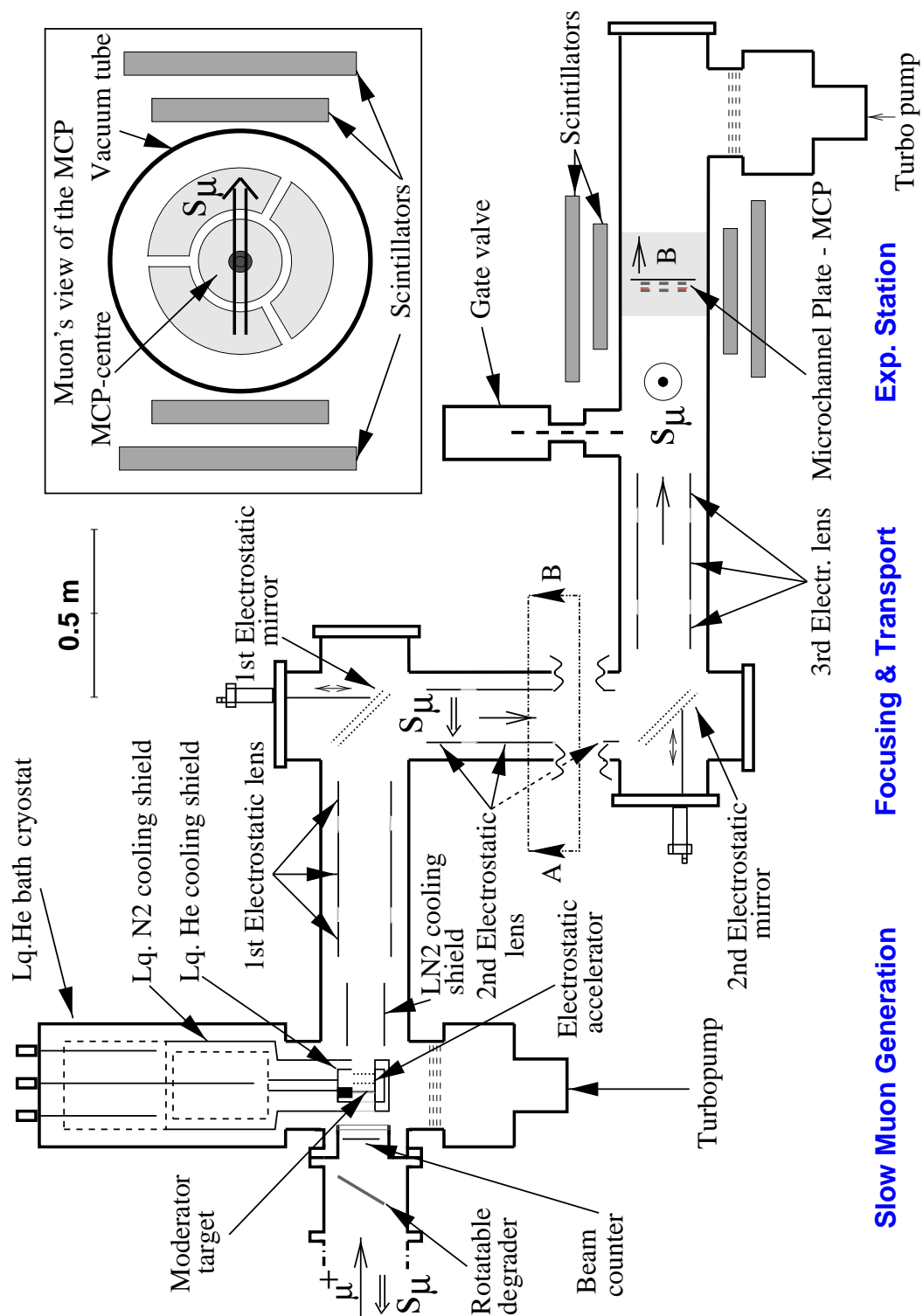


**Figure 13:** Layout of the slow muon apparatus at RAL consisting of three parts: slow muon generation, focusing and transport, and experimental station. Once generated in a frozen rare gas layer (Ar), the slow muons are accelerated up to several keV and transported through an electrostatic system which does not affect their spin direction. The detection is made with a microchannel plate detector (MCP) and a decay positron telescope at the sample station. The two bends are used to reduce to a minimum the background of fast muons and decay positrons.

To separate the  $10^{-6}$  mbar beam line vacuum from the  $10^{-10}$  mbar UHV region of the apparatus a  $50\ \mu\text{m}$  thick, 50 mm in diameter stainless steel window is used [148]. The choice of the window thickness represents a compromise between two opposite requirements: that of being mechanically resistant to the maximum differential pressure of 1 atm and the necessity of having a beam divergence as low as possible. The window position, very close to the moderator, ensures a low particle loss due to multiple scattering angular spread.

The rotatable degrader, the beam counter and the separation window, are all mounted on a short piece of tube which serves as a buffer between the DevA beam line and the apparatus itself. The latter is essentially a long vacuum tube, containing two bends and operating under UHV conditions. As we shall see later, the ultra high vacuum is of primary importance for an efficient slow muon emission, since the moderation properties of the frozen rare gas films are dramatically affected by the contamination degree of their surface.

To achieve a good overall vacuum two turbo molecular pumps, positioned respectively below the moderator target and close to the experimental station, are used. Their pumping power is further enhanced by the liquid helium bath cryostat and also by the liquid helium and liquid nitrogen shieldings, all of which act as cryogenic pumps. The need for low temperatures is dictated by the thermodynamic equilibrium curves in the  $pT$  plane (also called sublimation pressure curves) of the solid rare gases [69]. Thus, to produce a stable film at  $10^{-10}$  mbar, substrate temperatures of the order of 10 K are required.

After passing through the aluminium windows of the two cooling shieldings, the surface muons will stop in the liquid helium cooled aluminium moderator target. Here they lose part of their energy, whereas the moderation itself takes place in the solid rare gas layer in the downstream side of the target. From it the muons are re-emitted as “slow” particles with energies in the range of some tens of eV (see figure 12).

To allow the slow muons to pass unhindered towards the transport section, both cooling shieldings are provided in their downstream side with circular openings of 50 mm in diameter [148]. These openings will expose the moderator target to thermal radiation and, therefore, will limit the lowest reachable temperature to approximately 7 K. This undesirable effect can be somehow reduced by the insertion between the cryostat and the first electrostatic lens of a ring-shaped shield cooled to liquid nitrogen temperature.

To electrostatically accelerate the low energy muons before they enter the transport section, the aluminium target is set to a high positive voltage of  $\sim 10$  kV. Once accelerated the muons are alternately focused by a system of three electrostatic lenses (Einzel lenses).

Since roughly only one out of ten thousand is an epithermal muon, there exists a considerable “natural” background consisting of fast muons and their respective decay positrons which should be suppressed. This is achieved by the use of a two-bend geometry where each bend has at its flexure point a 90 degree deflecting electrostatic mirror, at the same potential

as the aluminium target.

A precise tuning of the voltages in the transport system is achieved by performing an intermediate check of the slow muon beam spot size, thanks to a microchannel plate detector (MCP) placed behind the second mirror (turned off during tuning procedure).

At the end of the beam line the slow muons are finally focused to a sample or an MCP. The magnetic field needed for the  $\mu$ SR measurements is created by a solenoid, wound around the vacuum tube in a symmetric position with respect to the sample. To detect the decay positrons four couples of scintillation counter telescopes are used. These are heavily shielded with lead bricks, to avoid the considerable positron background due to the neighboring experimental areas and to the positrons arising from the decay of fast muons inside the apparatus.

When performing depth slicing experiments, the tuning of the slow muon beam at the required energy is achieved by an additional electrostatic decelerator mounted just in front of the sample. To avoid frequent bake-ups of the apparatus, we make use of a gate valve which separates the sample station from the upstream part, and thus allows to change the sample without appreciable deterioration of the vacuum of the whole vessel.

### 3.2.2.1 General UHV and temperature requirements

As mentioned at the beginning of the previous section, both temperature and vacuum conditions are essential for a reliable operation of the slow muon beam line.

Simple calculations [37] are useful for an estimate of the time needed for the residual pressure gas to be deposited as an impurity monolayer on the cryogenic moderator surface. Assuming a unitary sticking probability and a residual gas pressure of  $p_{\text{vac}}$ , they give  $t_{\text{monol.}} \simeq 10^{-6}/p_{\text{vac}}$ , where the time is expressed in seconds and the pressure in mbar. For a reliable long-term operation a pressure of at least 4 orders of magnitude lower is required, which implies that pressures in the range  $10^{-10}$ – $10^{-11}$  mbar should be achieved.

The materials used to build up the apparatus are restricted to those compatible both with UHV requirements and those of heat endurance. The latter follows from the need to perform bake-ups in case of exposition to atmospheric pressure which, in order to limit the evacuation time at a reasonable value ( $\sim 48$  hours), implies reaching temperatures as high as  $180^\circ\text{C}$ , limited only by the most delicate components such as the temperature sensing diodes.

The vacuum level is controlled with a cold cathode ionisation gauge and, for more accurate analysis especially during cryogenic target preparation, a mass spectrometer residual gas analyser is used.

The liquid helium bath cryostat, consisting of two equal capacity (12l) tanks for liquid helium (LHe) and liquid nitrogen ( $\text{LN}_2$ ), allows to routinely reach a base temperature of  $\sim 8\text{K}$ <sup>7</sup>. It ends with a circular cold finger of 80mm diameter, where a silicon diode for

---

<sup>7</sup>Although sufficient for the deposition of most of the noble and other examined gases, the substrate

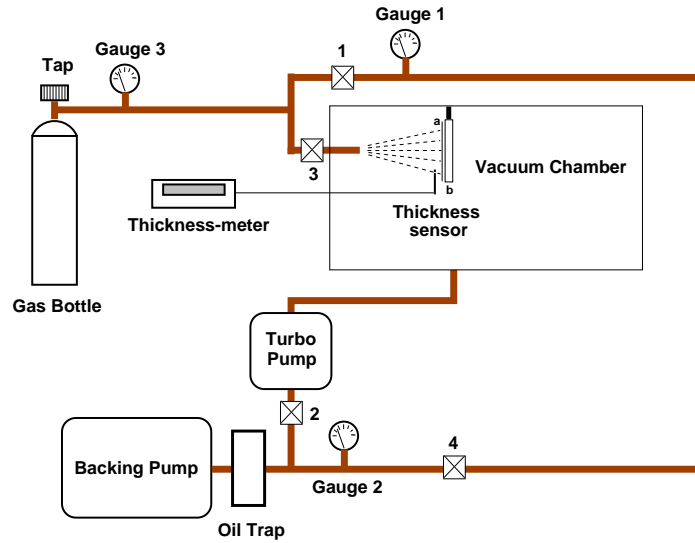


**Figure 14:** Schematic drawing of the noble gas film preparation procedure. Once the system has been evacuated, the leak valve (3) is opened to allow in the high purity gas which condenses onto the cold substrate (b). The pressure and film thickness are monitored respectively with the gauge (2) and the quartz micro-balance.

temperature measurement and an electric heater, used for the evaporation of the frozen gas layer, are mounted. To satisfy the requirements of low outgassing rates in the target region and optimal heat conduction, the substrate holder is built of massive oxygen free copper (OFC). A 3 mm thick sapphire plate placed between the cold finger and the substrate holder permits good thermal contact at low temperatures, while ensuring excellent electrical insulation.

Once the base pressure ( $\sim 5 \cdot 10^{-11}$  mbar) and temperature ( $\sim 8$  K) are stable, it is possible to grow noble gas films. The standard procedure for film growth consists in allowing inside the vacuum chamber the particular gas to be deposited which, once in contact with the cold substrate, will form the solid layer.

In practice, to regulate the partial pressure to approximately  $10^{-5}$  mbar, a high precision leak valve, connected to a high purity gas bottle (e.g. Ar better than 99.999% vol.), was employed. The gas is admitted into the vacuum chamber through a small copper orifice for about 5 minutes, while a quartz micro-balance, fixed close to the target, is used to measure the thickness of the frozen rare gas layer during the growth procedure (see figure 14). Within a few minutes after the film deposition, the residual gas pressure returns to the usual operative range of  $10^{-10}$  mbar.

Films grown at the lowest achievable temperature did not however display the best muon moderation efficiency, therefore a systematic study of slow muon yield as a function of depo-

---

temperature of  $\sim 8$  K did not allow the growth of a stable film of frozen neon, which is supposed to be probably a better muon moderator than argon.

sition temperature was carried out (see section 4.2.1).

Since the film thickness gauge measures only relative variations of the oscillation frequency, an initial absolute calibration was needed. It was performed by laser interferometry where the light intensity reflected by the two opposite faces of the growing film was recorded. It displays the usual Airy interference pattern which once fitted gives the coefficient of absolute calibration [148].

### 3.2.2.2 Slow muon generation target

To optimise the slow muon production rate one must enhance the fraction of muons stopped in the interface between the cold aluminium substrate and the frozen rare gas film. However, it is not easy to obtain both a high moderation efficiency and a high absolute number of slow muons, and a compromise has to be made. Indeed, the narrower the momentum distribution, the higher the slow muon yield, since one can virtually stop the beam profile in the exact interface by using additional degraders. On the other hand, a narrow momentum distribution is obtained only at the expense of a reduction of the overall beam intensity, which will therefore give a lower number of epithermal muons. The best solution was to keep the momentum slits of the DevA surface muon channel fully opened, which results in a momentum spread of  $\Delta p/p = 10\%$ .

Another major concern in the preliminary design was the preservation of the original beam quality, by keeping its spatial and momentum spread to a minimum. This puts restrictions on the sort of materials used as degraders and in their positioning with respect to the target. Low  $Z$  materials, placed as near as possible to the target will help reduce range straggling and beam spot enlarging due to multiple scattering (see also section 4.6.1).

Monte Carlo simulations by means of programs such as e.g. SRIM [158], are helpful for an evaluation of the beam characteristics before it reaches the frozen rare gas layer. The insertion of the various beam line components, including: the rotatable degrader, the beam counter, the beam window, the two cold shields and finally the metallic substrate, together with their respective materials and thicknesses yields a total stopping power of  $141(5) \text{ mg/cm}^2$ . That this represents quite an accurate value, is clearly demonstrated in figure 15, where the slow muon yield<sup>8</sup> is given as a function of the stopping power (or rotation angle) of the initial variable degrader. Even though its thickness was kept to a minimum, the presence of the peak in the muon yield, shows that indeed when changing the degrader angle the stopping profile of the beam crosses the aluminium/argon interface.

Other simulations, to estimate the effect of multiple scattering in the beam spot size, use as initial condition the nominal cross section of the DevA beam before it enters the slow muon apparatus ( $27 \times 10 \text{ mm}^2$  FWHM). They yield a scattering enlarged size of  $32(3) \times 22(2) \text{ mm}^2$

---

<sup>8</sup>In this and in the following graphics the slow muon yield is intended normalised to its maximum value.

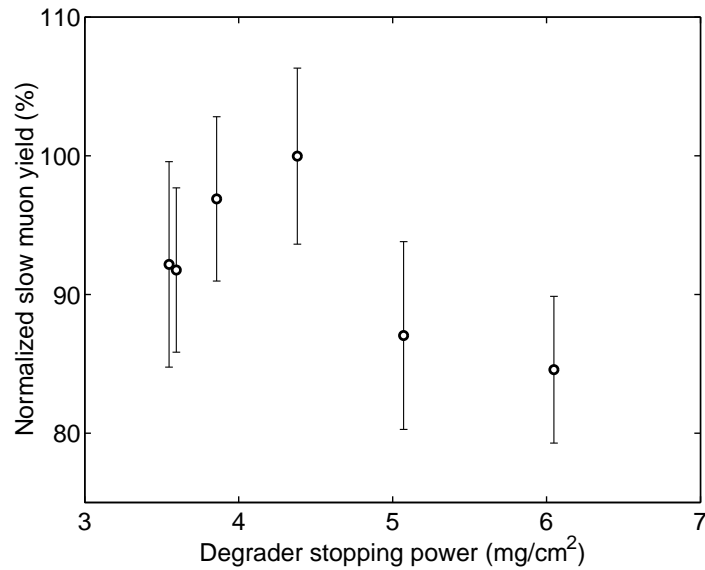


**Figure 15:** Normalised slow muon yield as a function of the rotatable degrader stopping power. As the angle increases the beam stopping profile shifts towards the aluminium/argon interface giving a maximum yield for  $\sim 4.4$  mg/cm<sup>2</sup>.

FWHM at the moderator target position, still considerably smaller than the moderator diameter of 48 mm, which implies only negligible losses of particles.

With a proper setting of the rotatable degrader about 50% of the muons will stop in the high purity (99.999%), 320  $\mu$ m thick Al substrate and only a small fraction of them will be re-emitted as epithermal particles.

A simple calculation shows that these muons, whose typical kinetic energy is of the order of  $E \simeq 10$  eV, have quite a short decay length  $l_d$ . It is given by the (non-relativistic) formula  $l_d = \sqrt{2E/m_\mu} \cdot \tau_\mu$  which, once substituted the numerical values, yields  $l_d = 9.1\sqrt{E}$ , where  $E$  is expressed in eV and  $l_d$  in cm. This example clearly points out the necessity for muon acceleration and transport up to the experimental station, otherwise the losses due to particles decaying before they reach the sample will be quite relevant. Taking into account the beamline length of 3.23 m, a rough estimate indicates that acceleration voltages of the order of some kV are needed.

To this purpose at the downstream side of the Al substrate a two-stage electrostatic accelerator was mounted<sup>9</sup> (see figure 16).

The equipotential surfaces of the accelerator are defined by electro-formed copper meshes with 95% transmission each. The latter are clamped between pairs of thin circular copper

<sup>9</sup>In fact there were two slightly different accelerator assemblies that were used: a two-stage one, commonly employed for most of the experiments, and a more complex three-stage assembly, specifically designed for energy distribution measurements. Here we concentrate only on the simpler two-stage accelerator, leaving the discussion of the other one for section 4.3, where the energy spectrum of slow muons will be discussed.

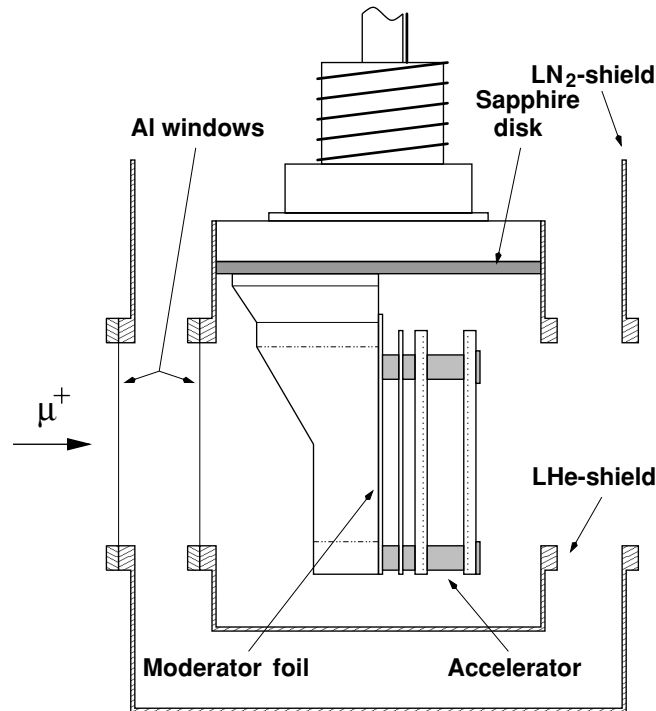


**Figure 16:** Layout of the target region showing the substrate, the accelerator, the cold finger and the cryogenic shields. All the accelerator components, separated by Macor<sup>®</sup> spacers, are mounted on a massive oxygen-free copper substrate holder. The Al substrate is brought up to +8 kV, whereas the guard ring placed very close to it reduces the effect of stray fields from the nearby shield and improves the electrostatic field homogeneity. The second grid is put at a ground potential (from [86]).

frames, which are separated by electrically insulating Macor<sup>®</sup> spacers. Since the typical distance between frames is of the order of some mm, small compared to their 48 mm diameter, very careful mounting is required to avoid electric field distortions. The same is true for the choice of the materials, where those having equal thermal expansion coefficients were preferred.

The substrate holder, set to a high positive voltage  $U_{\text{acc}}$  of typically +8 kV, will accelerate the slow muons arising from the noble gas film toward the transport channel. The presence of two frames, of which the last is electrically grounded, splits the particle acceleration into two steps. To further improve field homogeneity and reduce the influence of electrical fields from the grounded surroundings a guard ring was mounted in the accelerator, halfway between the substrate and the first frame.

The construction of the electrostatic accelerator was considerably aided by the use of the RELAX3D program package developed at TRIUMF [70], which can numerically calculate the distribution of the electrostatic potentials once the boundary conditions are specified (all the details about these calculation can be found in [18]).

### 3.2.2.3 High voltage focusing and transport

The focusing and transport of slow muons to the experimental station is carried out with the aid of electrostatic lenses and mirrors. Since these are purely electrostatic devices, the muon spin will be unaffected by them which, because of the two-bend geometry of the apparatus, implies a final muon spin direction perpendicular to its momentum (see figure 13).

The lenses are of the so-called Einzel type, consisting of a series of three stainless steel cylinders with their axis coincident with the beam axis, of which the outer are set at a ground potential, whereas the middle one is brought to a high positive voltage. Their operation principle is based on the different impulses a charged particle receives by the electric field in the gaps between cylinders, whose overall result is a net focusing action without changes in particle's energy [45].

To limit their intrinsically large spherical aberrations, and thus work in the best possible paraxial approximation, the largest diameter cylinders, compatible with the dimensions of the vacuum chamber, were chosen. Typical operation voltages were of the order of 75% of the acceleration voltage  $U_{\text{acc}}$ .

The electrostatic mirrors are even simpler devices which can roughly be compared to some sort of “transparent” plane capacitors. Indeed, they consist of two parallel elliptical frames where grids of equally spaced (1 mm), thin tungsten wires ( $30\ \mu\text{m}$ ) are mounted. A high electric potential applied to one of the frames, with the other put at ground, creates a uniform electric field which will deflect the charged particles. Depending on its orientation and applied voltage the mirror can select particles according to their energy. In our case an orientation angle of  $45^\circ$  and an applied voltage equal to that used in the acceleration stage  $U_{\text{acc}}$ , will deviate the epithermal muons by  $90^\circ$ . More importantly, the mirror can eliminate most of the background consisting of fast, non moderated muons which, due to their much higher kinetic energy, will be transmitted through it. There is however a small fraction of muons with energies in the range  $U_{\text{acc}} < E_k \leq 2U_{\text{acc}}$  which cannot go past the mirror and will be transported or decay inside the vacuum chamber. Their positrons will appear as background noise in the time-of-flight (TOF) spectra *before* the slow muon peak which has  $E_k \simeq U_{\text{acc}}$  (see also figure 24 and section 4.1). To reduce this noise the initial single-bend vacuum tube geometry, was extended to include an additional lens and mirror, therefore resulting in the actual two-bend configuration, characterised by a higher rejection rate, even though at the cost of a somewhat diminished transport efficiency due to a 31% increase in tube length.

Monte-Carlo simulations were useful to check and optimise the parameters of the transport system prior to its construction (the thesis [86] contains an extended account of these calculations). They foresee a transport efficiency of 78(2)% in the case of a two-bend geometry with an 8 kV initial accelerating voltage.

A careful beam line tuning is essential to a good performance of the apparatus. In the actual geometric configuration the tuning procedure involved two distinct steps. With reference to figure 13, the voltages of lenses 1 and 2 together with the orientation of the first mirror were initially adjusted. In this case the second mirror is turned off and the best setting corresponds to a minimum beam spot size on the MCP behind the second mirror. Next, the second mirror is turned on and its orientation together with the voltage of lens 3 are changed until one gets the maximum positron count rate at the sample position. The second step is rather delicate, so the tuning procedure was performed by a simultaneous check of two different signals. One comes from muons stopped in a 40 mm diameter quartz disk, placed in the centre of the vacuum tube at the sample position, whereas the other originates from muons detected at an MCP located 32 cm downstream the sample. This arrangement gives the possibility to follow the shortening of the focal length of the lens as the applied voltage is gradually increased. As expected, for lower voltages the muons pass almost undisturbed and hit the MCP, whose maximum signal is observed first. High enough voltages ( $V_{L3} = 6.0$  kV) will eventually make the focus coincide with the sample position and hence give a peak in the counting rate of the detector telescopes surrounding the sample. The tuning curves obtained for the three lenses are shown in figure 17.

Since the electrostatic mirrors operate at a fixed voltage ( $U_m = U_{acc}$ ), only the orientation has to be adjusted for them. Nevertheless, we checked the reflectivity of one of the mirrors as a function of the applied voltage, and report the measurement results in figure 18. As expected, the lowest energy muons, characterised by  $E_k \simeq U_{acc}$ , have the smallest transport threshold and therefore are the first to appear when the mirror voltage roughly equates half the value of the accelerating voltage. As the mirror is set to higher voltages, ever more energetic muons are transported towards the detector and consequently the curve displays a monotonically increasing behaviour. At last, when the mirror and the initial accelerating voltages coincide ( $U_m = U_{acc} = 8$  kV), particles with an energy up to twice  $eU_{acc}$  are transported, whereas the slow muon path inside the mirror electrodes is completely symmetric, thus ensuring their maximum transport efficiency.

The mirror orientation can be easily changed since each mirror plane is defined by three points of which one is fixed and the other two can be moved via two linear motion feedthroughs. Vertical and horizontal steering are achieved respectively by moving the linear drives in the same direction or opposite to each other. The change in muon count rate, as the mirror deflection angle is varied, can be monitored with the same MCP detectors used for lens tuning. However, to take full advantage of the position sensitive feature, all the signals coming from the four MCP sectors (centre, left, right and bottom) are employed in this case (see figure 20.b).

Typical tuning curves for the first mirror are shown in figure 19. Horizontal steering

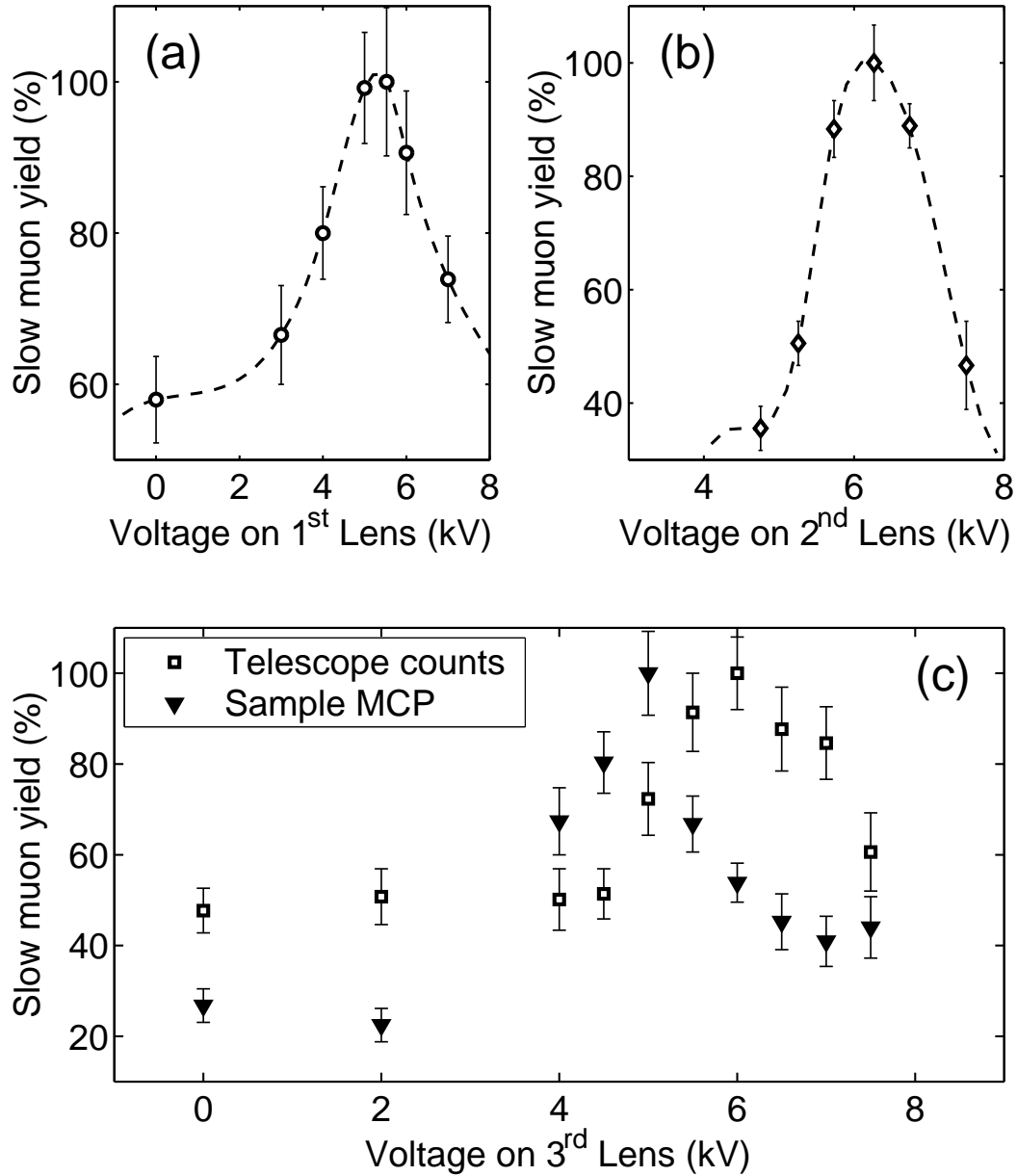


**Figure 17:** Tuning curves of the electrostatic Einzel lenses for an 8 kV initial accelerating voltage. Top figures (a) and (b) show tuning of lens 1 and 2 whose maxima in the slow muon rate, as measured by the MCP behind the second mirror (see text), are obtained respectively for  $V_{L1} = 5.5$  kV and  $V_{L2} = 6.25$  kV. The dashed lines serve only as guides to the eye. Figure (c) instead represents tuning of lens 3, performed by simultaneous monitoring of telescope coincidences in a quartz disk at sample position (shown with  $\square$ ) and count rates in the MCP located 32 cm behind it (shown with  $\blacktriangledown$ ). As  $V_{L3}$  increases, the focal length is shortened so that the peak in count rate, occurring first in the MCP detector, is shifted toward the sample position when  $V_{L3} = 6.0$  kV.

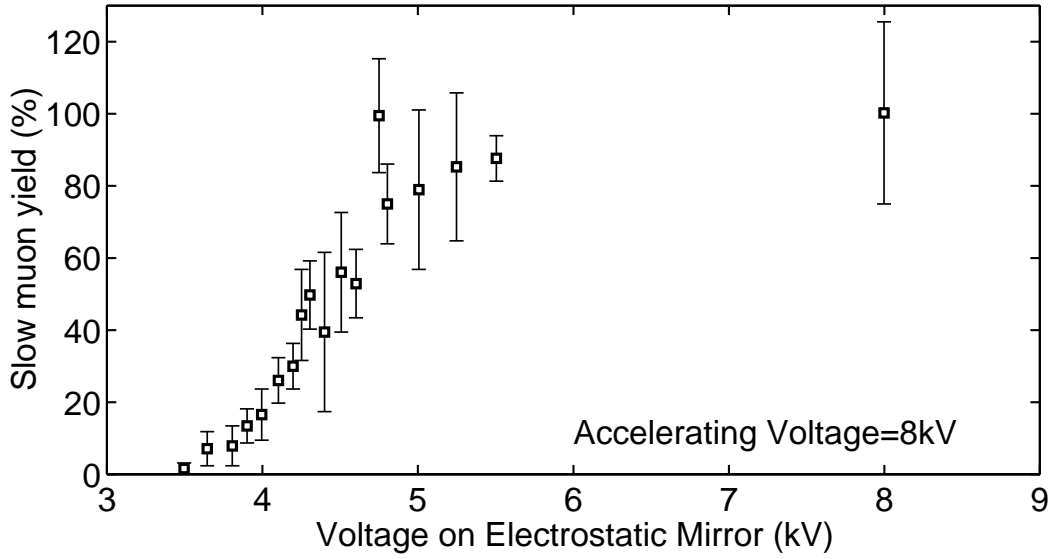


**Figure 18:** Measured slow muon rate as a function of the electrostatic mirror voltage with an accelerating voltage  $U_{acc}$  fixed at 8 kV. As the mirror voltage increases, the first slow muons are detected by the MCP once the theoretical threshold  $U_{th} = 1/2 2U_{acc}$  is reached. In the range between 4 and 8 kV there is a gradual rise in the number of detected muons. At 8 kV also particles with an energy up to twice  $eU_{acc}$  are transported (see also figure 24).

influences mostly the left and right sectors, whereas vertical steering affects the center and bottom sectors instead, whose count rate change in a complementary fashion.

Similar results were obtained for the second mirror too, even though the signals in this case were somewhat noisy and the geometric interpretation not so immediate. The poor performance of the second MCP is ascribed to the very long (70 cm) electrical feedthroughs needed to bring the signal out of the vacuum chamber, which implies significant cross “talk” among the four signals. This was a mandatory solution because, if the non UHV compliant electronics of the pre-amplifying stage were kept inside the vacuum tube, they would prevent us from reaching the very low pressures needed for a normal operation. On the other hand, the performance of the first mirror, with its much shorter wiring, was quite satisfactory. In this case 59(7)% of muons hit the central anode of 30 mm diameter, implying a 27(3) mm FWHM slow muon beam spot size, if a radial Gaussian distribution is assumed.

### 3.2.2.4 Experimental station for LE- $\mu$ SR Studies

The experimental station located at the end of the slow muon beam line (see figure 13) was planned with the goal to enable studies on different samples (typically thin films, surfaces and interfaces), for which slow muons are considered among the most appropriate probes. Since the present was mainly a development work, frequent sample station upgrades did take place at various stages of progress. Actually we can distinguish three of them, each identified by its peculiar features.

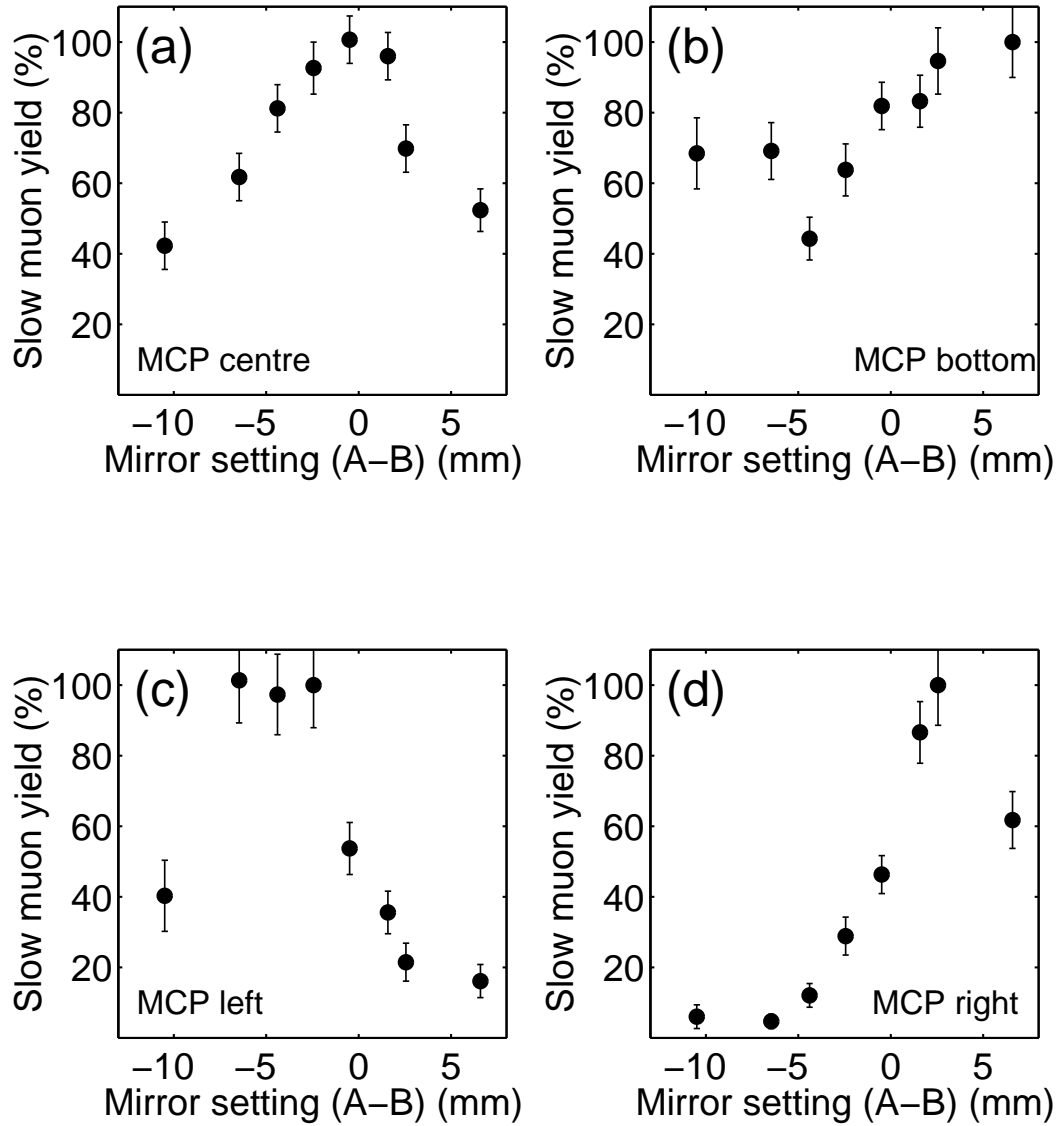


**Figure 19:** Horizontal tuning of the first mirror. Muons are detected by the four sectors of the MCP (see figure 20.b) positioned at the end of the second bend. The slow muon yield is plotted versus the difference in the settings of the two linear motion feedthroughs, labelled respectively A and B (the perfect alignment corresponding to  $A=B=9$ ). As the mirror is moved from left to right the respective MCP sectors (c) and (d) display opposite behaviours characterised by conjugate peaks and minima. The central anode (a) shows a maximum in case of symmetric alignment, whereas the bottom anode (b) does not display substantial variations as the mirror is being rotated.

- The first, very preliminary sample station, was used just to characterise the slow muon beam itself. An MCP detector was placed at the sample position and a simple arrangement of two telescopic pairs was used to detect positron decays. Mounted in opposite positions with respect to the vacuum tube, the plane rectangular areas of the scintillators covered a rather low total solid angle of 28.3(7)%.
- The next development step involved measurements on real thin film samples (described in chapter 5), thus imposing more stringent requirements from the sample station. The improved version (see figure 20) consists of custom designed cylindrical telescopes able to cover up to 85(3)% of the total  $4\pi$  solid angle. In practice the cylinders are evenly divided into four segments (top, bottom, left and right), each covering a  $90^\circ$  angle in the plane perpendicular to the vacuum tube axis. The considerable longitudinal extension of the scintillators ensures a good coverage of the whole sample area, except of course perpendicular to the vacuum tube itself. To achieve more detailed spatial information, both the inner and the outer cylinders were further split into two symmetrical halves along a plane passing through the sample position, thus resulting in a total of 16 scintillator counters, or equivalently, 8 telescopic pairs.

Another significant improvement consisted in the use of lead shielding (15 cm thick) of the whole experimental station, which substantially reduced the background due both to positrons from DevA beam as well as those coming from the neighbouring areas.

- A sample station including a liquid helium cryostat to perform low temperature studies, is foreseen in the near future. Moreover, an interlock chamber which provides *in-situ* sample cleaning, is expected to eliminate any dead times due to vacuum breaks between sample changes (refer to Conclusions for more detail).

In the actual setup a gate valve is employed to isolate the upstream production and transport sections from the sample station, thus allowing a quicker return to the normal UHV operating conditions. The magnetic field for the  $\mu$ SR experiments is supplied by a 27 cm long solenoid wound around the 127 mm diameter vacuum tube. Besides generating a rather uniform field, with less than 2% of measured inhomogeneity at the sample position, the solenoid provides the best alternative to improbable Helmholtz coils which would be too bulky to fit inside the telescopes and overall lead shielding. Simple calculations and successive measurements confirm that a 42 G magnetic field is produced when a 10 A current flows into the solenoid. To avoid damages to the scintillator counters the current was limited to this value, which during prolonged operation gave rise to a local temperature increase up to  $\sim 60^\circ$  C.

During the experiments the samples were fixed by thin wires on the vacuum tube axis. This solution reduces the background since only the muons which hit the sample are detected

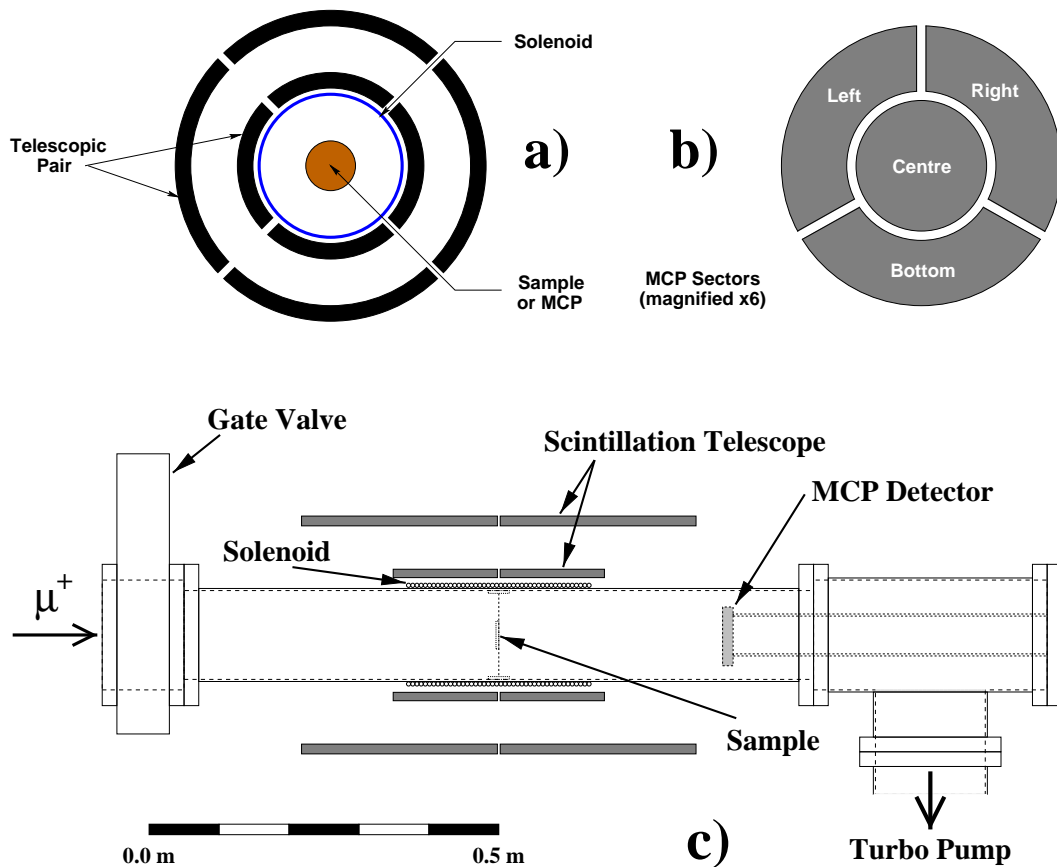


**Figure 20:** Schematic drawing of the experimental station at the end of the beam line, as used during thin film investigations. The 16 scintillators are symmetrically distributed in 8 telescopic pairs around the vacuum tube, which hosts in its center the sample suspended by thin wires. Top figures a) and b) show respectively a cross section of the tube and the four sectors of the MCP detector. The gate valve isolates the transport channel during sample changes. The MCP beyond the sample position detects the muons which are not implanted and therefore remain invisible to the telescopes.

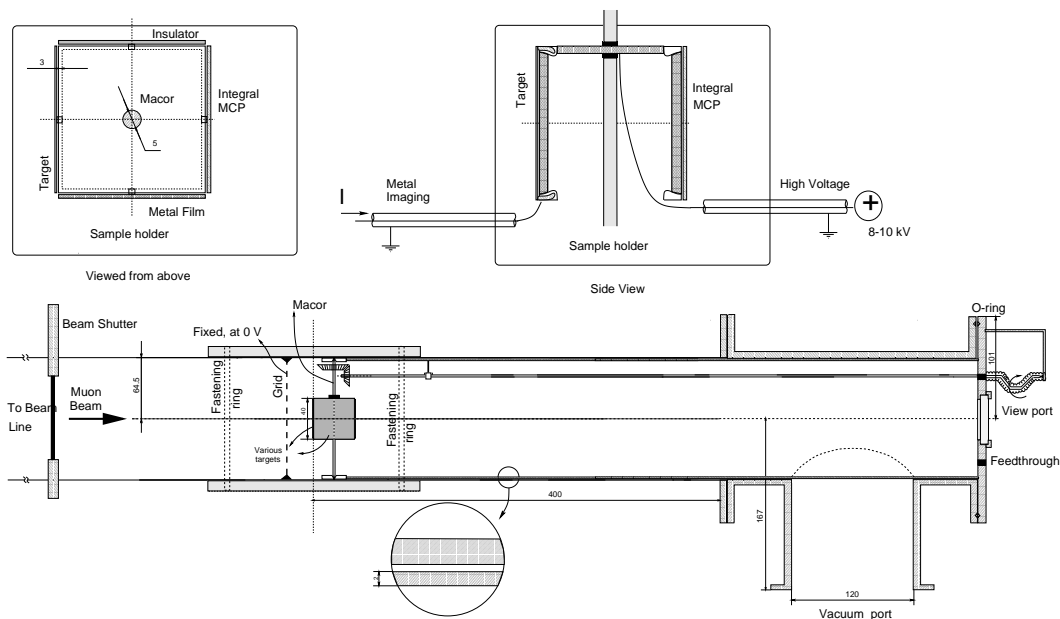


**Figure 21:** Layout of an alternative sample holder which uses a rotating cube to accommodate up to four different samples (see upper insets). A rotary feedthrough and an end viewport allow respectively to change the sample and to align it correctly. The high voltage grid, fixed inside the tube or attached to the sticks which carry the cube axis, is used to tune the energy of upcoming muons.

by the telescopes, the others pass through and their number can be determined by an MCP positioned near the end of the tube.

The same idea, namely that of exposing only the sample surface to the muon beam, was at the base of a more complex sample holder built in Parma (further details are given in the last chapter of [132]). It consists mainly of an open end cube, on which faces up to four different samples can be simultaneously mounted (see figure 21). The different specimens can then be studied by rotating the cube with a simple rotary vacuum feedthrough. A viewport at the end flange allows precise alignment of the sample surface perpendicular to the muon beam. The advantage of using this type of sample holder becomes clear if one takes into account that each time the sample area is accessed, approximately 12 hours of bake-out are needed to restore the base operating pressure.

### 3.2.2.5 Electronics and Data Acquisition System

The signals coming from the detectors are preprocessed using standard NIM electronic modules. As can be seen from figure 22, the timing for the start of data acquisition can be obtained in three alternative ways. These include the 50 Hz signal from the ISIS synchrotron extraction trigger, the signal from the Cherenkov counter located near the surface muon production target (which is due to electrons and positrons from  $\pi^0$  decay, cfr. section 3.2.1), or the signal from the muon beam counter placed in front of the cryogenic substrate. All the

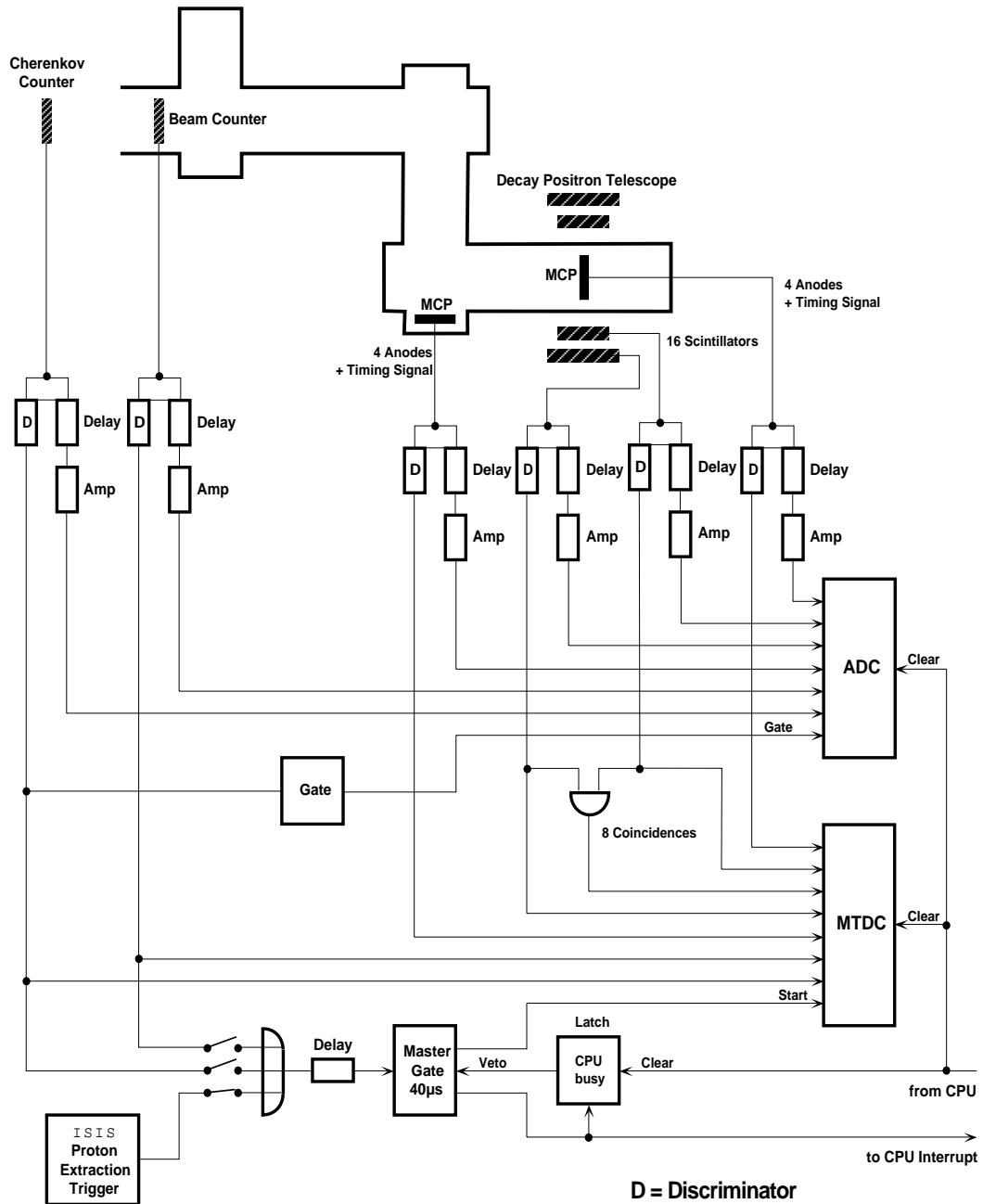


**Figure 22:** Simplified scheme of the electronics used for the slow muon experiment. The timing can be provided by three distinct sources: the ISIS synchrotron extraction trigger, the Cherenkov counter or the muon beam counter. The stopping signal for the  $\mu$ SR measurements is given by the coincidences at the scintillation detector telescopes (from [148]).

three starting signals, after appropriate delay and discrimination, are sent to a logical OR port, whose output will trigger the opening of the master gate with a fixed duration of 40  $\mu$ s.

The stopping signal for the  $\mu$ SR measurements is given by the coincidences at the scintillation detector telescopes. Similarly, the time-of-flight data are obtained by recording the signals originating at the MCP detector.

The data acquisition system is based on single event readout, which implies that all the acquired data within the opening interval of the master gate, i.e. Peak ADC, Flash ADC, etc., are contiguously stored in one event block. Since this technique, on the contrary of the common histogram filling used in particle data acquisition, retains the complete information about the experiment, it will allow sophisticated offline analysis, like application of background cuts or the study of correlations among various coincidences.

The front-end data acquisition uses VME based electronics. Each detector provides basically two types of information: timing signals, recorded by a 64 channel multi-hit TDC with a timing resolution of 1 ns, and analog signals, recorded by a Flash ADC, a Charge ADC and a Peak ADC.

A software driver, started by interrupting the VME single board CPU (ELTEC, Eurocom E5 (Motorola 68020, 16 MHz)) running OS9, handles the readout of the VME modules. The interrupt routine, triggered by mark signal generated at the end of the master gate, will read all the modules of the VME crate and successively write the data in binary format to a 2 MByte memory-module.

Every second the temporary stored data are transferred via a PCI-VME adapter (Bit3, Model 617) to a workstation (Digital, Alpha Station 200 4/166) which immediately writes them to the hard disk. To allow a quick online analysis, approximately half of the data are supplied to the experimenter, which thus can check detector performances, slow muon yield, background counts, etc. by running a routine based on the PAW (Physics Analysis Workstation [26]) program.

## Chapter 4

# Properties of the pulsed low energy muon source

IN the previous chapter we dealt with the development of the pulsed slow muon beam at ISIS with the aid of the moderator technique. The next step before performing measurements in thin films involved a thorough characterisation of all the relevant properties of the slow muon source. The present chapter is dedicated just to the systematic exposition of the measurements to study these properties, both of those depending on the type of moderator as well as those depending on operating conditions like temperature or pressure. We conclude with a theoretical overview which is an attempt to rationalise the experimental results. Note that, since this study was done in a collaborative work, much of the present material can also be found in the previously written theses like [86,148].

### 4.1 Beam spot size and slow muon yield

Both the beam spot size and the slow muon yield are two very important parameters that characterise a slow muon beam. Indeed, the *relative* muon production efficiency would be sufficient for comparisons among various moderator materials, only if all the other parameters could be kept constant. The knowledge of the *absolute* value of the yield instead, makes possible comparisons with data obtained in different conditions or even at other facilities. The size of the muon beam spot on the other hand, which depends both on the original surface muon beam section as well as on the slow muon transport and focussing system, is essential in the choice of the sample diameter.

#### Muon beam spot size

The beam spot size can be inferred from two different types of measurements, which make use of the decay spectra as detected by the telescopes. The first method consist simply in

recording the time-of-flight signal with and without a sample mounted. When the sample is present the spectrum comprises both the contributions from muons stopped in the sample as well as from those stopping in the walls of the vacuum chamber or decaying “in-flight”. In the other case instead, only the two last contributions are present. Once the sample diameter, the detection efficiency of the telescopes and of the MCP, together with the finite solid angle of scintillators are taken into account, one finds a 57(12) mm FWHM beam spot size.

The other method, although to a certain extent less precise, does not require the sample to be removed. By fitting the time-of-flight spectrum at long times one can discriminate the fraction of muons which decay “in-flight” from the others, since the former will give only a prompt peak, with a width equal to that of their transit time (easily evaluated since one knows the accelerating potential). Since in this case one cannot distinguish the muons stopped in the tube walls from those really implanted into the sample, the muon beam size will result somewhat underestimated.

### Slow muon yield

The measurement of the slow muon yield consists essentially in an integration of the area of the muon peak, as detected with the MCP placed at the sample position. The time structure of this peak closely resembles to that of the surface muon pulse (see figure 10) from which slow muons are generated. This is further confirmed by the 80(3) ns FWHM width of the time-of-flight spectrum and also by the same asymmetric distortion which can be traced back to the original convolution with the pion lifetime (26 ns) during muon production. To obtain the true yield value from the integration, apart from normalising to the number of incoming muons (measured with a photo-tube operating in a linear regime interfaced to a Peak ADC), one has to apply also some corrections for the detector and transport efficiencies and to cut part of the undesirable background. Let us consider these factors in more detail.

In their way from the moderator target up to the microchannel plate not all of the generated slow muons will be detected. Part of them are lost due to the finite transport efficiency of the system ( $\epsilon_{\text{trans}} = 78(2)\%$ ), another fraction decays during the time of flight up to the detector ( $\epsilon_{\text{dec}} = \exp(-t_{\text{tof}}/\tau_{\mu})$ ), and finally, from those reaching the MCP, there is still another “invisible” amount due to the detector’s finite efficiency, ( $\epsilon_{\text{MCP}}$ ). It follows that the total efficiency  $\epsilon_{\text{tot}}$ , arises as an outcome of these three components and therefore can be written as:

$$\epsilon_{\text{tot}} = \epsilon_{\text{trans}} \cdot \epsilon_{\text{dec}} \cdot \epsilon_{\text{MCP}} \quad (22)$$

The first factor is determined by the geometry of the apparatus, especially the positioning and diameter of the Einzel lenses. The second factor instead depends on the accelerating voltage  $U_{\text{acc}}$  through  $\epsilon_{\text{dec}} = \exp(-t_{\text{tof}}/\tau_{\mu}) \propto \exp(-1/\sqrt{U_{\text{acc}}})$ . In case of an 8 kV accelerating voltage one finds that  $\epsilon_{\text{dec}} = 58(1)\%$ . Due to the inverse square root dependence, going to

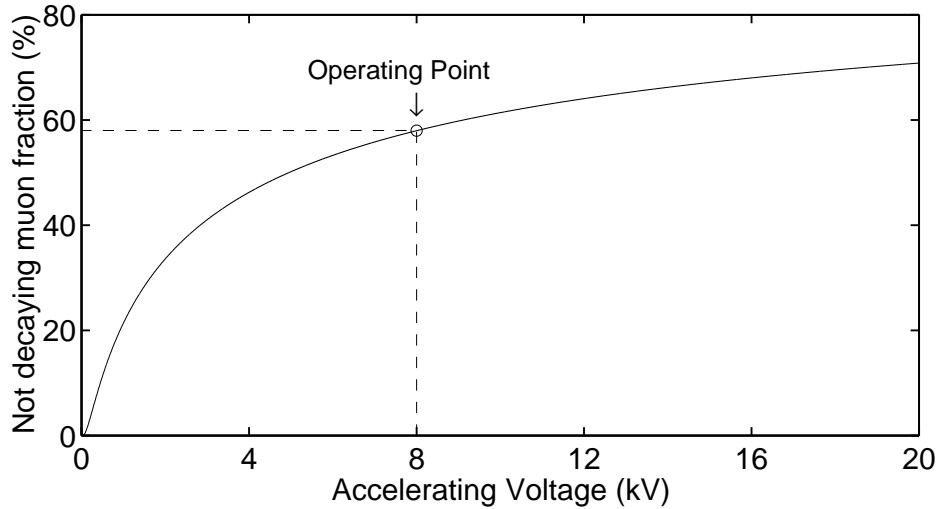


**Figure 23:** Fraction of muons which do not decay during their time of flight calculated as a function of the initial accelerating voltage. To the present operating condition  $U_{\text{acc}} = 8 \text{ kV}$  corresponds a muon “surviving” fraction of 58%. Note that a further increase in the accelerating voltage does not result in an appreciable gain in efficiency.

much higher voltages does not reduce very much the decay fraction (see figure 23) and, in addition, there are problems with electrostatic discharges which can severely damage the temperature sensing diodes. Therefore the actual choice of  $U_{\text{acc}} = 8 \text{ kV}$  represents the best possible compromise.

As for the detection efficiency  $\epsilon_{\text{MCP}}$ , it can be determined from measurements with the MCP placed at the sample position. If  $\epsilon_{\text{MCP}}$  were unitary, the events “seen” by the telescopes within a long enough time window (e.g.  $10 \mu\text{s}$ ) would be the same as the coincidences of MCP signals followed by a telescope decay events (within the chosen time interval). It is clear that taking the ratio of coincidences to that of the decay events alone will give the required MCP efficiency. Obviously, in a more accurate measurement one considers also the background rates which should be subtracted before evaluating the ratio. It is important to notice that neither the detection efficiency nor the solid angle of the telescope itself are needed for the calculation. The measured value of MCP detection efficiency turns out to be  $\epsilon_{\text{MCP}} = 64(5)\%$ . Therefore the total efficiency, given by the equation (22), amounts to  $\epsilon_{\text{tot}} = 29(2)\%$ .

Finally we briefly discuss about the cuts applied to reduce the background noise, which essentially originates from two different sources. The first one is given by the spurious signals generated in the MCP *after* a muon has been detected. In effect, each time a muon hits the MCP, it can also ionise residual gas components near the sensitive region of the detector, giving rise to aftercounts. The simplest way to get rid of these counts is to consider only the *first* event and ignore all the successive hits. The second source of background consists of events due to external sources, where we include also the hits arising from ions being detected

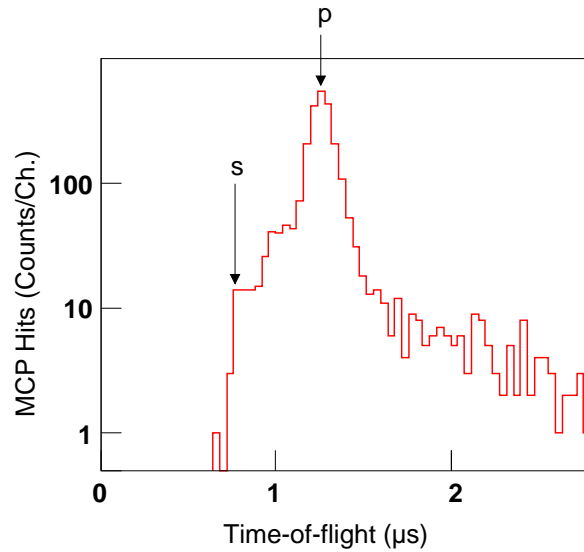


**Figure 24:** Muon time-of-flight spectrum for an 8 kV accelerating voltage as measured by the MCP at sample position. After the cuts mentioned in the text have been applied there is virtually no background (note the logarithmic scale). The peak  $p$  is due to the incoming slow muons, whereas the shoulder  $s$  at an earlier time ( $t_s = 1/\sqrt{2} t_p$ ) reflects the non perfect selectivity of the mirrors, which will transport also the particles with an energy up to twice  $eU_{acc}$  (adapted from [148]).

before a muon arrival or from ions whose muon “parent” could not be detected (we recall that  $\epsilon_{MCP} = 64\%$ ). The suppression of this further background can be operated by requiring a coincidence between an MCP hit and the successive detection (within  $10 \mu s$ ) of a muon decay in the telescopes. The resulting time-of-flight spectrum, after the two off-line cuts have been applied, is shown in figure 24. There is practically no background before the slow muon peak (shown with  $p$ ), whereas the small number of counts after the peak consists of residual random coincidences.

It is interesting to notice the presence of a shoulder  $s$  before the slow muon peak  $p$  even after the cuts have been applied. From the time of flights it is easily evinced that  $t_s = 1/\sqrt{2} t_p$ , corresponding to a factor of two in the respective particle energies. If now we recall that, when the voltage of the mirrors and the initial accelerating voltage are the same, the mirror reflectivity comprises the whole energy interval  $eU_{acc} \leq E_k \leq eU_{acc}$  the nature of the shoulder is readily explained (refer also to section 3.2.2.3 and in particular to figure 18).

## 4.2 Efficiency dependence on temperature and pressure

The study of the slow muon yield dependence on temperature and pressure was carried out with a twofold aim. The first one regards a practical problem, namely that of achievement of the highest possible slow muon production efficiency. The other instead was a more ambitious intent: to establish some general relationship between structural and morphological film

properties and its emission efficiency. The results we obtain confirm similar investigation performed also at PSI [97]. In the following paragraphs we consider in more detail the various types of experiments, concerning both the conditions during film deposition as well as those during the measurement itself.

#### 4.2.1 Deposition temperature dependence

The slow muon yield as a function of the temperature during film deposition can be investigated simply by varying the temperature of the substrate. The latter is adjusted by a conventional temperature controller which uses a silicon diode attached to the cryostat's cold finger as a sensor. With the help of an electric heater and by automatic (or manual) control over the helium flow valve, stable temperatures in the range 7–150 K can be attained.

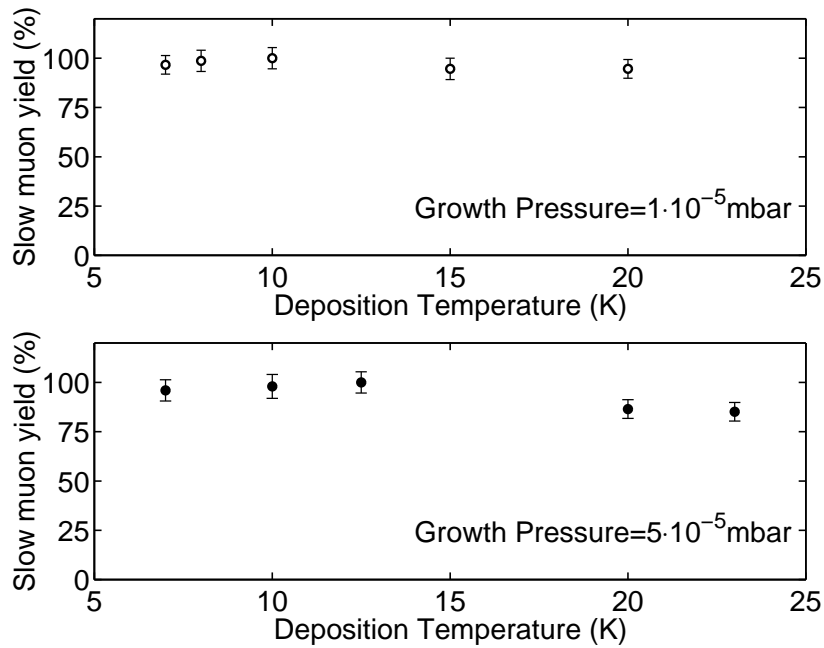
The deposition procedure consists first in the evaporation of the old film at approximately 70 K. Next the temperature is lowered to the required value and kept constant within 0.2 K, both during the growth of the moderator layer and the successive measurement. Two series of solid argon films were prepared, with argon pressures during deposition of  $1 \cdot 10^{-5}$  mbar and  $5 \cdot 10^{-5}$  mbar respectively. All the measurements were performed with films characterised by the same nominal thickness within 1 Å.

Figure 25 shows the results obtained for several deposition temperatures. For both series the moderator displays a very small dependence on temperature during growth. There is only a slight maximum in the range 10–13 K, which is more pronounced for the films prepared at a higher argon pressure. This is shown also by the higher excursion in slow muon yield which amounts to 5% for the films prepared at  $1 \cdot 10^{-5}$  mbar and to 15% in the other series.

These results, apart from confirming previous measurements [97], suggest that the temperature during the deposition of the rare gas film does not play a primary role as far as the slow muon yield is concerned, but rather influences in some indirect way other more important parameters. Before trying to find a possible explanation, which accounts for the moderation efficiency dependence on temperature, we report first also about the behaviour as a function of the annealing temperature, and postpone the interpretation of both cases to the end of the next section.

#### 4.2.2 Efficiency dependence on heat treatment

Other series of experiments were performed to study the dependence of slow muon yield on the thermal history of the frozen rare gas layer. This involves temperature cycling from the lowest value of 7 K, at which films were grown, to a higher value (variable from one measurement to the next) and then the return to the initial base temperature, where the measurement are performed. The duration of the annealing was fixed to a period of 10 minutes for all the



**Figure 25:** Dependence of slow muon yield on film deposition temperature. The different experimental data correspond to as many solid argon targets. The substrate temperature was kept constant both during film growth and the relative measurement. The argon deposition pressures were respectively  $1 \cdot 10^{-5}$  mbar (upper graphic) and  $5 \cdot 10^{-5}$  mbar (lower graphic). In both cases the moderator exhibits an almost insignificant dependence on the film growing temperature.

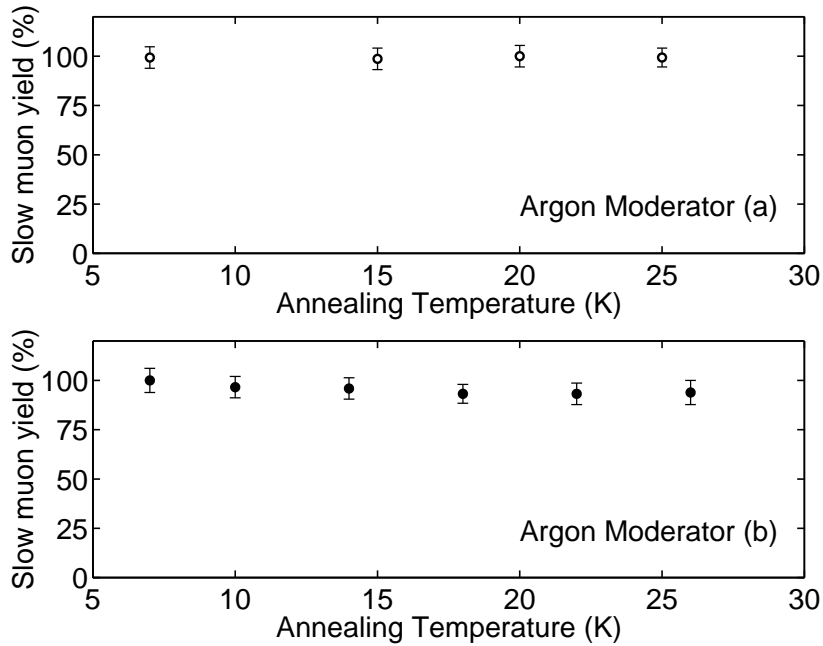
annealing temperatures  $T_a$  which were examined, whereas the experiments were carried out in an ever increasing  $T_a$  order.

Figure 26 shows the results obtained for different annealing temperatures with two similar argon films, (a) and (b), 180(6) nm thick and prepared at a  $1 \cdot 10^{-5}$  mbar argon pressure.

For the moderator (a), shown in the upper part of figure 26, the efficiency variations are smaller than the experimental errors, therefore one concludes that it does not manifest any dependence on annealing temperature. It is not so for the moderator (b) (lower part of the same figure), which exhibits a small systematic decrease of 7% in the range 7–18 K.

In conclusion, we can affirm that annealing has practically a very small effect on the slow muon yield of the moderator, at least in the condition in which it was performed (UHV, relatively low temperatures and not for a long time). Probably higher temperatures can induce a more substantial change in the film structure and therefore in its muon emission properties, but on the other hand they are more difficult to attain due to the higher film evaporation rate as the temperature increases.

A possible interpretation of the results shown in the last two sections considers the close relationship existing between film structure and its deposition or annealing temperature. It is long known [69] that films grown by direct sublimation (i.e. from vapour phase) form many



**Figure 26:** Dependence of slow muon yield on film annealing temperature. The solid argon layer is deposited at 7 K, then the moderator is brought to one of the annealing temperatures for  $\sim 0.2$  hours and finally returned to 7 K where all the experimental data are collected. The annealing temperatures were continuously increased from one measurement to the next. Both argon moderators (a) and (b), grown in similar conditions, show practically no dependence on annealing treatment.

random oriented crystallites and display a porous structure characterised by rather large voids, defects and granulous boundaries.

The existence of a weak maximum with respect to deposition temperatures, occurring at approximately  $\sim 10$  K, could be explained as a joint effect of at least two opposite factors. Indeed, as the deposition temperature rises, the grain size increases and the quantity of defects diminishes. This is associated to an improved moderation efficiency of the higher quality films, since here the muon transport towards the boundary occurs with fewer energy losses. On the other hand, the fact that the efficiency does not display a steady increase with temperature, indicates the presence of another contrasting factor. This is probably related to the degree of porosity of the film, which is proportional to the active surface area and therefore to the number of emitted epithermal muons. At higher temperatures there is an increase in film density and a contemporary reduction in film adsorption capacity, both of which agree with a diminished film porosity. This last feature explains also the reduced slow muon yield at higher annealing temperatures, found in case of argon moderator (b). Although only qualitative, these considerations seem to provide a good basic explanation that can be successively refined as more accurate data will be available.

### 4.2.3 Surface adsorbates and film ageing properties

There are two main pressure effects which could influence the slow muon production efficiency. The first one involves the residual pressure in the vacuum chamber, whereas the other regards the pressure of rare gas during film deposition. Since the latter influences directly the speed of deposition it will be considered in the following section.

As was shown with a simple example on page 40, the pressure inside the vacuum tube is closely related to the speed of impurity deposition on the cryogenic moderator surface. The presence of an impurity layer is supposed to attenuate the emission probability of the slow muons generated inside the moderator, by inhibiting their transmission through the surface and, therefore determining a constant decrease of the moderation properties in time. The most important components of the residual gas, as measured from the time-of-flight spectrum, consist mainly of water and protonated water clusters, but also of CO and CO<sub>2</sub>. The influence of their pressure on the lifetime of a moderator film has been shown in a previous work [97], where a base pressure of  $\sim 1 \cdot 10^{-10}$  mbar was shown appropriate for long term runs.

We investigated the film ageing process at even longer times in the cleanest possible conditions. This has a twofold goal: in view of future experiments on a permanently installed machine, one should know the duration of the moderator layer to maintain a reasonable slow muon production level. On the other hand the knowledge of the film deterioration rate is important for applying corrections to the decrease in yield, especially when several runs are performed with the same target (the study of slow muon energy distribution (cfr. *infra*) was such a typical case). Figure 27 shows the dependence of the slow muon yield on the time elapsed since deposition with the base pressure kept constantly at  $\sim 9 \cdot 10^{-11}$  mbar.

As expected there is a constant decrease in yield, which however is limited to  $0.26(2)$  hour<sup>-1</sup>, therefore allowing even experiments which last several days to be performed with the same target. Nevertheless, considering that maintaining the same target often is not important and the growth of a new film takes less than an hour, the preparation of a new moderator every 30–40 hours was a convenient choice.

To gain further insight into the problem of film ageing and the consequent efficiency decrease we performed another experiment. From the results shown in figure 27 it is clear that surface impurities play a crucial role in the drop of efficiency with time. But one can also ask himself whether the location of the impurity layer has some consequence on the ageing process. More precisely, if the impurities were located not on the solid-vacuum interface, but somehow “buried” well inside the moderator target, how would the efficiency change? To answer this question we carried out a series of experiments where an additional layer of argon was deposited on an already decreased efficiency argon moderator. Unfortunately, all the tests gave negative results, i.e. instead of the expected restore of at least the partial original efficiency, no variation in slow muon yield was observed after the fresh film growth.

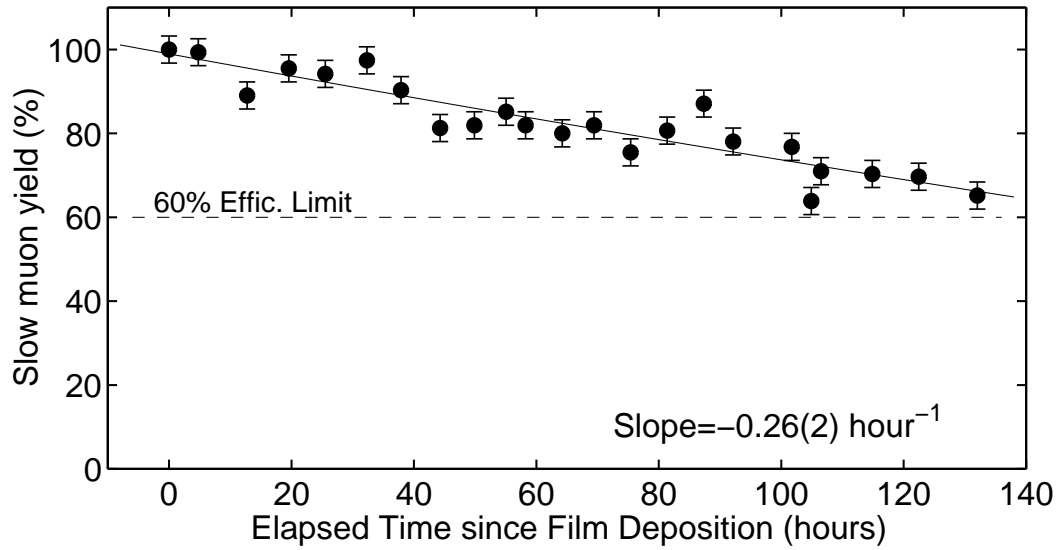


**Figure 27:** Slow muon yield from a solid argon moderator as a function of time elapsed since film deposition. With a decrease of  $\sim 26\%$  in 100 hours a critical limit of 60% for the total yield is reached only after more than 150 hours (or 6.3 days).

Probably the impurities, even though inside the moderator target, still retain their nature and therefore affect the slow muon emission in the same way as they did when deposited in its surface.

#### 4.2.4 Efficiency dependence on pressure

In this section we consider the influence of rare gas pressure on thin film properties and hence on slow muon yield. Variations in the deposition pressure are reflected in the speed of film growth which could therefore affect the structural properties of the moderator, typically its porosity and degree of disorder. As in the case of efficiency dependence on temperature, here also we do expect the presence of two opposite trends. On one side a large porosity should enhance the efficiency due to the increased epithermal muon emission from the larger active surface area. But, on the other hand, high quality films obtained at low deposition pressures, will determine a better muon transport, i.e. with fewer energy losses.

The experiment is expected to give an answer to the question whether there is a maximum in muon moderation efficiency and, if so, how pronounced it is. Two types of experiments were performed: in one the measurements were done *during* the film growth, whereas in the other the yield was checked *after* the film was deposited. The results from both of them are shown in upper and lower part of figure 28 respectively.

In the first experiment the film thickness cannot be kept constant, but instead we can arrange for a constant argon flow on the cold substrate during each of the efficiency measurements. Starting with a  $\sim 160$  nm thick argon layer and a substrate temperature of 7 K,

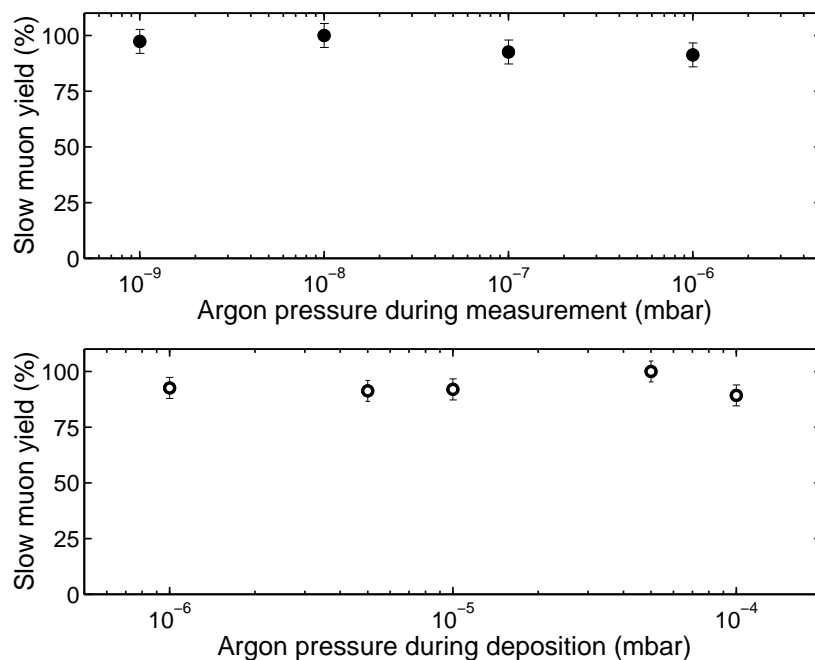


**Figure 28:** Efficiency dependence on argon pressure during film growth. In the upper graphic the measurements are performed *while* the growth is in progress (which limits the maximum reachable pressure). In the lower graphic the yield is checked *after* the film was deposited. In this case all the films have the same thickness, although very different deposition times were needed (from half a minute to more than half an hour). In both cases there is practically no evident dependence on growing pressure.

several deposition pressures (and therefore gas flows) were tested, spanning a range of more than four orders of magnitude (upper part of figure 28). The obtained results suggest a small efficiency decrease as the deposition pressure grows, but this can instead be due to the more significant increase in layer thickness for higher pressures (see section 4.4). These measurements can be thought also as a “dynamic” version of those regarding the addition of new film on the old moderator.

In the second case the argon films had all a thickness of 105(3) nm, but the change in deposition pressure from  $1 \cdot 10^{-6}$  mbar to  $1 \cdot 10^{-4}$  mbar implied quite different growing rates (0.5 nm/s and 42 nm/s respectively) and times. In this case the yield displays a weak maximum for  $5 \cdot 10^{-5}$  mbar corresponding to a growth rate of  $\sim 27$  nm/s (lower part of figure 28). All the successive moderator targets were prepared with this deposition speed.

The conclusion of the studies on pressure dependence is similar to those regarding the temperature, i.e. the pressure does not determine an appreciable change in the moderation properties of rare gas films.

### 4.3 Energy distribution of slow muons

The knowledge of energy distribution of epithermal muons has important practical and theoretical implications and therefore is one of the first to be measured once a new slow muon source is available (see e.g. figure 8). Unfortunately, the simplest measurement method i.e. the analysis of time-of-flight spectra, does not provide a purely energetic distribution but a rather mixed up quantity containing also some angular information. In practice, due to the considerable angular acceptance of the initial electrostatic accelerator, there might be several energy–angle combinations which belong to the same TOF. Hence, only an accurate simulation of the transport system, which considers also the shape of the surface muon pulse and a model for the angular distribution, could give a satisfactory energy spectrum [97]. The latter consists of the relative weights of the simulated monoenergetic spectra needed to fit a measured TOF spectrum.

In this work a new, more direct approach was used to study the energy distribution of slow muons, With the aid of decelerating potentials, applied between the moderator and the first stage of the electrostatic accelerator, we can “filter” all those muons whose energy is not sufficient to overcome the potential barrier. Thus, one expects a decrease in the number of detected muons as the retarding potential increases. To perform these experiments a newly designed accelerator was used, which eliminates almost completely the field “leakages” that affected some of the very first measurements (reference [18] contains a whole chapter dedicated to the study of potential distribution and field leakage). The new accelerator, together with the configurations used to measure muon energy distribution are shown in figure 29.

The dependence of slow muon yield from a solid argon moderator on the applied decelerating voltage is shown in figure 30. If in first approximation one neglects the muon angular distribution, the measured curve gives the integral of energy distribution function from the lower threshold, determined by the reverse potential  $V_r$ , up to infinity. Nevertheless, the dependence on angular distribution is clearly seen when negative decelerating (i.e. accelerating) voltages are applied. The saturation of the muon yield only at  $V_r \sim -150$  V (instead of the expected  $V_r \sim 0$  V) shows the gradual collection of muons at higher emission angles while  $|V_r|$  is being increased. On the opposite side, i.e. for high decelerating voltages, a persistent tail extending well beyond  $\sim 300$  V suggests the presence of energetic muons, although in a rather reduced number. The most interesting part of the spectrum is comprised indicatively in the range 0–15 V, shown in figure 30.b. Here one observes a rather linear decrease in muon yield, which corresponds to a flat muon energy distribution in this range. The remarkable closeness of the upper limit of linear behaviour to the argon energy gap ( $E_g = 14.2$  eV), together with the presence of a flat spectrum, which implies a lack of energy dissipation during muon moderation, both seem to confirm the “hot” muon model described in section 12.

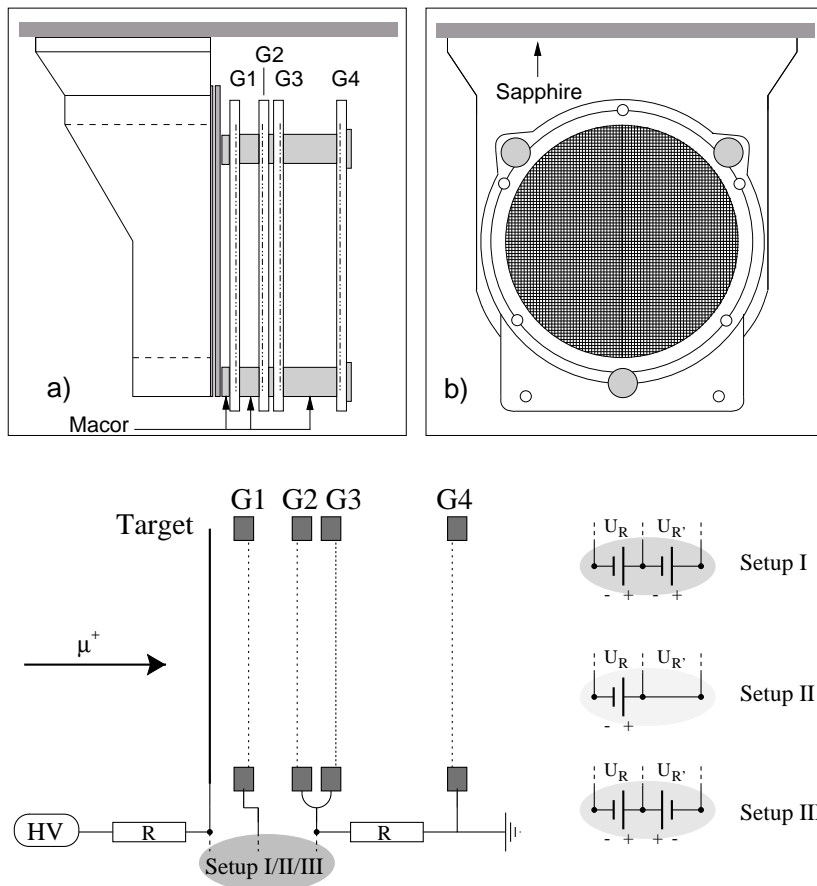


**Figure 29:** Layout of the accelerator in its three-stage configuration (top a and b figures), as used to measure the slow muon energy distribution through the application of retarding potentials in the first stage. The bottom figure shows the details of the electrical connections (taken from [18]).

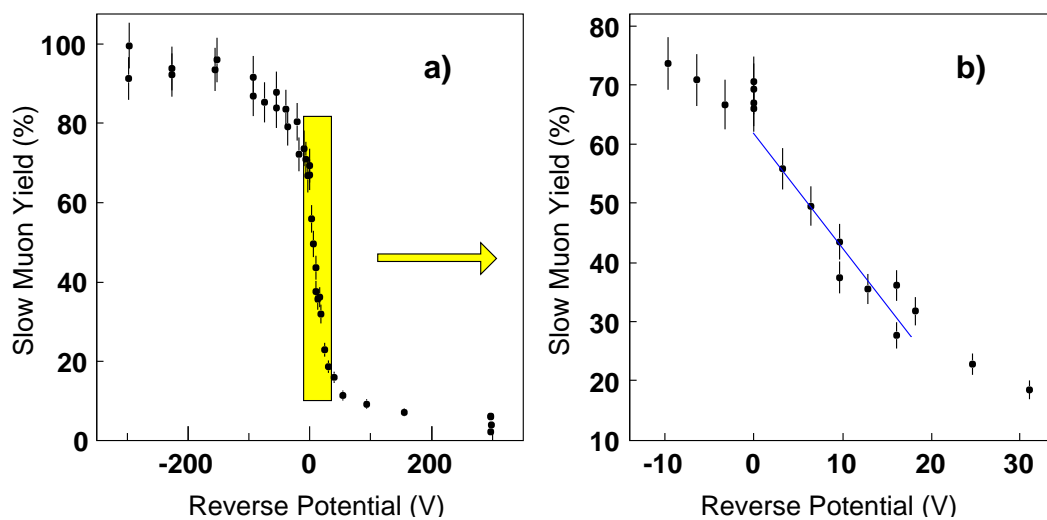


**Figure 30:** Slow muon yield from a solid argon moderator as a function of the applied decelerating voltage (left). The linear behaviour in the range 0–15 V suggests the existence of a flat energy distribution (right). The measurements were performed using the first setup shown in figure 29.

The superiority of the method of decelerating voltages upon time-of-flight analysis, was further confirmed by very detailed Monte-Carlo calculations [148]. Moreover, modelling the slow muon energy distribution with a constant value up to  $E_g$ , followed by an exponential decrease, resulted in simulated spectra in excellent agreement with the experiments.

#### 4.4 Efficiency dependence on film thickness and escape depth

The thickness of the moderating film is expected to influence the diffusion processes of emitted muons and hence to modify the slow muon yield. The experiments were performed both with argon and nitrogen layers, whose preparation and measurement were carried out in analogous conditions, i.e. same deposition and measurement temperature (7 K), growth at  $1 \cdot 10^{-5}$  mbar and measurement at  $\sim 2 \cdot 10^{-10}$  mbar of base pressure. In case of nitrogen, apart from the series of individually grown moderators, an incrementally deposited film was also measured. Figure 31 shows that argon and nitrogen exhibit basically the same type of behaviour, at least qualitatively. They both present a fast initial increase in yield, followed by a maximum at respectively 100 nm and 200 nm, and then by a final asymptotic decrease at approximately 65% of maximum level.

Since even for the largest grown film the thickness is just a fraction of micron, still very small compared to the muon stopping distribution (shown in figure 15), a possible effect due to the shift of moderator surface with respect to the substrate can be promptly ruled out. Hence, an explanation for the observed behaviour should be sought in some particular microscopic effect. There exists a simple model [97] which tries to explain the yield dependence on film thickness by assuming both a constant muon moderation efficiency and in meantime a exponentially decaying emission probability. It is this last feature which leads to a *saturation* of yield when a typical distance called the *escape depth* is exceeded, since any further increase in film thickness will not contribute anymore to slow muon yield. The analytical formula giving the slow muon flux  $j$  as a function of film thickness  $t$ , with the escape depth  $L$  as a parameter, is:

$$j(t) = N_\mu L \tanh\left(\frac{t}{2L}\right). \quad (23)$$

Typical escape depths  $L$  for argon and nitrogen as given in [97] are  $67 \pm 5$  nm and  $50 \pm 10$  nm respectively. Our data however, cannot be fitted reliably by using the formula (23), since they present a clear maximum not foreseen in the previous model and not detected in the measurements performed by the group at PSI. To further evidence the presence of the maximum, two measurements with very large moderator thickness were performed, giving still lower yields with respect to the asymptotic level.

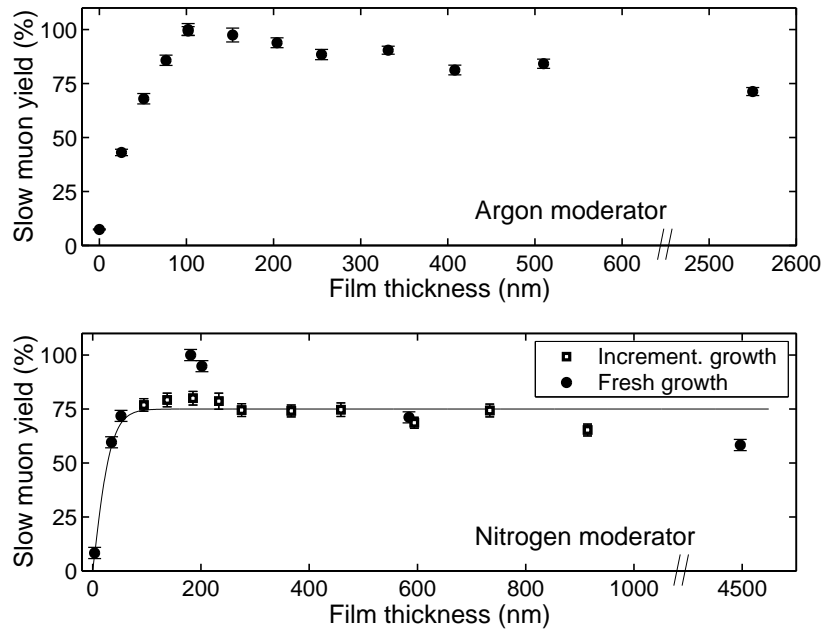


**Figure 31:** Dependence of slow muon yield on moderator film thickness for argon (top) and nitrogen (bottom). Both moderators show qualitatively a similar behaviour, characterised by maxima at 100 nm and 200 nm respectively. For nitrogen also incrementally grown films were measured. These data are the only to be satisfactorily fitted with the model given by equation (23) (see text).

A possible clue to resolve the apparent contradiction with the results obtained at PSI, would be to consider the conditions in which the films were grown in the two cases. Indeed, when we repeat the measurements with incrementally grown nitrogen films, we find that the maximum almost disappears substituted by a gradual saturation of the yield, as shown with open squares in the lower part of figure 31. A possible explanation for the maximum in slow muon yield considers the details of the film growth process (see also [148]). As is well known, at the beginning of growth the deposited material concentrates in islands characterised by a complex fractal structure, rather than creating uniform layers [113]. This is true also for the rare gas solids, which for small thicknesses display a very corrugated and irregular surface [69]. It is this very large surface to volume ratio to enhance the slow muon yield in the first stages. However, for thick enough films the islands start to “melt” with one another. The corresponding layer thickness provides a maximum in slow muon yield, since any further growth of the film will just make the surface smoother and hence diminish the moderation efficiency.

In conclusion we can affirm that the escape depth model in its present form, although essentially correct, does not provide a satisfactory agreement with the measurements. Nevertheless, the addition to this model of a *variable* coefficient, to allow for a varying active surface area during film growth, should restore its ability to accurately describe the experimental data.

## 4.5 Efficiency dependence on moderating material

The slow muon yield has been measured for several moderating materials, both to find one that shows a large efficiency and also to gain an insight on the moderating process itself. Besides the rare gas solids, favoured by their large energy gaps and low phonon energies, other materials like frozen carbon dioxide, solid nitrogen and even bare substrates of aluminium and diamond were investigated. All the measured efficiencies, together with the band gaps of the respective materials are shown in table 3. We recall that the reported values of *absolute* yield depend significantly also on the momentum width of the original surface muon beam (see section 3.2.2.2), and that the relative values are sufficient for an efficiency comparison.

Moderator	Temp. (K)	Energy gap (eV)	Efficiency ( $10^{-5}$ )
Argon	11	14.2	2.9(4)
Krypton	11	11.6	0.22(4)
Xenon	11	9.3	0.04(3)
Nitrogen	7	15.1	2.1(3)
Carbon Dioxide	7	8.1	0.12(2)
Aluminium	7	0	0.18(2)
Aluminium	300	0	0.10(2)
Diamond	7	5.45	0.07(1)
Diamond	425	5.45	0.06(1)

**Table 3:** Muon moderation efficiencies for various materials. The respective energy gaps and measurement temperatures are also shown. The data correspond to slow muons generated from a surface muon beam characterised by a 26.5 MeV/c momentum and a momentum spread of 10%. Note the close correlation between the band gap energy and moderation efficiency in case of frozen noble gases.

Argon, characterised by the highest energy gap among the examined solid rare gases<sup>1</sup>, displays the best slow muon generation efficiency,  $2.9(4) \cdot 10^{-5}$  per incoming surface muon. It is followed by solid nitrogen, another high gap insulator, which shows an efficiency amounting to 75% that of frozen argon. On the other hand, krypton and xenon show considerably reduced yields, even though their energy gaps are only 18% and 34% lower than that of solid argon. The same holds true for another intermediate band gap material as carbon dioxide, which has proven quite inefficient as a muon moderator.

The bare substrate, consisting of high purity, 320  $\mu\text{m}$  thick aluminium, was used to study the role of energy gap in moderation efficiency. The measurements, performed both at room

<sup>1</sup>A solid neon film with  $E_g = 21.6\text{eV}$  is expected to perform even better, but it is rather difficult to grow because of the very low binding energy which implies a substrate temperatures lower than 7 K (see also section 3.2.2.1).

temperature and at 7 K, gave very poor slow muon yields, as expected for materials without a gap like metals. Surprisingly however, there is a remarkable difference in the relative yields at the two examined temperatures. The existence of an almost doubled efficiency at low temperatures is still unclear, even though one might argue that it is somehow related to the unavoidable presence of a thin oxide layer on top of the aluminium substrate.

Diamond, contrary to the weakly bound van der Waals solids, is characterised by very high phonon energies and a Debye temperature of 2200 K, but at the same time it displays a considerable energy band gap of 5.45 eV. The sample consisted of four  $20 \times 20 \text{ mm}^2$  squares of  $120 \mu\text{m}$  thick diamond films, grown at low pressure by chemical vapour deposition (CVD). Special arrangements of the sample holder were needed to fix the sample and to apply the accelerating voltage. The measurements performed at 7 K and at 425 K gave very low efficiencies of muon moderation in spite of the presence of the band gap. The time-of-flight spectra show a very broad energy distribution, where the slow muon peak is heavily blurred by the rest of the spectrum extending towards higher energies. The results found for diamond reinforce those from previous measurements on LiF and SiO<sub>2</sub> [99, 97], characterised respectively by  $E_g = 14.1 \text{ eV}$  and  $E_g = 9 \text{ eV}$ , showing that the existence of a relevant band gap alone is not sufficient to provide high muon moderation efficiencies. On the other hand, the low efficiency of a *par excellence* covalently bound insulator such as diamond, refutes the widespread conviction that the poor muon moderation properties of LiF and SiO<sub>2</sub> are attributable to their ionic bound character.

## 4.6 Theoretical overview of muon moderation processes

At the end of each of the previous sections, short conclusions regarding the particular measurements were given. The goal of this last section is to provide an organic theoretical overview about all the performed experiments, without the aim of being exhaustive (a thorough exposition regarding the present status of theoretical understanding, is given e.g. by Morenzoni in [95]). Before going into details it is necessary to point out that up to now the models put forward to explain the generation of epithermal muons have been mostly qualitative. This denotes that our current knowledge is still far from being complete, as demonstrated by the example of diamond, which was measured in the hope of finding a very promising muon moderator ...

### 4.6.1 Stopping processes for low energy muons

The processes taking place during the stopping of particles in matter are of great practical interest since in almost all the experiments in nuclear and particle physics the obtained information is a direct consequence of the interaction of charged particles with the detector. Here

we give a somewhat lengthy exposition since this topic is important also for the experiments described in chapter 6, where the problem of range and range straggling of muons in matter is discussed.

When a charged particle enters a given material it will break the existing equilibrium and trigger a series of events, which correspond to the response of the medium to the externally added charge. Typically the electrons can be “pulled apart” and subsequently recaptured by the ionic cores or valence states. Coherent polarised structures are formed and, in some cases, also *dynamic screening* from electrons promptly responding to the Coulombian field of the moving charge can arise. Furthermore, oscillatory perturbations (surface plasmons) are associated with the particle entry interface [44]. Therefore it is clear that the passage of charged particles through matter (an intricately coupled system) is a problem that still today represents a difficult task, both regarding its comprehension as well as its experimental study.

A charged particle passing through matter will lose its energy mainly by ionisation and excitation of the nearest to its trajectory atoms. The quantity  $dE/dx$  used to express the energy loss per unit path is called the *stopping power* of the medium [141]. It is determined by many complex mechanisms, whose relative weight varies not only for particles with different masses, but for the same particle also as its energy changes. Simple approximations are possible in case of high energies, leading to analytical expressions for the relative stopping powers; for low energies on the other hand, this is either very difficult or simply impossible.

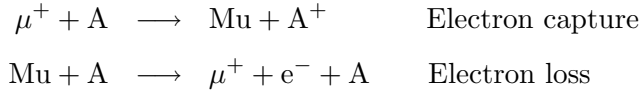
The study of muon energy loss in matter can be conveniently divided into three different regimes if a comparison between the muon velocity  $v_\mu$  and that of the electrons  $v_e \sim v_0$  ( $v_0 = \alpha c$  – Bohr velocity, with  $\alpha \simeq 1/137$  – fine structure constant) is made [130]:

**High energies** ( $v_\mu \gg v_0$ ): At high energies, and hence at high muon velocities, the stopping occurs mostly for *electronic excitation* and *ionisation*. In this regime, called also the Bethe–Bloch regime, the energy loss practically does not depend on the stopping medium and its calculation is rather simple [9, 141]:

$$-\frac{dE}{dx} = \frac{2\pi n z^2 e^4}{mv^2} \left[ \ln \frac{2mv^2 W_{\max}}{I^2(1-\beta^2)} - 2\beta^2 - \delta - U \right] \quad (24)$$

with  $n$  the electron concentration in the stopping medium measured in  $\text{cm}^{-3}$ ,  $m$  the electron mass,  $v$  and  $z$  the velocity and charge respectively of the incident particle (muon),  $\beta = v/c$ ,  $I$  mean excitation potential,  $W_{\max}$  maximum energy transferred from the charged particle to the electrons,  $\delta$  and  $U$  corrections for the density effect and for the inner shell exclusion in case of low velocities. Since this is a rather general formula, valid for  $\beta \geq 0.1$ , one can apply it to surface muons and find that they will follow the Bethe regime from  $E_\mu^0 \simeq 4.12 \text{ MeV}$  down to  $E_\mu \sim 530 \text{ keV}$  without particular differences among various materials.

**Average energies** ( $v_\mu \sim v_0$ ): When the muon velocity is of the same order as that of the electrons in the moderator, one has the so-called *charge exchange* regime. The matching electron and muon velocities give rise to processes which are typically represented by:



The captured electrons form bound states with the moving muons giving muonium atoms. Muons follow the charge exchange regime for energies  $3 \text{ keV} < E_\mu < 12 \text{ keV}$ . Essentially the electron capture follows three possible ways: a) electron transitions from bound states of an atom to bound states of muonium; b) Auger processes; c) resonant processes [3, 114]. The electron loss occurs in an analogous fashion. Even though at the beginning both processes have equal probabilities, as the muon energy decreases the electron capture becomes more important. Hence, at lower energies muons are mostly found in a bound state, i.e. as neutral muonium atoms. Since the muon energy loss depends heavily on its charge status, this regime is characterised by strong variations in stopping power.

**Low energies** ( $v_\mu \ll v_0$ ): This regime sets in when the muon energy drops below the threshold of  $\sim 2 \text{ keV}$ . The most important energy loss process is the elastic scattering of the muon with the atoms, even though a small contribution from electronic excitation still persists. The stopping power can be calculated only for the gas phase, where with the assumption of a uniform electron density and by using the linear response approximation one finds [44, 120]:

$$-\frac{dE}{dx} = z^2 \frac{2v}{3\pi} \left[ \ln \left( 1 + \frac{\pi}{\alpha r_s} \right) - \frac{1}{1 + \alpha r_s / \pi} \right] \quad (25)$$

with  $\alpha = (4/9\pi)^{1/3}$ ,  $v$  and  $z$  velocity and charge of the particle, and  $r_s$  a parameter which describes the electron gas density. This formula is valid under the assumption of an exponential shielding of the electric potential due to the charged particle. A similar result has been found also by Lindhard et. al. [80]. The equation (25) can be successfully applied to metals, if one assumes a free electron model for the electrons of the conduction band. Nevertheless, the same equation cannot be used in case of semiconductors and even worse for insulators, where due to the presence of an energy gap the conduction band is very scarcely populated. The phenomenology at low energies is quite rich and complex, since it should account both for contributions arising from elementary excitations as well as those from collective phenomena. Unfortunately, due

to this complexity, neither a valid theoretical description nor sufficient experimental data exist to date regarding the charged particles in the low energy regime.

The muon energy loss from the MeV range down to some eV is shown schematically in figure 32, where approximate time scales for each stage are also shown.

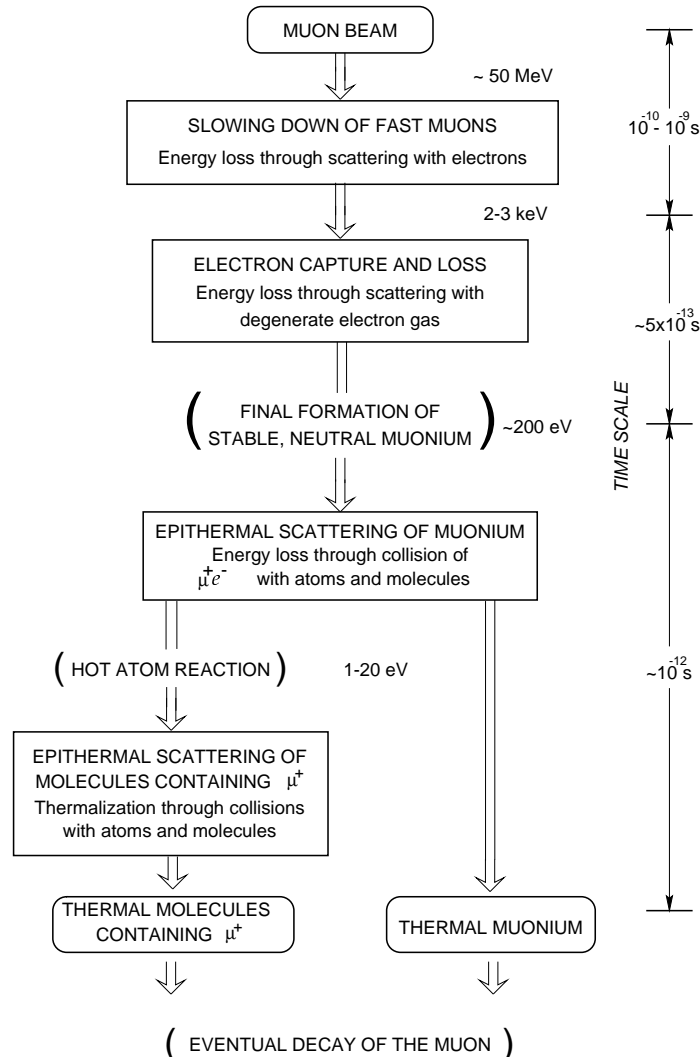


**Figure 32:** Flow diagram showing the principal stages of energy loss of muons in matter. On the right side an approximate time scale for each stage of the process is also reported (from [21]).

Note that, whereas all the previously described regimes contribute to muon energy loss, only the last one is relevant for the description of transport and emission of the already low energy muons.

Beside the energy loss due to electronic scattering, there exists processes like the elastic collisions where atoms as a whole are concerned. Although irrelevant for the energy loss itself (at least at high and average energies), they are fundamental in determining the range straggling, since during these collisions the charged particle changes continuously its direction

of motion. Thus the muon transport can be roughly divided into two main stages: a first one extending down to  $\sim 200$  eV, where there is a relevant energy loss but almost no scattering with the muons moving along straight lines, and a final stage dominated by elastic scatterings, characterised by a modest energy loss and enhanced diffusivity.

#### 4.6.2 Solid rare gases as muon moderators

In section 12 we gave a brief outline of the “hot” muon model, based on the equivalent counterpart for the low energy positron emission. Here, taking into account the previous considerations and the characteristics of frozen noble gases, we try a more basic level approach.

The very fact that the molecular and rare gases exists as solids only at relatively low temperatures is a simple and direct consequence of their very small interatomic bounding energies (due only to the van der Waals forces from fluctuating dipoles). Typically this energy is of the order of  $\sim 0.08$  eV/atom for solid argon or nitrogen and is reflected also in their very low phonon frequencies ( $\hbar\omega \sim 8$  meV for both Ar and N<sub>2</sub>). Furthermore, the low binding energy together with the small electronic coupling imply that the atoms in the solid will essentially retain their gas state properties and therefore it is possible to consider them simply as a particularly dense gas. The most significant consequence of this is the possibility to neglect complicate many body effects during epithermal muon moderation and transport, and to consider only binary interaction with the atoms of the medium.

The other important feature of the solids of rare (molecular) gases is the presence of relevant energy gaps (see table 3) of the order of  $E_g \sim 15$  eV. This high excitation threshold will prevent any further muon energy loss once its energy drops within the “forbidden” gap. The high energy gaps associated to the low acoustic phonon frequencies suggest modest energy loss during transport of epithermal muons towards the film interface and therefore appreciable epithermal muon yields. The reduced stopping power of the medium at very low energies implies also unusually large escape depths, as experimentally verified.

Now we can describe a hypothetical scenario which tries to explain the epithermal muon interaction with the stopping material. The low energy muon ( $E_\mu \simeq 10$  eV), characterised also by a relatively small velocity ( $v_\mu \simeq 10^5$  m/s), approaches one of the atoms of the van der Waals solid. Because of the high energy gap of the material the muon cannot excite the electrons and still less ionise them. It will simply deform *adiabatically* the electronic cloud and break its symmetry. The electrostatic interaction with the positively charged nucleus increases as the muon approaches it, because of the ever reducing electronic shielding. Since the atoms is bound in a crystal (although by very weak forces) it will share its interaction with the nearest neighbours giving rise to phonon creation or absorption. However, there is an essential difference in the time scales of muon interaction compared to the period of lattice

vibration. The first is of the order of  $\tau_{\text{int}} \simeq a/v \sim 10^{-15}$  s, where  $a$  is the lattice parameter and  $v$  the muon velocity. The other is at least 100 times larger, since  $\tau_{\text{ph}} \simeq 1/\omega_{\text{ph}} \sim 10^{-13}$  s, with  $\omega_{\text{ph}}$  a typical phonon frequency [95]. As long as  $\tau_{\text{int}} \ll \tau_{\text{ph}}$ , the recoil of the atoms is almost free and the “fast” moving muons cannot interact appreciably with phonons.

This last point can perhaps explain the negative result of the experiment on diamond. The expectation of a high muon yield from diamond was based on the possible existence of a relevant *recoilless fraction*, where the muon would be scattered without variations of its kinetic energy in a series of elastic events. Probably in this case, the much higher phonon frequency determines both a better matching of the muon interaction time with the lattice vibration period and also a higher energy loss per event with a consequent low epithermal muon yield.

As stated at the beginning of this section, our understanding of the processes controlling the muon moderation in matter is still at a qualitative level. There are several problems that still require an answer among which we can list: the precise role of the *interplay* between the high energy gap and the very low phonon frequencies, the question of muonium contribution to the epithermal muon yield: does it compete with or helps their production, the deeper understanding of yield variation with film thickness, etc.

## Chapter 5

# Experiments on thin films using epithermal muons

THIS chapter is devoted to the description of various experimental studies performed with the newly available pulsed epithermal muon beam. The very first experiments (mostly described in the previous chapter) focused on the properties of the slow muon beam itself rather than on the investigation of new physical systems. For example, the goal of one of the initial  $\mu$ SR measurements was the study of the degree of muon polarisation, with the MCP detector being used as a sample. Only when an electrostatic decelerator was mounted inside the vacuum tube, thus offering the possibility to tune the beam energy in the range  $0-V_{\text{acc}}$ ,  $\mu$ SR experiments on real systems could be performed. This, associated to the advantage of a narrow energy distribution of slow muons arising from rare gas moderators, permits investigations of thin films and interfaces. Furthermore, the pulsed feature automatically provides the implantation time, essential to retain the intrinsic energy resolution of the beam, since no other energy degrading devices are needed for the timing. The experiments described below deal respectively with the mapping of the implantation profile of epithermal muons and the study of a typical magnetic thin film.

### 5.1 Implantation profile of epithermal muons<sup>1</sup>

When using ordinary surface muon beams, characterised by their  $\sim 4$  MeV of kinetic energy and some hundreds of microns of typical range, the only concern of the experimenter is to make them stop well within the bulk of the sample. It is not so for beams of epithermal muons where, to take full advantage of their tunable energy (from 0 to 10 keV) and correspondingly much reduced stopping range (0 to 100 nm), one needs an accurate knowledge of the beam

---

<sup>1</sup>This experiment was chosen for demonstration purposes because of its simplicity. In chapter 6 however, we show a new method with clear advantages for studying the stopping profile of epithermal muons in metals.

implantation profile. This in turn allows the slow muons to be stopped only around a given material depth, as e.g. in an interface or a surface, and consequently to study its properties. The investigation of the implantation profile is motivated also by the need to test the codes that simulate the transport of charged particles in matter. As stated in the introduction, most of the measurements where the stopping range is an essential parameter rely on simulations. Nevertheless, in the limit of very low energies, the reliability of the existing computer programs becomes rather questionable.

Since the problems of range and straggling of muons in matter, as well as those related to the Monte Carlo simulation codes, will be dealt with in much more detail in a dedicated chapter (7), in what follows we give only the essential information needed to understand the experiments.

The basic idea, frequently used when determining muon stopping profiles, relies on the very different precession frequencies of muons in a diamagnetic state ( $\mu^+$ ) as compared to those which thermalise as muonium atoms (Mu). The use of a metal film on an insulating substrate is therefore a good choice, since one can experimentally distinguish the  $\mu$ SR precession of free muons in the metal from the muonium triplet frequency in quartz (see figure 33). In this case the equation (19) reads:

$$N(t) = N_0 e^{-t/\tau_\mu} [1 + A_\mu G_\mu(t) \cos(\omega_\mu t + \phi_\mu) + A_{\text{Mu}} G_{\text{Mu}}(t) \cos(\omega_{\text{Mu}} t + \phi_{\text{Mu}})],$$

where the various symbols have the usual meaning and in particular  $A_\mu$  and  $A_{\text{Mu}}$  are the muon and muonium asymmetry, whereas  $\omega_\mu$  and  $\omega_{\text{Mu}} \simeq 103 \omega_\mu$  are their respective precession frequencies. One can measure the fraction of muons stopped in each material, i.e. the implantation profile, by simply following the variation of the diamagnetic signal asymmetry  $A_\mu$  as a function of the implantation energy.

A 20 nm *copper film on quartz substrate* was selected to demonstrate the depth slicing properties of the ISIS facility when the muon energy is selected by means of a decelerating device. In terms of depth slicing, the spatial sensitivity and resolution depend not only on sample material but also on muon straggling. For the specific case of copper, we expected to cover the range of depths from 1 to 100 nm.

The sample was sputtered in argon atmosphere. The surface of the substrate as well as that of the sputtered film were examined by Atomic Force Microscopy (AFM): the very modest roughness of the surface ( $\sim 7$  nm deep with an average angle of  $0.9^\circ$ ) allows reliable slicing experiments. Due to presently unavoidable exposure to atmospheric agents, Auger analysis of the surface indicated the presence of 2–3 nm of  $\text{Cu}_2\text{O}$ . The muon precession in  $\text{Cu}_2\text{O}$  is well known, it is quite different from the precession in metallic copper and cannot be detected within the ISIS frequency passband. The presence of this oxide layer offers therefore a challenge to the slicing experiment to be performed.

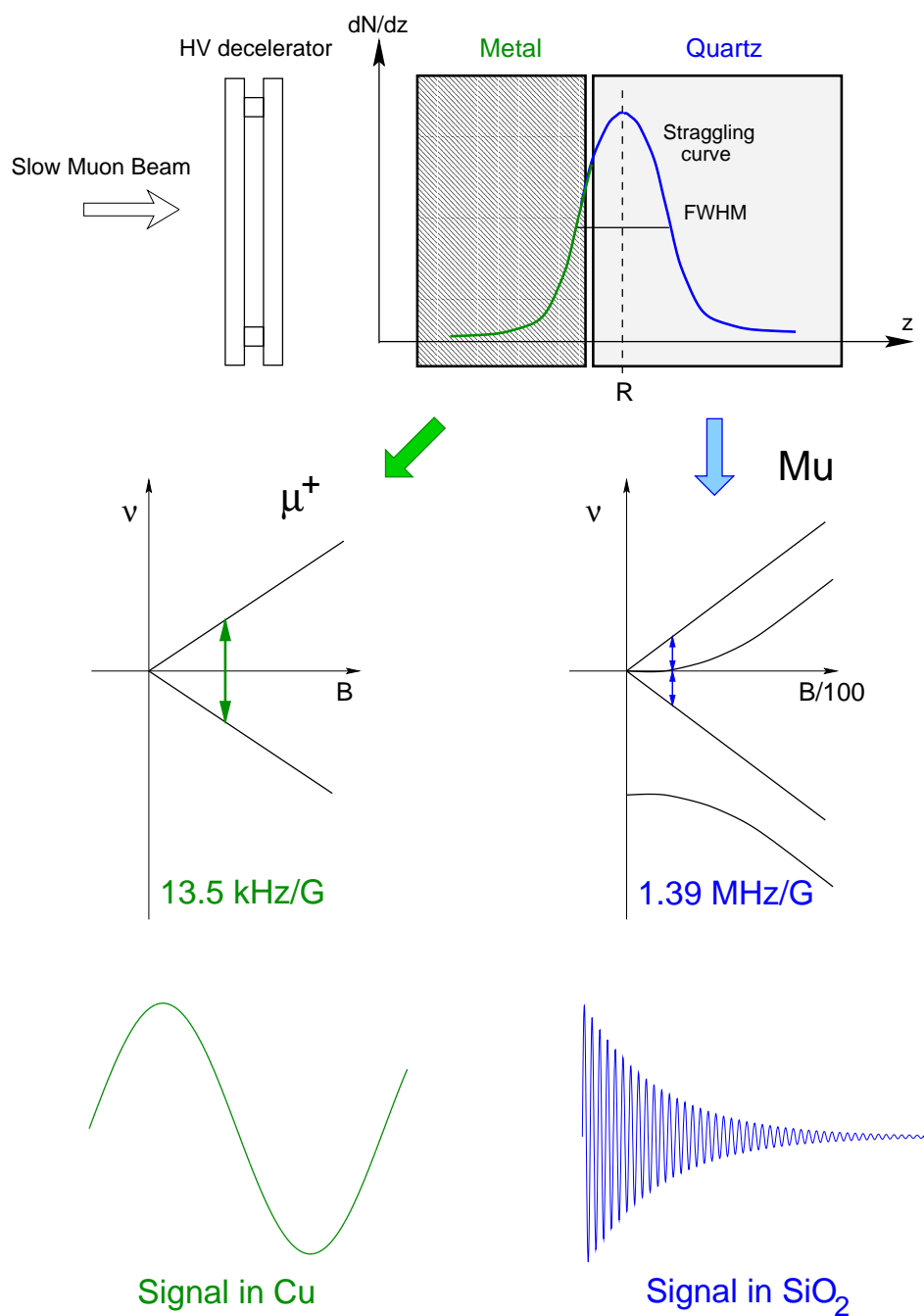


**Figure 33:** Scheme of the experiment to determine the muon stopping profile on a copper on quartz sample. Once the epithermal muons are decelerated to the required energy they stop in the composite sample (top figure). Muons in copper remain in a diamagnetic state, whereas those in quartz form muonium atoms  $\text{Mu}$ , the energetic levels as a function of field being respectively shown in the middle figure. The two asymmetry signals are easily distinguished by the very different precession frequency (bottom figure).

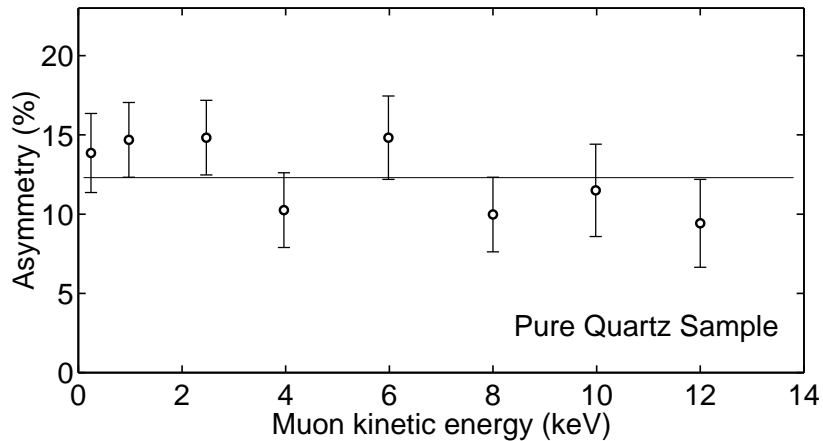


**Figure 34:** Calibration measurement with a pure quartz sample to exclude possible decelerator effects on measured asymmetry. The experimental data, taken at the same energies as in the copper on quartz experiment, seem to be randomly scattered around a 12.4(7)% fitted mean value of asymmetry (straight full line).

The sample station used for these experiments was an upgraded version of the one employed during the preliminary characterisations and consisted in 8 detector pairs symmetrically arranged with respect to the sample position (see section 3.2.2.4). The decelerator in front of the sample uses two 95% transmittivity copper meshes mounted 16 cm apart to define the equipotential planes. With the upstream mesh put at ground and the downstream one set at either positive or negative voltages, one can span a rather wide energy range going from about twice the transport voltage ( $E_k = 2eV_{\text{acc}} = 16 \text{ keV}$ ) down to intrinsic energy spread at the production site (typically  $\sim 10 \text{ eV}$ ). To improve the electrostatic field homogeneity and to ensure a good electrical contact, the sample was directly attached to the high voltage downstream mesh. Furthermore, to limit the increased background from muons stopping in the decelerator frame, a Kapton<sup>®</sup> foil annular collimator of 70 mm inner diameter was mounted 27 cm before the sample position.

Prior to performing measurements with epithermal muons, the quartz substrate was tested in a *surface* muon beam and a muonium fraction asymmetry of approximately 90(2)% was found. During all the LE- $\mu$ SR experiments the solenoid provided a magnetic field of 42 G with only 2% of field inhomogeneity, parallel to the sample surface but perpendicular to muon spin. As explained in detail in section 4.1, the present epithermal muon beam exhibits a rather large spot size of 57(12) mm FWHM. This, associated to the increased beam divergence [148] and to the difficulties of slow muon focusing, highly suggests the use of preliminary measurements on a “dummy” sample. These calibration measurements, which serve both to establish the base level of the diamagnetic asymmetry  $A_\mu$  and to exclude any possible influence due to the electrostatic decelerator, were carried out using a very pure quartz sample, identical in every respect to that of the real experiment except for the absence of the copper layer. The

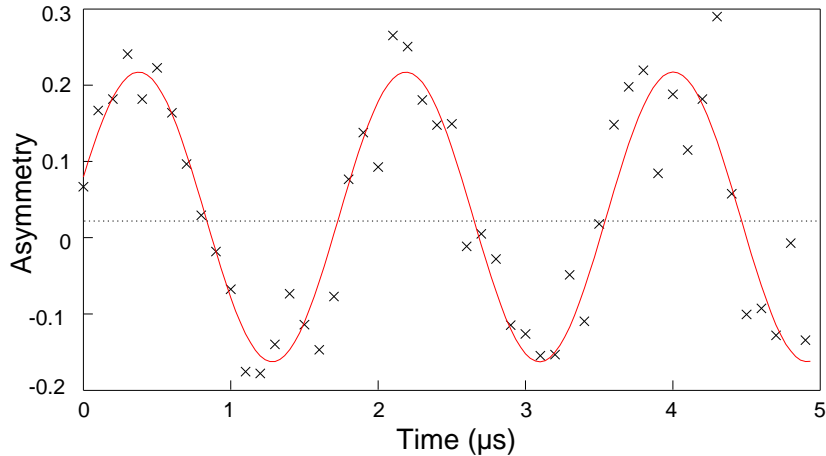


**Figure 35:** Asymmetry spectrum for 1 keV muons precessing in the 20 nm copper film at a 4.2 mT applied magnetic field. The full line shows the best fit curve which provides among others the amplitude of oscillation (maximum asymmetry).

asymmetry values measured at various implantation energies are shown in figure 34. The random distribution of the data points around a fitted mean value of 12.4(7)% makes us conclude that the presence of the decelerator does not affect the depth slicing measurements. The extracted mean asymmetry was then used in subsequent normalisations.

Next, several measurements were performed at different implantation energies on the copper on quartz sample. Figure 35 shows a typical asymmetry spectrum obtained in case of 1 keV muons. The data can be readily fitted with a simple decaying harmonic function from which three parameters are obtained. Apart from the precession frequency reflecting the externally applied field and the low relaxation rate characteristic of copper, the most important information is given by the asymmetry value. Indeed, whereas the first two quantities remain practically constant over all the measurement range, the asymmetry changes as the muon kinetic energy is varied.

For higher kinetic energies muons are implanted deep inside the quartz with a consequent decrease in the asymmetry signal amplitude; conversely, low energy muons will stop almost entirely in the copper layer giving a maximum precession amplitude. The measurements carried out at various muon energies are summarised in figure 36. From the figure one notes that for energies above  $\sim 8$  keV the asymmetry levels off to approximately 12.5%, which corresponds just to the value found for pure quartz (see figure 34), indicating that most of the muons have enough energy to pass the copper layer and stop in the quartz substrate. On the other hand, a reduction in implantation energy results in an asymmetry increase up to a maximum of 20.5%. In absence of any oxide layer we would expect a monotonically growing asymmetry, reaching its maximum at the lowest implantation energy, as shown with a continuous thin line in figure 36. The decrease of measured asymmetry at very low energies ( $< 500$  eV) indicates instead the existence of an oxide layer. Indeed, the behaviour of the

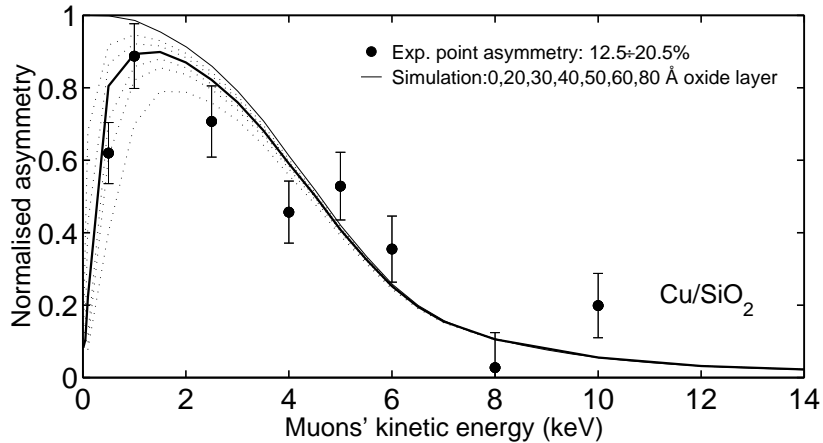


**Figure 36:** Slicing experiment on 20 nm copper over a quartz substrate performed by measuring the muon asymmetry in copper as a function of incoming muon energy. The drop in asymmetry at low energy is proportional to the fraction of muons stopped in the surface oxide layer, as calculated by Monte Carlo simulations (solid curve) by assuming an oxide layer thickness of 3 - 4 nm. Independent Auger profiles on the same sample measure a total non-metallic surface layer of about 2-3 nm (see text). Background measurements were taken on a quartz substrate alone.

muons stopped within the oxide will be similar to that in most other insulators, i.e. they will form muonium atoms and hence a reduction in  $A_\mu$  is foreseen. Considering the rather small oxide layer thickness, the observation of the initial drop in asymmetry demonstrates a good energy resolution for the pulsed muon beam.

Many computer codes relying on Monte Carlo techniques are available for predicting the stopping profiles of charged particles. Our simulation were based on the program SRIM 2000 [160,158], which has proven quite reliable at intermediate energies (see chapter 7). After providing the main parameters of the experiment as an input, including the muon mass, the multi-layered sample composition, the material densities and thicknesses, the program gives the muon range distribution as an output. The various simulations performed at different energies are summarised in figure 37, where one notes that range distributions are characterised by rather broad maxima and by tails extending at lower depths. To compare the simulations with the experiment we fix the thickness of the copper layer at 20 nm and in meantime assume a variable oxide layer. For each value of the oxide depth the normalised asymmetry  $A_\mu$  was calculated from the number of muons stopped within the copper layer. The family of curves thus obtained is shown in figure 36. As the thickness of the oxide increases the curves bend downwards following the data points fairly well. Even though a true fit to experimental data is not possible, from the family of simulation curves one can reasonably expect a 3–4 nm oxide layer thickness (bold curve in figure 36), fully confirmed by the independent Auger analysis of the sample surface, which indicate the presence of 2–3 nm of  $\text{Cu}_2\text{O}$ .

Similar range studies recently performed also at PSI [50], could in addition evidence the

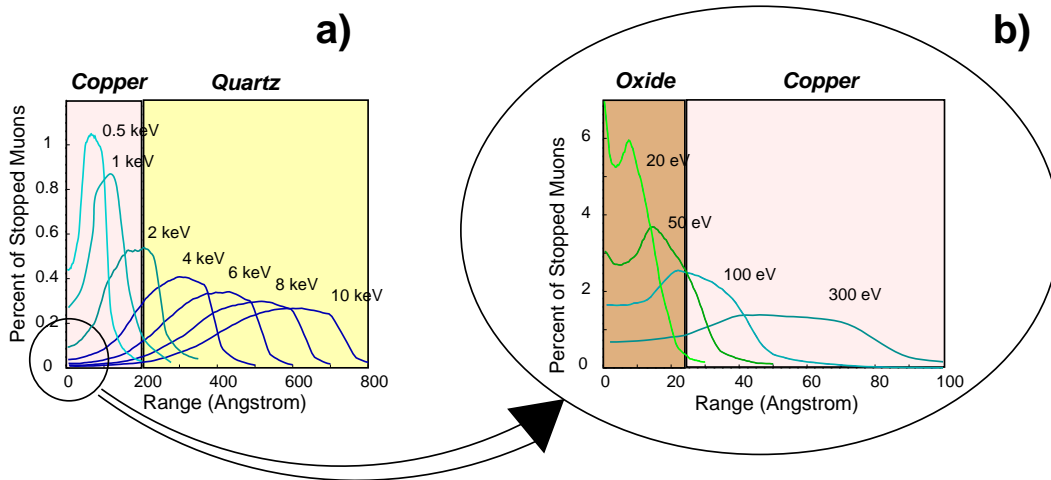


**Figure 37:** Simulated muon implantation profiles in a copper on quartz sample as a function of energy (a). As the energy decreases the broad maximum moves towards the copper surface and the curves become more peaked. For very low energies, the enlarged figure (b) shows that most of the muons will stop in the initial copper oxide layer.

presence of muon backscattering at low energies ( $\sim 3$  keV). The experimental data were found in good agreement with simulations carried out using the TRIM.SP program [85], an improved version of SRIM (even though our simulations with SRIM provided reliable predictions as well). In these experiments due to the unavoidable presence of a trigger detector in a continuous muon beam, the intrinsic energy resolution was limited to about half of a keV. However, the beam resolution is supposed to improve with the use of a cylindrical electrode positioned behind the detection trigger [95].

In conclusion, we have shown that the implantation range of low-energy muons can be successfully determined with the use of a metal–insulator system by measuring the diamagnetic asymmetry as a function of the incident energy and the measured profile agrees well with the simulated values. More importantly, the experiment confirms that by employing an electrostatic decelerator it is possible to produce a tunable slow muon source, whose energy still retains the original narrow distribution, characteristic of a pulsed beam. The ensuing narrow stopping profile permits investigations on thin films and interfaces in the range of a few tens of ångströms.

## 5.2 Investigations on magnetic thin films

Another opportunity to test the ability of epithermal muons as a new investigative tool was provided by the study of magnetic thin films. Thus, a demonstrative experiment on an *interface* between copper and *hexagonal cobalt* films, was performed to explore the potentialities of the slow muon beam when studying the magnetic properties of thin films and interfaces

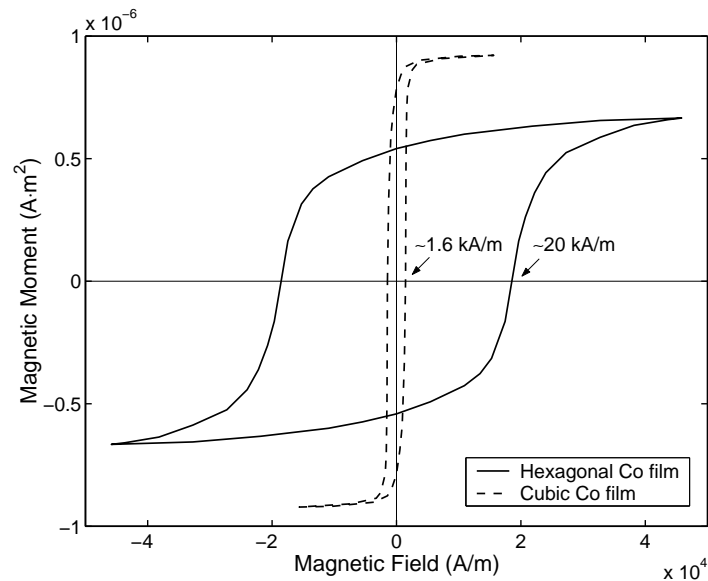


**Figure 38:** Magnetisation curves for two cobalt films with different crystalline structures. The hexagonal cobalt film (full line) is characterised by a very broad hysteresis loop and a relatively large coercive field ( $\sim 20$  kA/m). The cubic cobalt instead (dashed line) displays a much narrower hysteresis cycle and a correspondingly lower coercive field ( $\sim 1.6$  kA/m).

between magnetic and non-magnetic materials. In principle, in this case there is no need for an externally applied field, since the precession will occur in the material's intrinsic magnetic field.

The sample consists of a 40 mm diameter silicon substrate on top of which a 80 nm hexagonal cobalt film is deposited first, followed by a 20 nm copper film. Copper and cobalt are ideal materials for such studies as they have a negligible atomic miscibility and thus offer atomically clean interfaces. This sample, like the previous one, was grown by sputtering at the MASPEC institute<sup>2</sup>. Growing conditions for the cobalt film were chosen in order to induce a hexagonal structure, since from single hexagonal crystal studies it is known [104] that the muon precession frequency in the local magnetic field should fall within the frequency cut-off of the ISIS beam time-structure. More precisely, in case of a cobalt single crystal measured at room temperature we do expect a muon precession frequency of  $\sim 2.75$  MHz with an asymmetry of roughly  $\sim 20\%$ . The morphology of the cobalt film was characterised both by X-ray diffraction and by magnetisation curves. The hexagonal c-axis was found to lay in the film plane and the crystallites had a linear size of about 30 nm. Comparative characterisations, performed on films grown in such conditions as to induce a cubic structure, confirmed their quite low coercive field (only  $\sim 1.6$  kA/m) and the cubic crystalline structure. The magnetisation curves obtained in the two cases are shown in figure 38. The hexagonal cobalt film is clearly distinguishable from the cubic cobalt because, apart from a very broad

<sup>2</sup>Istituto Materiali Speciali per l'Elettronica e Magnetismo, Parma, Italy.

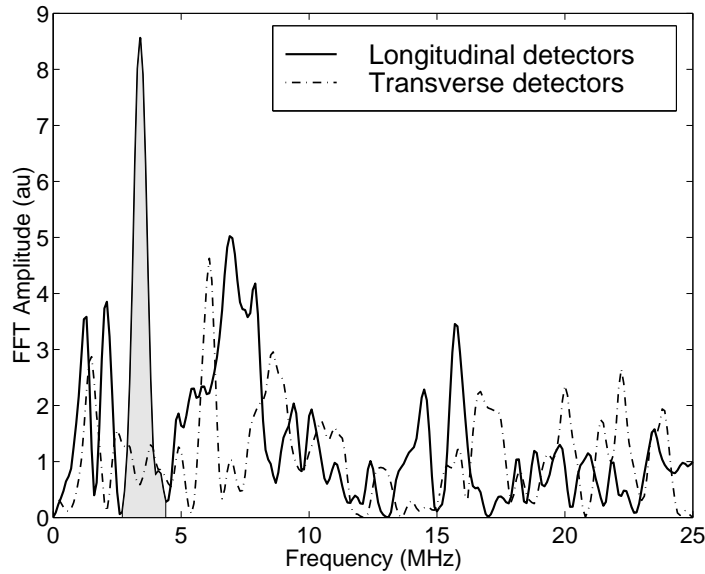


**Figure 39:** Fourier spectra of the histograms obtained by stopping muons in a hexagonal cobalt film. In zero external field the precession signal is expected in the longitudinal detectors and no signal in the transverse ones (see text). The highlighted peak occurs at a frequency which is close to the single crystal results.

hysteresis cycle, it displays also a much larger coercive field of  $\sim 20$  kA/m.

Because of the cluster morphology of the film, the evaluated asymmetry was expected to be much less than 10%. Other effects, such as the role of the excluded volume and the possible preferential diffusion of muons towards grain boundaries could not be evaluated quantitatively, but a further reduction in asymmetry was expected. On the other hand, accurate simulations showed that, in the hypothesis of a signal with an asymmetry of 5% and damping constant of  $\sim 1 \mu\text{s}$ , the precession frequency can be detected both by a time domain fit and also by a Fourier transform, provided that at least  $1.5 \cdot 10^5$  events are collected.

The spectrometer setup was the same as the one used during the measurement of slow muon implantation profile. However, since the cobalt *c*-axis lays in the film plane, only four scintillator telescopes in the forward–backward configuration with respect to the muon initial polarisation will detect the precession signal; the other four belong to the transverse configuration and hence will not detect any precession (see figure 20). The muon energy was tuned to 8 keV in order for the muons to cross the 20 nm copper film sputtered over the cobalt film. Unfortunately, due to problems with the primary proton accelerator, we could not collect an adequate statistics during the allocated beam time. Nonetheless, it was sufficient to perform a Fourier analysis, whose spectra for both the longitudinal and transverse configurations are shown in figure 39.

From this figure it can be seen that the highlighted FFT peak in the signal from longitudinal detectors indicates the presence of a muon precession frequency in the expected range.

The rest of the spectrum consists mainly of statistical noise as is evinced from the random location of the peaks, their relatively lower height and the lack of any correlation in the spectra of the two detector sets. The value of the measured frequency is consistent, although slightly different, with the single crystal results and corresponds to the local magnetic fields at the site(s) where muons come at rest in the film. In view of the film morphology and of the muon diffusion and localisation properties (all features that still need to be investigated) the present indications are encouraging.

In conclusion, we believe that the precession signal in the hexagonal cobalt hyperfine field has been detected and, compatibly with the limits set by the low statistics, we can tell that the hyperfine fields are at least 25% higher than those expected from single crystal data. Only further experiments will provide information on the spread and relative strength of the local magnetic fields in the small cobalt clusters within the film. In particular it will be possible to investigate the existence of “finite size” effects, which depress the fundamental parameters of the magnetic system in its thermodynamical limit: Curie temperature,  $T_c$ , and spontaneous magnetisation,  $M_s$ .

We close here the first part of the present thesis, mostly dedicated to the systematic exposition of the principles of epithermal muon generation, the setup and properties of the pulsed slow muon beam and to the experimental results obtained in thin films.

During the progress of the present work, the pulsed nature of the ISIS beam proved to be essential for producing a slow muon source that has a unique energy resolution, necessary for investigating important fields of research such as nanostructures, surfaces and ultra-thin films.

In addition, a pulsed beam allows the synchronous application of different fields: magnetic, electric, electromagnetic, etc. [135, 31] and hence offers the possibility of using  $\mu$ SR for studying non-linear and off-equilibrium phenomena in a variety of low dimensionality systems. The second part of this thesis is entirely devoted to the practical implementation of the synchronously applied fields, focusing mainly on two of its uses: the projected range imaging and the study of adiabatic to non-adiabatic crossover. We remind the reader that the developments mentioned in the second part, although foreseen for use in a slow muon beam, were carried out in a traditional surface muon beam.

## Part II

# Developments dedicated to low energy $\mu$ SR

## Chapter 6

# Projected Range Imaging (PRI)

IN this chapter we describe a new  $\mu$ SR method, devised for directly imaging the implantation depth distribution of positive *epithermal* muons in metals, called Projected Range Imaging (PRI). After discussing the main features and the advantages of the method, the experimental results for muons with energies in the MeV range are tested against Monte Carlo simulations and compared with measurements obtained by using the conventional *moderator curve* method.

Range and straggling studies are then shown to be possible also with epithermal muons. These future extensions will allow a better understanding of the energy loss mechanisms in the previously inaccessible very low energy range.

### 6.1 Introduction

Individual muons implanted in a sample during a  $\mu$ SR experiment stop at different depths from the surface exposed to the muon beam. The material dependent *projected range*  $R$  coincides with the average depth, while the width of the distribution  $\Delta R$  is referred to as *straggling* [103]. Most muon beams consist of particles of the same moderate incident energy [16, 112] ( $\sim 4$  MeV) so that simple rule-of-thumb prescriptions on sample thickness would suffice. When needed, a *variable moderator* experiment allows a reliable check: it consists of recording the signal amplitude of muons stopping in a suitably thin sample as the thickness of a moderator material placed immediately upstream the sample is varied.

The main motivation for devising a new quantitative measurement of the entire range distribution at epithermal energies has basically a twofold origin:

- An experimental one, since the ordinary methods for mapping the muon implantation profile cannot be applied to epithermal muons, primarily because of the very large energy straggling introduced during the mapping measurement.

- A theoretical one, whose aim is to test the reliability of Monte Carlo simulations at epithermal energies. Indeed, as mentioned in section 5.1, for a light particle such as a positive muon ( $m_\mu \approx 1/9 \cdot m_p$ ) the lack of experimental data at very low energies is accompanied by the uncertainty regarding the reliability of the simulation codes so far developed and tested for ions.

The first aspect was closely related to the development of the tunable energy epithermal muon beam at ISIS, for which a calibration of the muon stopping depth with the conventional moderator curves is both impractical and time consuming.

As for the other point, scattering of charged particles in condensed matter, while well understood down to kinetic energies of few hundreds eV, is still largely unexplored when the energy approaches the scale of the electronic outer bands in solids (see also section 4.6.1). Detailed studies of this regime, where a variety of solid state excitations might play a role, are of relevance also for light ion implantation. Attention for this largely unexplored field [44] is testified by recent simulations [85] and experimental work [122] on hydrogen and deuterium.

The proposed method is applicable to electric conductors and it directly yields the distribution of the projected range of individual particles, as if it were imaged, whence the name “Projected Range Imaging” (PRI). The method of PRI relies upon two main circumstances:

- One is the direct detection by means of  $\mu$ SR itself, here taken to mean the specific Muon Spin *Rotation* variety of this spectroscopy [125].
- The second circumstance is the generation of a large magnetic field gradient in the direction of the incoming muons by a laminar electric current.

The Larmor spin precession frequency of the implanted muons is proportional to the local magnetic field, which varies linearly throughout the thickness of the metallic slab, because of the uniform electric current flowing along it. This establishes a *direct correspondence* between the distribution of stopping muon depths and the distribution of Larmor frequencies, as determined by the Fourier transform of the precession signal in a single  $\mu$ SR experiment.

Both the geometry of the current and the fact that sample and magnetic field gradient source are but the same object (we shall refer to this as a *self generated* gradient) are essential points of the technique, which however limit its application to highly conducting materials. Conventional magnetic field gradients generated outside the sample are far too weak for our purpose. Besides, they would extend over a large volume, thus interfering severely with the beam transport.

The present PRI method is reminiscent of the well known *Magnetic Resonance Imaging* [78] (MRI), based upon the resonance of nuclear spin species. In MRI the space–frequency link is provided by conventional magnetic field gradients over large objects allowing two-dimensional (2D) resolution. PRI is a simpler 1D version of the same principle.

The  $\mu$ SR experiments were conducted on the MuSR apparatus at the ISIS Muon Facility shown in figure 11. For the actual beam energy of approximately 3 MeV (because of energy loss in vacuum windows of the transport channel), in metals we expect a range between 100 and 500  $\mu\text{m}$ . Hence, the present demonstrative experiments were performed on thin metallic sheets.

As shown in figure 10, the ISIS beam exhibits a pulsed time structure with intense, 80 ns wide, bunches of muons produced every 20 ms. It is just the pulsed nature of the muon source to allow synchronous pulsing of the currents with a low duty-cycle and hence achieve very large magnetic field gradients. Consequently, as we will show later, appropriate gradients can be generated also in ultra thin films and PRI experiments can be performed when muons at very low energy will become available on a routine basis. We conclude this introductory section by providing some definitions that will be used in the rest of the chapter.

### Some definitions and formulae

When a charged particle as the muon enters a given material, due to the various mechanisms of energy loss (see section 4.6.1), it will eventually thermalise at some distance from the entry point. In what follows we give a list of useful definitions when studying the implantation profile of charged particles [103], some of which are also illustrated in figure 40:

- The *linear range*  $R_L(E_0)$ , is the total path length measured along the particle's path, between the point at which it has the energy  $E_0$  (in the laboratory system) and its stopping point.
- The *vector range*  $R_V(E_0)$ , is the actual vector distance between these two points.
- The *projected range*  $R_P(E_0)$ , is the projection of the vector range on the direction of the particle's motion when its energy was  $E_0$ ;  $R_P(E_0)$  is thus a measure of the penetration of a particle along its initial direction.
- The *energy straggling* describes the finite width energy distribution curve, which arises from the stochastic nature of the energy loss processes in a material.
- Finally, the corresponding spread in the range of the particles is named *range straggling*.

When performing theoretical calculations regarding the energy loss it is more convenient to work in terms of *linear range*; on the other hand the experimental measurements yield the *projected range*. There exists a simple semi-empirical formula that relates these two quantities [80, 103]:

$$\frac{R_L}{R_P} \approx 1 + \frac{1}{3} \mu$$

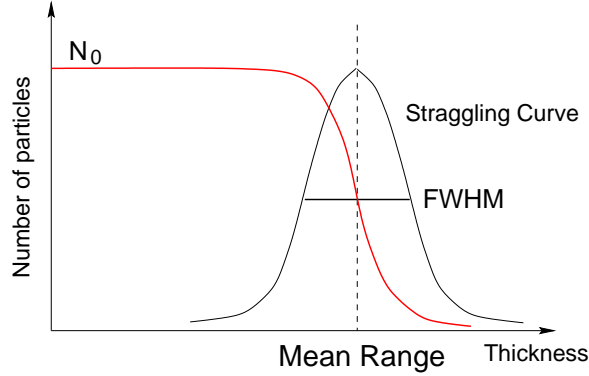


**Figure 40:** Definitions of *projected range* and *range straggling* for charged particles stopped in matter. Both the variation of particle number with the material thickness as well as the respective straggling curve are shown.

with  $\mu = M_2/M_1$ , where  $M_1$  and  $M_2$  are respectively the masses of the incident particle and that of the knocked atom.

Straggling generally depends both on the intrinsic spread, characteristic of the given material, and also on the momentum “bite” of the particle beam, introduced by the transport and focusing even in case of an originally monochromatic beam.

A precise calculation of the intrinsic straggling is very difficult, even though the approximate formula  $\Delta R_{\text{intr}} \simeq 10\%R$ , has shown to give satisfactory results. As for the straggling connected to the momentum spread of the incident particles, we consider first a well known formula [151, 112, 79] which gives the range dependence on the particle’s linear momentum:

$$R \simeq a \cdot p^{3.5} \quad (26)$$

with  $R$  the particle’s range,  $p$  its linear momentum and  $a$  a material dependent constant. From it, the straggling induced by the momentum spread, is immediately found to be:

$$\Delta R_{\text{mom}} \simeq 3.5 a p^{2.5} \Delta p = 3.5 \left( \frac{\Delta p}{p} \right) \cdot R \quad (27)$$

Since for a given muon beam the quantity  $\Delta p/p$  usually has a fixed value, one can write:

$$\Delta R_{\text{mom}} \propto R \propto p^{3.5} \quad (28)$$

Since the effects of the intrinsic straggling and that of the beam momentum spread are independent, they will contribute additively to the second moment of the total distribution. Hence for the *total* straggling one finds:

$$\Delta R_{\text{tot}} \simeq [(0.1)^2 + (3.5\Delta p/p)^2]^{1/2} \cdot R \quad (29)$$

$$\Delta R_{\text{tot}} \simeq a \cdot [(0.1)^2 + (3.5\Delta p/p)^2]^{1/2} \cdot p^{3.5} \quad (30)$$

The last equations show that a reduction in  $\Delta p/p$  implies a reduction also in  $\Delta R_{\text{tot}}$ , whose drop however cannot go beyond the limit set by the intrinsic straggling. As we will see

further, (cfr. section 6.3), the experimental results on an aluminium foil fully confirm these formulas.

## 6.2 Principles of the PRI method

To understand how  $\mu$ SR allows range and straggling measurements in conducting films, let us first examine the simple case of a metal sample placed in a uniform magnetic field  $B_0$ . From section 2.4 we recall that after the very fast thermalisation process, in a *transverse field*  $\mu$ SR experiment the evolution of muon spins is described by the formula:

$$N(t) = N_0 \exp(-t/\tau_\mu) [1 + AG(t) \cos(2\pi\nu_\mu t + \phi)], \quad (31)$$

where the standard notation is used for the various symbols. Next, either a direct fit or a combination of two detectors lying opposite in the precession plane will yield the muon polarisation function  $P_\mu(t) = G(t) \cos(2\pi\nu_\mu t + \phi)$ .

In a *uniform* magnetic field all the muons precess at the *same* frequency  $\nu_\mu$ , i.e.  $G(t) = 1$ , the experimental asymmetry  $A$  is maximum and the Fourier Transform (FT) of  $P_\mu(t)$  exhibits a narrow peak at the frequency  $\nu_\mu$ . If a *spatially varying* magnetic field  $\mathbf{B} = \mathbf{B}(z)$  is applied instead, an unknown distribution  $D(z)$  of muon projected ranges  $z$  is measurable by the corresponding *distribution* of Larmor frequencies. In the FT of the muon polarisation data this frequency distribution is immediately available and its conversion into the projected range distribution  $D(z)$  will only require the knowledge of  $\mathbf{B} = \mathbf{B}(z)$ .

To show this in more detail, let us specify a geometry in which the incident muons have an initial spin polarisation along the direction of the incident particle trajectory,  $\hat{\mathbf{z}}$ . A constant magnetic field gradient  $b$  serves our purposes and the resulting local field  $\mathbf{B}(z)$  must be perpendicular to the initial muon spin polarisation, such as  $\mathbf{B}(z) = B(z)\hat{\mathbf{x}} = (B_0 + bz)\hat{\mathbf{x}}$ .

If  $D(z)$  is the normalised distribution of muons as a function of depth  $z$  the complex muon polarisation in the presence of the constant gradient specified above is

$$P(t) = \int dz D(z) G(t) e^{i(\omega_0 + \varpi z)t},$$

with  $\omega_0 = 2\pi\gamma_\mu B_0$  and  $\varpi = 2\pi\gamma_\mu b$ . Introducing  $\mathcal{D}(k)$ , the Fourier transform of  $D(z)$ , the previous formula may be rewritten as:

$$P(t) = \mathcal{D}\left(t\frac{\varpi}{2\pi}\right) G(t) e^{i\omega_0 t},$$

From this, with a simple rearrangement of the terms and by antitransforming both sides we finally get:

$$D(z) = \frac{\varpi}{2\pi} \int dt \frac{P(t) \cdot e^{-i\omega_0 t}}{G(t)} e^{i\varpi z t} \quad (32)$$

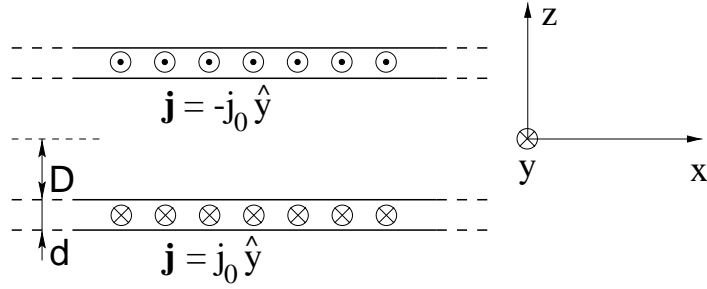


**Figure 41:** Geometry of currents.

In the simple case when  $G(t) = 1$ , one gets:

$$D(z) = \mathcal{P}\left(\frac{\omega - \omega_0}{\varpi}\right). \quad (33)$$

### 6.2.1 Magnetic field gradients in metallic films

Before performing the experiments we must quantify the value of field gradient required for measuring range  $R$  and straggling  $\Delta R$ . A lower limit is set by the intrinsic  $\mu$ SR linewidth in metals, i.e. the width of the Fourier transform of the relaxation function  $G(t)$  [58, 152]. A typical resolution limit for this quantity on MuSR is  $\sigma_0 \simeq 0.004 \mu\text{s}^{-1}$ , which corresponds to a spread in local magnetic field intensity at the muon site of the order of  $\langle \delta B^2 \rangle^{1/2} \simeq 5 \cdot 10^{-6} \text{ T}$ .

One must produce field gradients such that the magnetic field variation ( $\Delta B_{tot}$ ) over the straggling  $\Delta R$ , is larger than  $\langle \delta B^2 \rangle^{1/2} \simeq 5 \cdot 10^{-6} \text{ T}$ , i.e.:

$$\frac{\partial B_{\text{ext}}}{\partial z} \gg \frac{\langle \delta B^2 \rangle^{1/2}}{\Delta R} \quad (34)$$

Let us estimate this limit for aluminium and copper in the most unfavourable condition, i.e. that of a minimum straggling, obtained for an ideally monochromatic beam. In this case only the intrinsic straggling will be present and hence, from formula (29), we expect a muon straggling of the order of  $0.1R$ . Taking into account that for the actual muon energy at experimental site of 3.05 MeV the ranges are approximately  $400 \mu\text{m}$  for Al and  $150 \mu\text{m}$  for Cu, one obtains  $\Delta R \approx 0.1R = 40 \mu\text{m}$  and  $20 \mu\text{m}$ ; the minimum field gradient is then  $0.125 \text{ T/m}$  and  $0.25 \text{ T/m}$  respectively. One can safely carry out PRI experiments with field gradients of the order of a few T/m. Obviously, the lower the particle energy, the smaller  $R$  and  $\Delta R$  and, consequently, larger field gradients are needed. We shall come back to this point in the final comments regarding epithermal muons.

Large field gradients inside a metallic slab can be achieved by driving an intense electric current along it. Figure 41 shows the selected current geometry, composed of two parallel slabs in which a uniform current with density  $j_0$  flows in opposite directions (see also figure 48 for a pictorial view). For slab dimensions  $40 \times 40 \times 0.1 \text{ mm}^3$  (for the ISIS MuSR beam 90%

of the transported muons fall within a diameter of 30 mm) we may neglect fringe effects and compute the magnetic field by Ampère's law. Using the notation of the figure, one gets:

$$\mathbf{B}_I(z) = \hat{\mathbf{x}} \begin{cases} \mu_0 j_0 d & |z| \leq D \\ \frac{1}{2} \mu_0 j_0 [(D + d) - |z|] & D < |z| < D + d \\ 0 & |z| \geq D + d \end{cases} \quad (35)$$

Note that the field  $\mathbf{B}$  is parallel to the surface of the slab and perpendicular to  $\mathbf{j}$ . For the loop, whose cross section is shown in figure 42, the magnetic field magnitude is zero outside the loop, varies linearly inside the slabs and has its maximum value in the space between them, as shown schematically with bold lines in figure 42.a.

The device is placed in an external, uniform magnetic field  $B_0 \hat{\mathbf{x}}$ , which conveniently shifts the frequency scale by  $\nu_0 = \gamma_\mu B_0$ . When all muons stop in the slab  $\mathcal{S}_1$ , a  $\mu$ SR experiment measures a distribution of Larmor frequencies  $\nu$  which, according to equation (33), are related by:

$$z = \frac{\nu - \nu_0}{\gamma_\mu b} \quad (36)$$

to the stopping depth  $z$ .

The fine tuning of the muon stopping depth is achieved by means of an upstream moderator  $M$ , so that the projected range falls in the center of the slab  $\mathcal{S}_1$ .

The corresponding fraction of stopped muons as a function of depth  $z$  is shown in figure 42.b. The thickness of the slab  $\mathcal{S}_1$  is chosen close to the straggling  $\Delta R$ , which is obviously the optimal imaging condition.

Even when the thickness of the slab  $\mathcal{S}_1$  is larger than  $\Delta R$ , since the straggling is given by a distribution, some of the muons belonging to the lower energy tail will stop in the moderator  $M$  in front of  $\mathcal{S}_1$  — experiencing a field  $B_0$  — whereas those of the higher energy tail stop on the surface of the backward current slab  $\mathcal{S}_2$  — experiencing a field  $B_1 \approx B_0 + \mu_0 j_0 d$ . The expected Fourier transform of the  $\mu$ SR polarisation is qualitatively sketched in figure 42.c. Here the narrow peaks A and C at frequencies  $\nu_0$  and  $\nu_1$  correspond respectively to muons stopped in the moderator  $M$  and in the slab  $\mathcal{S}_2$ , where they experience field magnitudes  $B_0$  and  $B_1$ . Note that, since the return slab  $\mathcal{S}_2$  is thicker than  $\mathcal{S}_1$ , the field gradient inside it is much smaller, which implies a rather narrow C peak. Finally, the broad peak B images the central portion of the muon stopping distribution, as discussed at the beginning of the present section.

### 6.3 Experimental Results

The present section is divided into two parts: the first one describes a series of control experiments performed according to the conventional variable moderator technique and shows

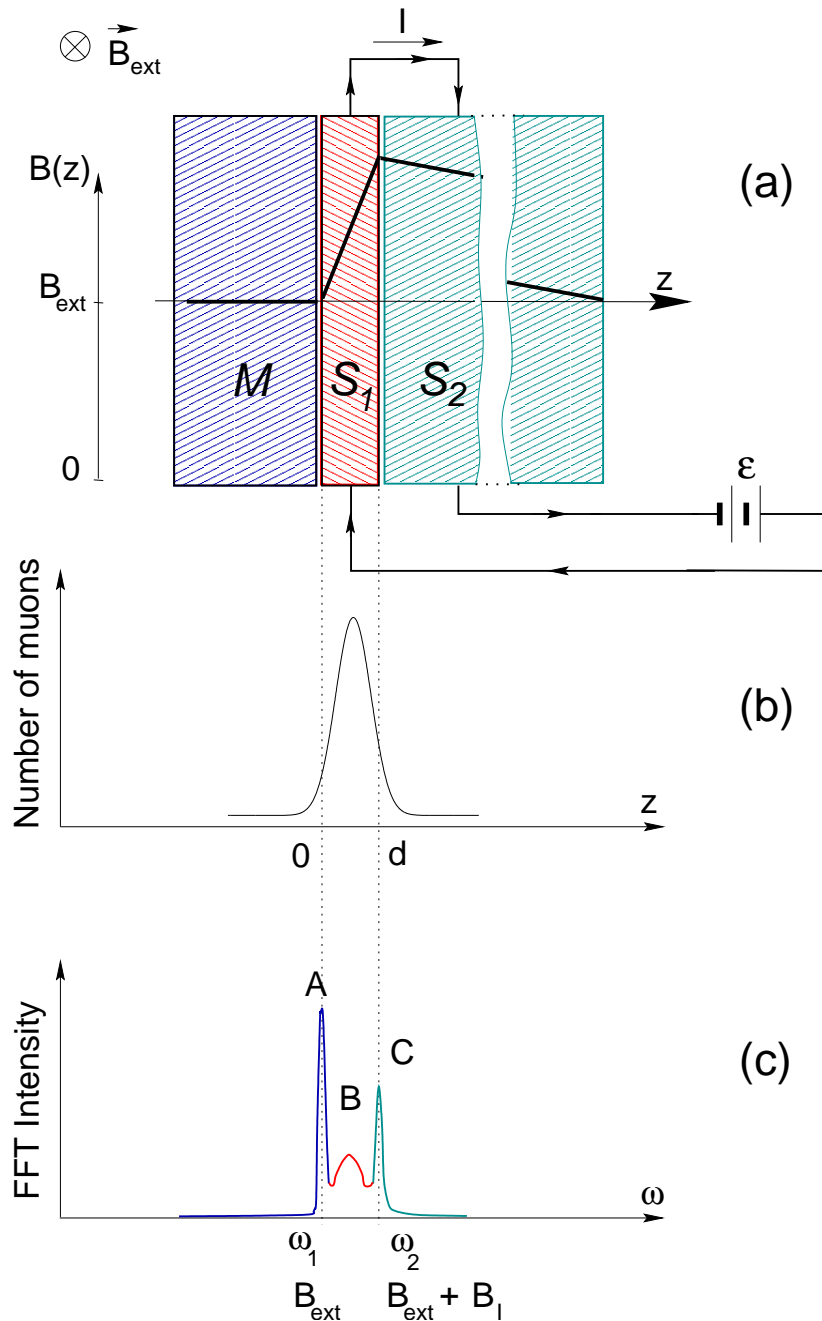


**Figure 42:** (a) Sketch of the PRI device, which comprises a moderator  $M$  and a current loop made of two slabs,  $S_1$  and  $S_2$ . The solid line in the superimposed plot represents the magnetic field profile in the device. (b) Plot of the function  $D(z)$ , mapping the stopped muon profile. (c) Fourier transform of the muon polarisation: the narrow A and C peaks correspond to muon stopping in  $M$  and in  $S_2$ , respectively, while the broad B peak maps muons at rest inside  $S_1$ .

the effect of the finite momentum spread of the muon beam. The second part summarises the PRI experimental results and the planned evolution of the technique towards its use with epithermal muons.

### 6.3.1 Range measurements by conventional methods

The sample consists of a thin Al layer in front of a quartz plate, as it is sketched in figure 43.a. A transverse external magnetic field of 30 mT is applied such that muons in Al precess

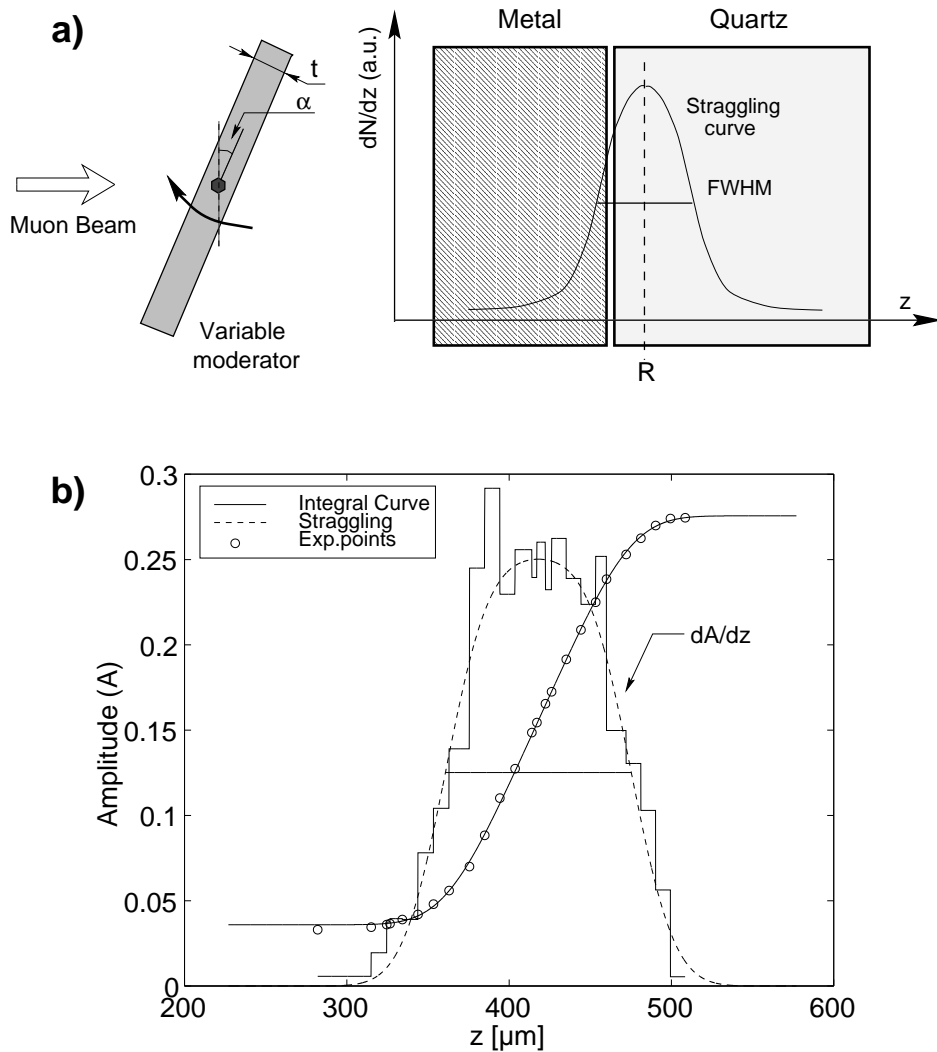


**Figure 43:** (a) Experimental layout for variable moderator experiments: the muon depth distribution (straggling curve) is overlaid on a sketch of the composite sample. Fine tuning of the moderator effective thickness is achieved by rotating the premoderator Al foil by the angle  $\alpha$ . (b) Open circles: amplitude of the Larmor precession in 30 mT as a function of Al thickness  $z$  - with best fit (see text) as a solid curve. The histogram is the numerical derivative of the amplitude curve (solid line: Gaussian best fit).

at  $\nu_L = 4.06$  MHz. In the quartz slab more than 90% of the muons form muonium atoms, for

which all precession frequencies [153] in the applied transverse magnetic field are too high to be observed at ISIS [41, 39, 43]. As a consequence, the  $\mu$ SR signal amplitude is proportional to the number of muons stopped in Al (cfr. section 5.1).

Coarse changes in the moderator thickness are obtained by adding  $50\ \mu\text{m}$  Al foils, while fine changes,  $z(\alpha) - z_0 = t/\cos\alpha$  result from varying the inclination of a premoderator  $t = 50\ \mu\text{m}$  Al foil.

A typical result obtained for aluminium with the *variable moderator* method is shown in figure 43.b. Each point corresponds to a  $\mu$ SR experiment performed with a different total moderator thickness  $z$  and the amplitude  $A(z)$  of the  $\mu$ SR signal provides the fraction of muons stopped in Al backed by a quartz slab. The data should follow the curve:

$$A(z) = A_1 + A_2 \int_0^z D(z') dz', \quad (37)$$

hence the muon distribution is given by  $D(z) = A_2^{-1} dA/dz$ . Assuming a Gaussian profile for  $D(z)$  we may use the function  $A(z) = A_1 + A_2 \text{erfc}(z)$  for fitting purposes.

The residual amplitude  $A_1$  observed for vanishing Al thickness is due partly to the residual small fraction of diamagnetic muons in quartz, partly to a few muons stopping in the metal frame around the composite sample. When the overall aluminium thickness is larger than the total range, all the stopped muons will precess inside Al and therefore give a signal amplitude  $A_1 + A_2 = 27\%$ , which corresponds to the maximum asymmetry value for the MuSR apparatus (since  $A_1 \ll A_2$  we can neglect its small  $z$  dependence).

However, we must also consider the spread in the momentum of the incoming muons (the so-called *momentum bite*), which, in standard conditions on MuSR, is  $\Delta p/p \sim 9\%$ . Its effect is to broaden the measured distribution  $D(z)$ , with the total straggling being given by formula (29):

$$\Delta R_{\text{tot}} \simeq [(0.1)^2 + (3.5\Delta p/p)^2]^{1/2} R \quad (38)$$

To obtain the material dependent contribution to the straggling we must first deconvolve the momentum contribution as discussed in the following section. The details of the deconvolution procedure in two relevant cases are extensively discussed in appendix B.

Similar experiments were performed also with a muon beam whose momentum spread was reduced to  $\Delta p/p \sim 3\%$ . For an easier comparison, the results corresponding to the two different spreads in beam momentum are both reported in figure 44. As expected, the intersection of the two data sets occurs at a thickness corresponding to the muon range in aluminium. From the figures 43 and 44 one can see also that the experimental data are in excellent agreement with the predictions of formula (29).

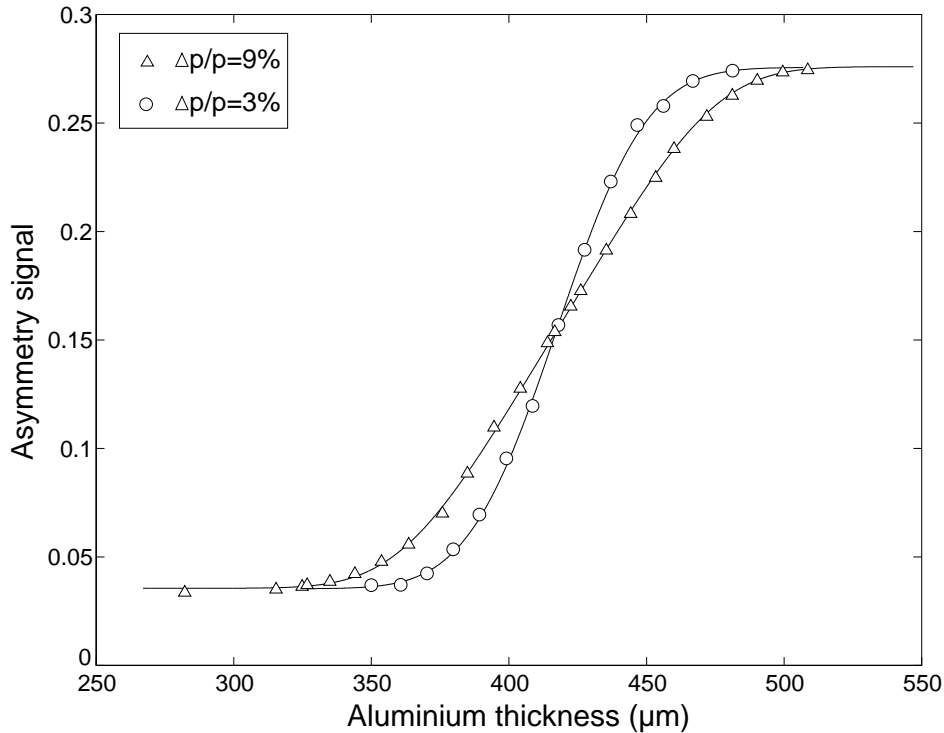


**Figure 44:** Asymmetry signals as a function of aluminium thickness for two different values of momentum spread of the muon beam. Note that the two fit curves intersect at a thickness corresponding to the muon range in Al ( $R \simeq 418 \mu\text{m}$ ). The asymptotic asymmetry values in both cases are the same, although the curve relative to  $\Delta p/p \sim 9\%$  shows a broader straggling distribution.

### 6.3.2 PRI results on Al, Cu and Pb

Most of the PRI measurements were performed with 100–150 A currents, and with a biasing external field of  $B_0 = 10 \text{ mT}$  perpendicular both to the current and to the muons' spin direction. The construction of the PRI device itself is rather simple. Since most of its operating parameters are not critical for performing PRI measurements, we defer to the next chapter a detailed description of the device. There are however some precautions that must be taken to ensure uniform current density in the slab and to avoid stray magnetic fields generated by the circuitry feeding the current into the slab. As far as the electrical contacts between the slab(s) and the current generator are concerned, mechanical contacts under pressure gave a better performance than soldered or welded ones. For thin films instead, we found reliable results with contacts attached using Silver Print<sup>®</sup>, successively pressed and dried under an inert atmosphere at 100° to 200°C.

Fourier transforms (FT) of muon polarisation for copper are shown in figure 45. By a variable moderator like that of figure 43 we could choose to stop the majority of muons either in the moderator itself, in the field  $B_0$  (panel a), or in the current slab  $S_1$ , inside the field gradient region (panel b), or behind it, in the field  $B_0 + \mu_0 j_0 d$  (panel c). The appearance

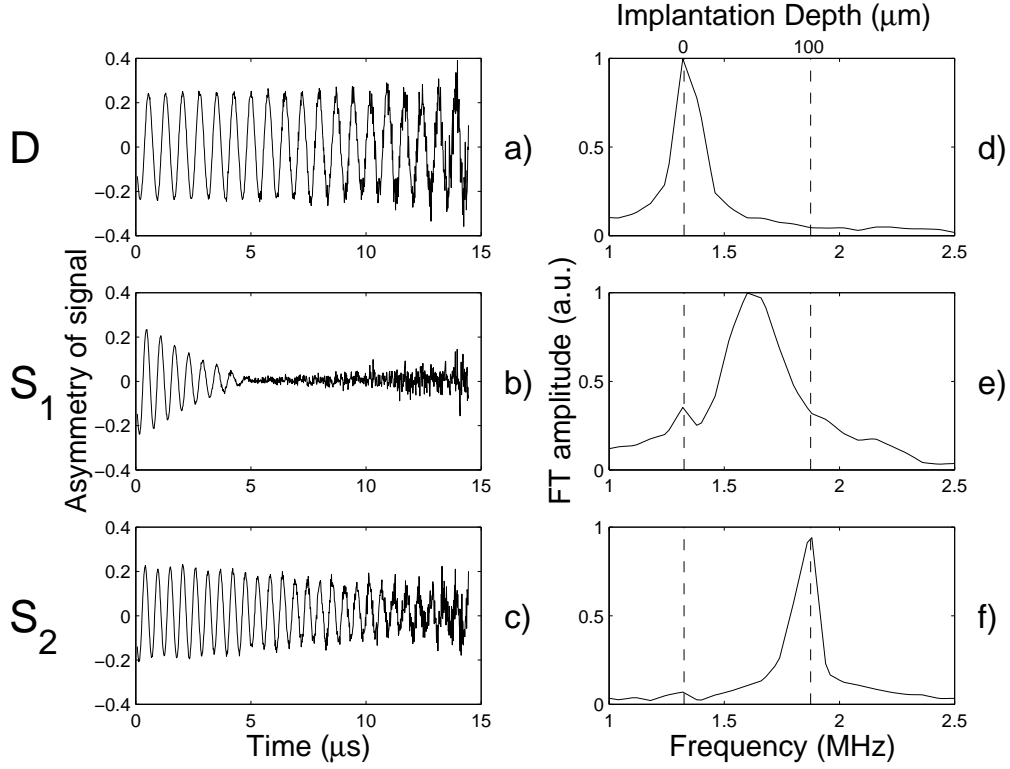


**Figure 45:** Polarisation (left) and its Fourier transform (right) for Cu with the PRI device (top scale: implantation depths  $z$  by equation (36)). Cu moderator was  $178.4 \text{ mg/cm}^2$  in (a),  $89.2 \text{ mg/cm}^2$  in (b) (dotted vertical lines delimit currents slab) and  $44.6 \text{ mg/cm}^2$  in (c).

of these FT plots agrees with expectations, anticipated in section 6.2. The narrow peaks of panels *a* and *c* correspond to muons experiencing vanishing or small magnetic field gradients (the return slab  $S_2$  is much thicker than  $S_1$ ). Actually FT analysis shows a resolution broadened width (an artifact due to the finite time window). A direct fit to equation (31) (by the MINUIT package [62]) with a Gaussian relaxation function  $G(t) = \exp[-(\sigma t)^2/2]$  yields a precise determination of the local field  $B_0 = 9.963(5) \text{ mT}$  and a much narrower width value,  $\sigma = 0.004(1) \mu\text{s}^{-1}$ , corresponding to a few hundredths of a Gauss for the inhomogeneity of  $B_0$ . The same analysis in the case of panel *c* yields  $B_1 = 13.627(6) \text{ mT}$  and a slightly larger  $\sigma = 0.050(1) \mu\text{s}$ , due to the small gradient in  $S_2$ .

The magnetic field drop across  $S_1$ , for slab thickness  $d$  and width  $l$ , is thus  $B_1 - B_0 = \mu_0 j_0 d = \mu_0 I/l = 3.6 \text{ mT}$ , by equation (35) which, for  $d = 10^{-4} \text{ m}$ , implies a gradient of  $36 \text{ T/m}$ . A calibration is shown in figure 46, where we collected data relative to Cu and Al slabs with the same widths  $l = 50 \text{ mm}$  and thickness in the range between  $50$  to  $100 \mu\text{m}$ . Muon magnetic field drops  $B_1 - B_0$  and current intensity  $I$  are proportional, with a slope  $b = (B_1 - B_0)/I = 0.248(2) \cdot 10^{-4} \text{ T/A}$ , which agrees very well with the value  $\mu_0/l = 0.251 \cdot 10^{-4} \text{ T/A}$  obtained in case of an infinite layer geometry.

The detailed PRI information is carried by the lineshape of the peak in panel *b*. The

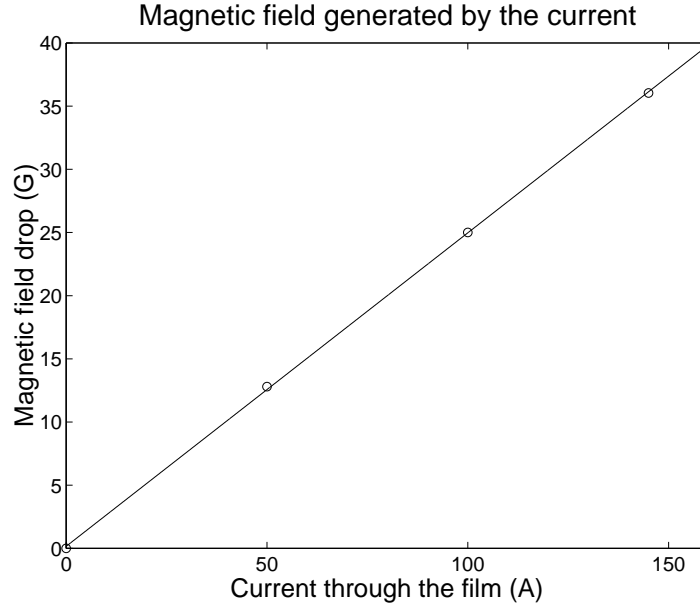


**Figure 46:** Magnetic field drop  $B = (\nu_1 - \nu_0)/\gamma_\mu$  as seen by muons stopping just before and just after the current slab  $\mathcal{S}_1$ , as a function of total current  $I$  in the slab.

frequency to depth scale conversion (top scale) afforded by equation (36) emphasizes the fact that the same lineshape, when normalised to unity, represents the function  $D(z)$ .

A direct time domain fit is equivalent to the FT analysis, provided a second component is included for the small residual peak at  $B_0$ . Following the discussion of section 6.3.1 a Gaussian lineshape is used. With this choice of fitting function it is also easy to deconvolve the momentum spread contribution from the width parameter  $\sigma$ , assuming a square wave shape for the momentum distribution — then  $G(t)$  is the product of a Gaussian and a sinc ( $\sin x/x$ ) function. This further assumption, supported by the good quality of the fit, was checked by running the same experiment with reduced momentum spread  $\Delta p/p = 3\%$ : results were within error bars. The fit in the case of figure 45.b (Cu) yields

$$\Delta R = \frac{\sigma_i}{2\pi\gamma_\mu b} = 14.3 \mu\text{m} \quad R = z_0 + \frac{B - B_0}{b} = 152.2(2) \mu\text{m}$$

where  $\sigma_i$  is the Gaussian parameter of the intrinsic straggling distribution,  $z_0 = 100 \mu\text{m}$  the moderator thickness and  $B = \nu/\gamma_\mu = 11.84(2) \text{ mT}$  is obtained from the fitted frequency  $\nu$ . Experiments with  $B_0 = 0$  may be analysed in a similar fashion and, apart from a trivial shift in frequency, they yield identical results.

The same experiments were run also on Al and Pb and the results are summarised in table 4. These results also agree within error bars with those of the conventional, but more time consuming, variable moderator method. The behaviour of the three listed materials follows the expected trend, which is a less than linear decrease of the range with increasing atomic

Material	$R$ meas. [ $\mu\text{m}$ ]	$R$ sim. [ $\mu\text{m}$ ]	$\Delta R$ meas. [ $\mu\text{m}$ ]	$\Delta R$ sim. [ $\mu\text{m}$ ]	$\Delta R/R$ meas. in %	$\Delta R/R$ sim. in %
Aluminium	418.4(6)	417	22.5(6)	22.1	5.4(1)	5.3
Copper	152.2(2)	150	14.3(4)	10.9	9.4(3)	7.27
Lead	161.1(3)	161	21.7(6)	20.3	13.5(4)	12.61

**Table 4:** Comparison between PRI-measured and simulated values for range and straggling of muons in some materials.

number  $Z$  (actually a slight increase for Pb), and a corresponding increase of the *relative* straggling.

For a precise determination of this qualitatively correct behaviour, the Monte Carlo simulation program SRIM [160] was used. The simulation at  $E_0 = 3.05$  MeV was based on 10 000 generated events. This program takes into account the energy loss due to ionisation in the first stages as well as those (more subtle) due to collective phenomena, (for instance phonon scattering) in the last stages of thermalisation. As can be seen from table 4 the simulated values are in fairly good agreement with the measurements.

### 6.3.3 Notes on thin films

Let us now discuss the possibility of applying the proposed method to epithermal muon beams. Scaling PRI down to keV muon energies and below implies driving currents comparable to those of the previous subsection (i.e. approximately 100 A) in thin or ultra thin films. Optimal field gradients imply a conducting layer thickness  $d$  comparable to the straggling  $\Delta R$ , which decreases with the beam kinetic energy. Thus, in order to measure  $D(z)$  with a given relative spatial resolution, the field shift across the layer,  $\Delta B = \mu_0 j_0 d$  must be kept constant, i.e. one must use the same current, independent of  $d$ . This yields a Joule heating of the film which scales with  $d^{-1}$  and corresponds to 1700 W at room temperature for a 100 nm Cu film ( $40 \times 40 \text{ mm}^2$ ).

At the ISIS pulsed muon source one may reduce drastically this huge dissipation by pulsing the field gradient synchronously with the beam, at 50Hz. With a pulse width of  $20 \mu\text{s}$  — allowing a conservative  $\mu\text{SR}$  time window of 8–9 muon lifetimes — this means a duty cycle of  $10^{-3}$ , hence a dissipation of 1.7 W. We have tested a pulsed device of this kind with various films and different currents, with results close to expectations, demonstrating an extreme case of a 18 nm thick Al film deposited on a mylar substrate.

A vital requirement for the PRI apparatus is the uniformity of the current density within the thin film. This is both easy to obtain and to check in the continuous current mode, but

much less so in the pulsed version, since contacts on a thin film are much more critical and the 20  $\mu\text{s}$  pulse width brings into play the reactance of the device. Therefore we decided to use muons for this purpose as well. However, since the fraction of 3 MeV muons which stop in a very thin film is too small, we reverted to measuring the magnetic field uniformity in the gap inside the current loop, which mirrors the current uniformity in the film. This was achieved by inserting a thin quartz slab in the gap, where the field is maximum, and measuring the inhomogeneous line broadening of the muonium triplet transition. The transition frequency in very low fields is  $\nu = (\gamma_e - \gamma_\mu)B/2 \approx \gamma_e B/2$ , i.e.  $10^2$  that of free muons, therefore it yields a much better sensitivity to spatial field inhomogeneities. To avoid undesirable eddy current effects at the beginning of the current pulse this was anticipated for  $\sim 2 \mu\text{s}$  with respect to the incoming muon bunch.

The experiment was conducted with a linear current density of 166 A/m, and the triplet precession in the quartz sample was 2.7 MHz, appropriate for the expected field of 0.2 mT. The measured precession linewidth was  $0.436 \mu\text{s}^{-1}$ , which coincides with the known lifetime broadening [21] in bulk quartz. The absence of an additional inhomogeneous broadening places an upper limit of 0.1% on the field and current non uniformity.

## 6.4 Conclusions

The experiments reported in this chapter demonstrate the PRI technique at typical energies of conventional  $\mu\text{SR}$  beams. The specific feature of PRI is that the *entire* muon stopping depth distribution is mapped in a *single* measurement.

However, the real interest in such a technique lies in the possibility to perform systematic studies at much lower energies. In this case PRI is a very useful tool for range and straggling studies in metals, practically unrivalled by other methods. Indeed, besides being by far the less time-consuming, it does not require any specially prepared samples (as is the case for the metal-on-insulator systems, necessary for performing the measurements described in section 5.1), and does not suffer from the loss of depth resolution (as happens in a typical rotatable degrader experiment due to the unavoidable straggling introduced by the degrader). Experimental data on range and straggling at moderate and low energies will be essential for designing thin film, multilayer and surface experiments with epithermal muon beams.

The same data are very valuable to test and improve simulation codes which, for the time being, do not handle properly the multiple large-angle scattering and may not account well for the material specific electronic and vibrational excitations at very low energies (below a few keV). Improved simulation codes have already been written, as for instance TRIM.SP (see also section 5.1) [85], which makes this new experimental technique more valuable.

From the experimental side, methods to measure the projected ranges of light ions such as

deuterium at low energies have been recently published, either based on secondary-ion mass spectrometry (SIMS, [81,28]) or on ion beam elastic recoil detection technique (ERD, [122]). All of them are limited by depth resolution. Both methods have been satisfactorily used to measure ranges of  $\sim 1$  keV deuterium ions in Be, C and Si, which represent the state of the art performance. ERD becomes increasingly complex for depths smaller than 50 nm. Within these limits the simulation results obtained by TRIM.SP [85] agree fairly well with experiments.

The positive outcome of preliminary experiments involving the production of strong magnetic field gradients in thin films, together with others regarding the thermal effects of large pulsed currents, demonstrate the viability of the PRI method when using very low energy particles such as epithermal muons.

One limit of the PRI method is that it can be applied only to metals (electric conductors, maybe stretching out to *heavily doped* semiconductors).

Further developments of the Projected Range Imaging method are expected when a pulsed source of epithermal muons will be available for routine experiments at RAL. The present experiments on micron-thick foils could be tested more accurately in thin films, where the pulsed current method is possibly the unique way of measuring range and straggling.

## Chapter 7

# Muons in pulsed magnetic fields

A pulsed epithermal muon beam as the one developed at ISIS, lends naturally itself to  $\mu$ SR studies with pulsed magnetic fields, either synchronous or delayed with respect to the muon pulse arrival. This unique feature can have several interesting applications.

First, it can contribute to resolve important questions concerning the mechanisms of epithermal muon generation in rare gas solids, such as the decisive role played by the muon interaction with the products of its ionisation track or the time-scale of muonium formation.

In other solid films similar questions, such as that of “delayed” muonium and muonium radicals formation, are open for studies and can be investigated with pulsed delayed fields.

Finally, the method makes  $\mu$ SR experiments possible at frequencies higher than the natural bandwidth of a pulsed beam, thus overcoming an intrinsic drawback of pulsed sources.

### 7.1 Introduction

As briefly mentioned in section 2.4, once stopped in matter (with thermalisation times negligibly small if compared to their lifetimes) muons adopt a variety of “chemical” configurations depending on their interactions with the host material. They can range from nearly free muons, (such as in most metals where  $\mu^+$  behaves as a  $s = 1/2$  charged particle with a gyromagnetic ratio of  $\gamma_\mu = 2\pi \cdot 13.55$  kHz/G) to nearly free muonium atoms,  $\text{Mu} \equiv e^- + \mu^+$ , (such as in many insulators) whose electron-muon hyperfine levels are given by the Breit-Rabi diagram (cfr. section 2.4 and figure 33.b). As a comparison, in weak magnetic fields the muonium triplet ( $F = 1$ ) frequency ( $\Delta m_F = \pm 1$ ) is  $\omega_{\text{Mu}} \approx -103\omega_{\mu^+}$ . Muonium, as a highly reactive paramagnetic species, often forms muonium adduct radicals, still paramagnetic but with reduced hyperfine coupling [32] and a large family of  $\mu$ SR studies in this field require the detection of high frequencies in a variety of external magnetic fields.

The formation of muonium may be “hot”, with prompt capture of electrons from the host material, or thermal, i.e. occurring when the muon has already thermalised. A debated

and still largely unanswered question deals with the time scale over which these formation mechanisms take place, both regarding muonium as well as its radicals. A frequent sign of thermal (or *delayed*) processes has been the existence of missing fractions of muonium/radical signals. Only recently some more direct evidence has been produced in condensed rare gasses and semiconductors by using electric fields to study electron mobilities and Mu formation mechanisms [142, 144]. Predictions for liquid hydrocarbons (typically n-hexane) are also available [136]. These experiments give an *indirect* hint that there is a considerable fraction of free epithermal muons  $\mu^+$ , which are created within the escape depth and thus support the picture of “hot” epithermal muon formation (i.e. not created from successive Mu ionisation).

In conventional  $\mu$ SR experiments in static transverse magnetic fields a serious difficulty arises from the loss of phase coherence with time: the formation time, short for epithermal regimes (“hot” reactions), is no longer negligible at thermal regimes and a comparison with the precession period is needed to establish whether phase coherence is conserved or lost. If alternatively the magnetic fields were switched on suddenly, at a controlled delay from the muon implantation time, the phase coherence problem could be avoided. Intuitively speaking, in a *delayed* formation process a *delayed* applied transverse magnetic field recovers the precession phase coherence that could otherwise be lost if the magnetic field were constantly present. More formally, if the formation process is governed by a rate equation, the number of precessing muonium atoms can be described by :

$$N_{\text{Mu}} = N_{\infty}[1 - \exp(-t/\tau)],$$

where  $N_{\infty}$  is the equilibrium number of Mu atoms and  $\tau$  their time constant of formation rate. In a constant magnetic field  $B$  (the precession frequency being  $\omega = \gamma B$ ) one finds for the observable signal:

$$\begin{aligned} S(t) &= \int_0^{\infty} \frac{N_{\infty}}{\tau} e^{-t'/\tau} \cdot \cos[\omega(t-t')] dt' = \\ &= \frac{N_{\infty}}{1 + \omega^2 \tau^2} [\cos(\omega t) + \omega \tau \sin(\omega t)], \end{aligned}$$

which vanishes for  $\tau \gg \omega^{-1}$ . On the contrary, the whole precession signal is recovered as  $S(t) \simeq N_{\infty} \cos(\omega t)$ , if the field is applied at times  $t_s > \tau$ .

In this chapter we demonstrate that such a pulsed field technique is experimentally possible when using pulsed sources of polarised muons which offer the possibility of applying a variety of pulsed excitations, such as the already established radio-frequency resonance [71, 31]. At the same time, the technique allows also to overcome the only drawback of a pulsed beam, namely its limited frequency bandwidth due to the finite muon pulse width. Indeed, the delayed onset of the precession, defined by the instant of application of the pulsed magnetic field, will cancel the effect of the original spread in muon arrival times (see section 3.2.1). We

demonstrate the practical operation of this method by detecting muonium triplet frequencies well above the beam characteristic cut-off values.

A slightly different experimental setup, of particular physical interest, consists in adding a constant field, parallel to the initial muon polarisation. Depending on its intensity, this field can suitably lock the muon polarisation while muons are incoming and before the transverse field is switched on. This configuration offers the unique opportunity to test the “sudden-versus-adiabatic” condition [14, 87] while observing, in real time, the evolution of the muon spins. The connection with the similar case in NMR [1, 139] is straightforward. Put in simple terms, for suddenly changing fields muons will precess around the final field direction, whereas in the opposite adiabatic limit the muon spins will closely follow the field direction. In the following section we focus on the analytical condition of adiabaticity in the particular case of  $\mu$ SR experiments.

## 7.2 Analytical aspects of the adiabatic transition

In many standard quantum mechanics textbooks [14, 87, 121] the adiabatic condition (in Ehrenfest’s sense) is stated as follows: *For a slowly varying Hamiltonian, the instantaneous eigenstates of the Hamiltonian evolve continuously into the corresponding eigenstate at a later time.*

Here we examine the behaviour of a muon spin ensemble, where the “slow” variation of the Hamiltonian is determined by a time-varying magnetic field. The case of a fully spin polarised muon ensemble at rest in a material is similar to that of a family of nuclear moments in an external “magnetising” field  $B_0$ . The effect of time-dependent perturbations is also similar in the two cases, provided we use the *laboratory* frame as an initial reference for muons and an appropriate *rotating* reference frame for the nuclei (NMR). In particular, the analysis of the so-called adiabatic condition (or passage), well known in NMR [1, 139], holds for polarised muons as well and we will rephrase it here in order to make clear the connection to the experimentally measured parameters.

The basic concept is simple and intuitive. In NMR, the nuclear magnetisation is induced by the field  $B_0$  and resonance occurs when a transverse field  $B_1$  is oscillating at the Larmor frequency  $\omega = \gamma B_0$ . One can vary  $B_0$  suddenly or adiabatically from far below to far above the resonance condition. The adiabatic passage through resonance occurs when the nuclear spin magnetisation, in the rotating reference frame at  $\omega$ , remains aligned to the effective field.

For muons, we try to find out an analytical condition for the adiabaticity in a rather general case. A magnetic field having an arbitrary magnitude and direction can always be decomposed into a longitudinal component along the spin direction and a transverse one. So, without loss of generality and adopting an experimental configuration similar to that shown

in figure 47 let us consider the case of a constant, longitudinal magnetic field superimposed to a transverse one, switched on at a controlled rate. Thus we have:

$$\mathbf{B} = \mathbf{B}_{\parallel} + \mathbf{B}_{\perp}(t) = B_{\parallel}\hat{x} + B_{\perp}(t)\hat{z}$$

with the initial muon spin along the  $\hat{x}$  direction.

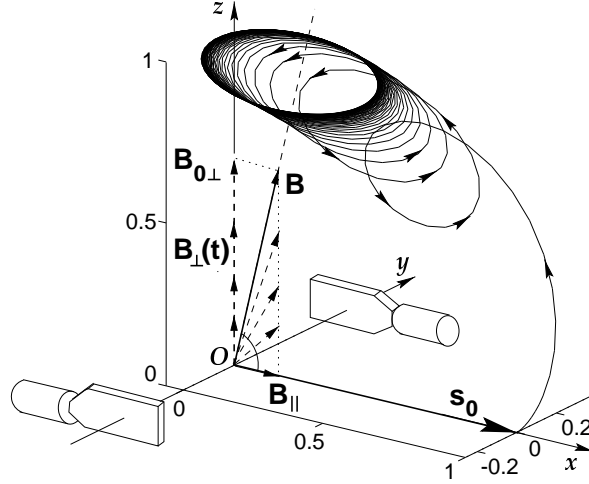


**Figure 47:** Experimental set-up for studying the adiabatic cross-over of Mu. A 3D view of the Mu precession, simulated for a realistic case (relaxation omitted for clarity), is also shown.  $B_{0\perp}$  represents the final value of  $B_{\perp}(t)$ .

The classical time evolution of a spin in a magnetic field  $\mathbf{B}$  is given by:

$$\frac{d\mathbf{s}}{dt} = \mathbf{s} \times (\gamma\mathbf{B}) \quad (39)$$

with  $\gamma$  the *gyromagnetic ratio*. Regardless of the rate with which  $\mathbf{B}$  changes in time,  $s^2$  is conserved as shown by:

$$\frac{ds^2}{dt} = 2\mathbf{s} \cdot \frac{d\mathbf{s}}{dt} = 2\mathbf{s} \cdot \mathbf{s} \times (\gamma\mathbf{B}) = 0.$$

However, only when the field variation is *sufficiently slow*, also the *angle* between  $\mathbf{s}$  and  $\mathbf{B}$  will be a constant of motion.

We now move to a rotating frame of reference (with angular velocity  $\boldsymbol{\Omega}$ ). For an arbitrary vector  $\mathbf{V}$ , the time evolution in the laboratory frame is related to the corresponding one in the rotating frame by [139]:

$$\frac{d\mathbf{V}}{dt} = \frac{\delta\mathbf{V}}{\delta t} + \boldsymbol{\Omega} \times \mathbf{V}$$

where  $\frac{\delta\mathbf{V}}{\delta t}$  is the rate of change of  $\mathbf{V}$  in the rotating frame.

Accordingly, equation (39) in the rotating frame reads:

$$\frac{\delta\mathbf{s}}{\delta t} + \boldsymbol{\Omega} \times \mathbf{s} = \mathbf{s} \times (\gamma\mathbf{B})$$

or:

$$\frac{\delta \mathbf{s}}{\delta t} = \mathbf{s} \times \gamma \left( \mathbf{B} + \frac{\boldsymbol{\Omega}}{\gamma} \right)$$

Now we choose for  $\boldsymbol{\Omega}$  the particular value  $\boldsymbol{\Omega}_B$  which describes the variation of  $\mathbf{B}$  in time. This is equivalent to consider an *effective* field acting on the spins:

$$\mathbf{B}_{\text{eff}} = \mathbf{B} + \frac{\boldsymbol{\Omega}_B}{\gamma}$$

The spin, if initially aligned with the field  $\mathbf{B}(t=0)$ , will precess around the effective field in the rotating frame with an angle  $\phi$  such that:

$$\tan \phi = \frac{\Omega_B}{\gamma B} \quad (40)$$

As we will see below,  $\mu\text{SR}$  can measure directly, with a suitable choice of the experimental geometry, the aperture angle  $\phi$  of the precession cone and therefore it provides a test for the degree of adiabaticity. Just as in NMR, the muon spin  $\mathbf{s}$  will remain aligned to  $\mathbf{B}$  as long as the ratio  $R$  defined by:

$$R = \Omega_B / \gamma B \ll 1 \quad (41)$$

is much less than 1. In our specific case, the time variation of  $B_{\perp} = B_{\perp}(t)$ , implies that both the magnitude and the direction of the total field  $\mathbf{B}$  will vary. In particular the angular velocity is given by:

$$\boldsymbol{\Omega}_B = \frac{\mathbf{B}}{B^2} \times \frac{d\mathbf{B}_{\perp}}{dt}$$

By introducing the Mu (or  $\mu$ ) precession frequency in the field  $\mathbf{B}$ ,  $\omega_{\text{Mu}} = \gamma B$ , and the actual composition of the total field  $\mathbf{B}$ , from the adiabaticity condition (41) one obtains:

$$R(t) = \frac{\dot{B}_{\perp}(t) B_{\parallel}}{\gamma B^3} \ll 1 \quad (42)$$

As we will see in section 7.3, the transverse field  $B_{\perp}(t)$  shows an exponential behaviour and therefore it is the maximum initial value of  $R(t)$ , to control the spin dynamics. Therefore, for practical purposes, it is sufficient to consider the initial ratio  $R_0 = R(0)$ :

$$R_0 = \frac{\dot{B}_{\perp}(0)}{\gamma B_{\parallel}^2} \gg 1. \quad (43)$$

From the last condition we note that there are two independent parameters  $\dot{B}_{\perp}(t)$  and  $B_{\parallel}$  through which we can affect the adiabaticity. Namely, when  $B_{\perp}(t)$  varies “very fast” in time or when  $B_{\parallel}$  is small compared to  $B_{\perp}$ , the condition (42) is violated and one finds a large precession cone; conversely, if  $B_{\perp}(t)$  varies slowly in time or  $B_{\parallel}$  is of the same order of magnitude as  $B_{\perp}$  an adiabatic behaviour and a negligible aperture angle for the precession cone

is expected. In practical cases it is not very easy to adjust the *rise time* of the transverse field while keeping other parameters fixed. One can then conveniently investigate the adiabatic condition by modifying the other parameter, the *longitudinal field*.

The presence of  $\gamma$  in the denominator makes the adiabaticity condition far more easily satisfied for Mu rather than for  $\mu^+$  since  $\gamma_{\text{Mu}} \simeq 103 \gamma_{\mu}$ . Thus we will expect a  $\mu^+$  precession angle very close to the angle corresponding to an ideal sudden pulse, even for relatively high magnetic fields  $B_{\parallel}$ .

We conclude by considering some simple numerical cases which will help us in defining the experimental conditions. Let us suppose switching on a transverse magnetic field of 18 G at an exponential rate of  $1/\tau = 2 \mu\text{s}^{-1}$  in the presence of an applied longitudinal field of 0.5 G. The condition (42) in the case of Mu yields  $R = 16.5$ ; for larger longitudinal fields of  $B_{\parallel} = 2 \text{ G}$  and  $10 \text{ G}$  the values  $R = 1.02$  and  $R = 0.04$  are obtained respectively, which means that by changing  $B_{\parallel}$  non adiabatic, adiabatic or intermediate behaviour can be obtained. In the case of  $\mu^+$  in the same conditions, these ratios are  $R = 1691$ ,  $R = 106$  and  $R = 4.3$ , i.e.  $\mu^+$  behaves always non adiabatically.

### 7.3 Experimental details

The  $\mu\text{SR}$  experiments were carried out on the MuSR instrument of the ISIS Pulsed Muon Facility, which (we recall again) has  $\sim 80 \text{ ns}$  FWHM muon pulses that imply a 6 MHz frequency bandwidth. The sample consisted of a 40 mm diameter disk of fused quartz, thick enough to stop the 26.5 MeV/c muon beam. Muonium Mu [19, 153] triplet transitions could be observed as the largest signal component, together with a smaller diamagnetic precession signal due to  $\mu^+$ . The very different gyromagnetic ratios of these two species ( $\gamma_{\mu}/2\pi = 135.53 \text{ MHz/T}$  and  $\gamma_{\text{Mu}}/2\pi = 13.945 \text{ GHz/T}$ ), not only clearly distinguish the two signals but also offer the possibility of testing the adiabatic condition in two extreme limits.

The chosen experimental geometry (see figure 47) enables us to measure the instantaneous precession cone angle  $\phi(t)$  from the signal asymmetry  $A(t)$  (respectively equal to  $A_{\text{Mu}}$  and  $A_{\mu}$  for Mu and  $\mu^+$ ), being  $A = A_0 \sin \phi$ . Since for an *ideal* sudden pulse, the corresponding maximum signal asymmetry would be  $A_{\text{M}} = A_0 \sin \phi_{\text{sp}} = A_0 / \sqrt{1 + (B_{\parallel}/B_{\perp})^2}$ , for a *real* pulse, by defining the suddenness factor:

$$\mathcal{A} = \frac{\sin \phi}{\sin \phi_0}, \quad (44)$$

we can measure how sudden it is.

Longitudinal magnetic fields are generated by a pair of Helmholtz coils, whereas for the transverse pulsed field we adopted the solution described in the previous chapter. There we saw that a convenient way to generate large magnetic field gradients in small volumes (as is

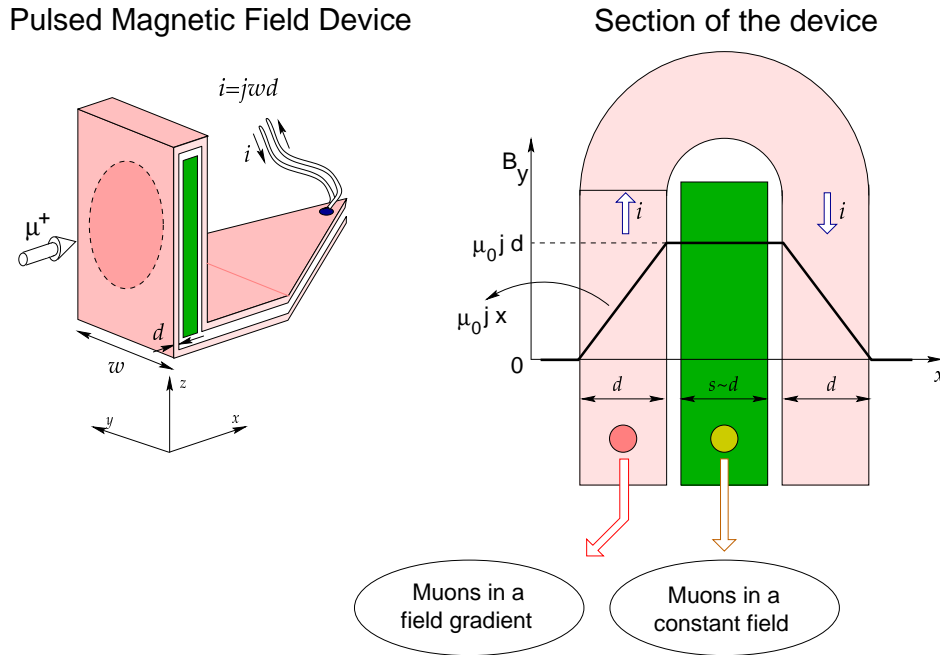


**Figure 48:** The pulsed magnetic field device (left) and its cross section (right). The profile of the magnetic field is also shown. By selectively implanting muons either in a field gradient or in a constant field one can respectively investigate the muon range and straggling or the delayed muonium formation (see text).

the case for the thin samples used in  $\mu$ SR experiments) is to employ a laminar current flat-loop device [135]. To obtain the pulsed magnetic field needed for the experiments on the adiabatic transition we make use of the same device, but now the sample is placed *inside* the loop and therefore it will sense a spatially uniform field. Figure 48, which shows the magnetic field profile along the cross section of the device, should help the reader to distinguish between these two possible applications, depending on where the muons are made to stop. The resulting transverse magnetic field is uniform and equal to  $B_{\perp}(t) = \frac{1}{2} \frac{\mu_0 I(t)}{wd}$  in the sample volume and zero outside it, where  $w$  and  $d$  are respectively the width and thickness of the metallic film where the current flows.

To establish the precise delay of the applied field with respect to the muon pulse arrival one needs to synchronise the device with the machine cycle. This is achieved by triggering the power switching circuit by a suitably delayed reference signal taken directly from the accelerator. Another concern regarded the monitoring of the transverse field rise time which, as can be seen from equation (42), is an important parameter for the present experiment. Figure 49 shows the electronic circuit employed both to drive the pulsed current into the sample loop, as well as to perform the synchronisation and the current monitoring. The profile of the transverse magnetic field is detected by measuring the voltage drop across a calibrated series resistor inserted in the current loop. A digital sampling oscilloscope (DSO) was used

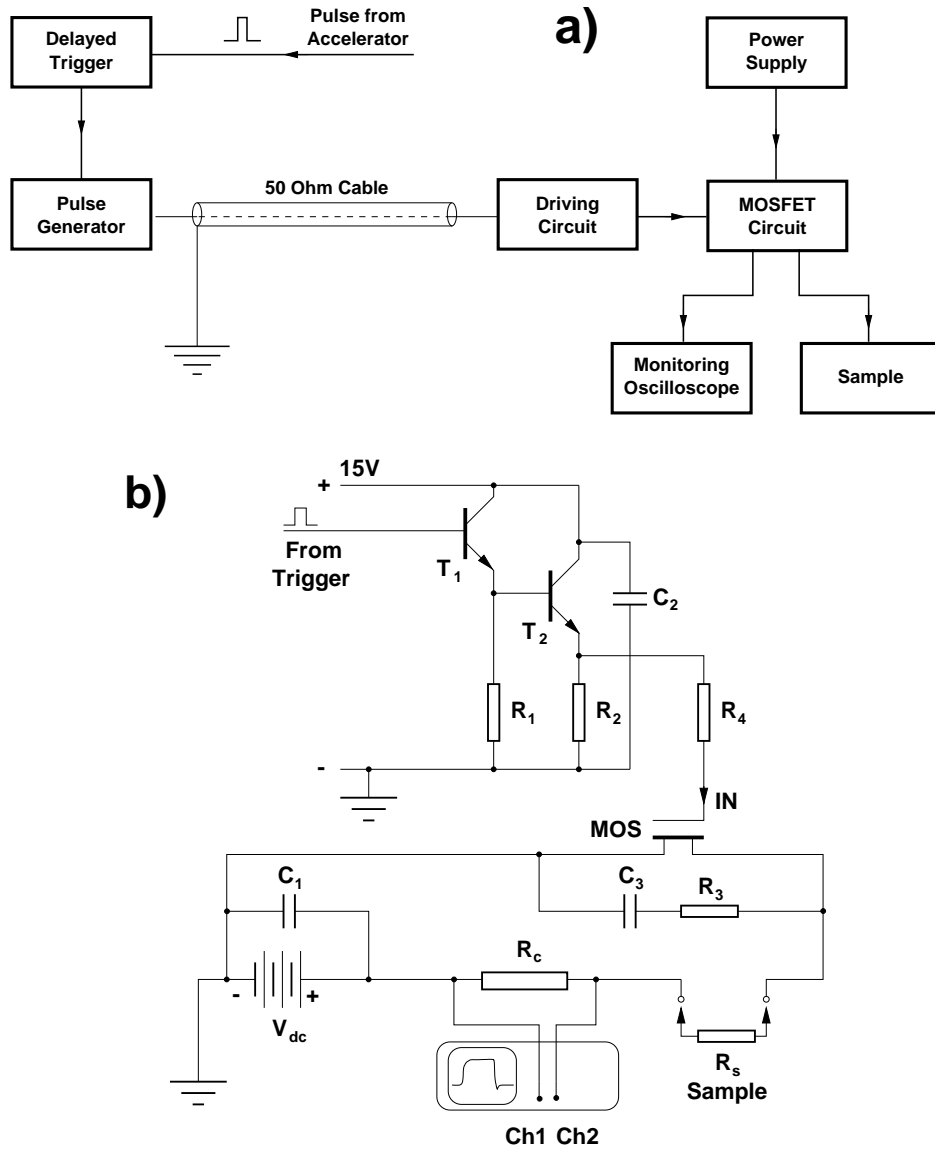


**Figure 49:** Outline of the experimental apparatus (block diagram – top, electronic circuit – bottom). A delayed signal from the main beam triggers the pulse generator. The latter controls the power output of the MOSFET circuit, whose current pulses are delivered to the flat loop around the sample. The orientation of the device and of the current is chosen so as to produce a magnetic field transverse to both the muon spin polarisation and the longitudinal magnetic field. The current is measured by monitoring the differential voltage drop across a calibrated series resistance.

for online recording of the voltage signal whose rising edge is satisfactorily approximated by a double exponential (see figure 50). From a best fit procedure the analytical form of the curve results:

$$B_{\perp}(t) = B_{0\perp} [c_1 \cdot (1 - e^{-t/\tau_1}) + c_2 \cdot (1 - e^{-t/\tau_2})] \quad (45)$$

where  $B_{0\perp} = 18.8 \text{ G}$ ,  $c_1 = 0.8664$ ,  $c_2 = 1.1376$ ,  $\tau_1 = 0.0422 \mu\text{s}$  and  $\tau_2 = 0.5874 \mu\text{s}$ .

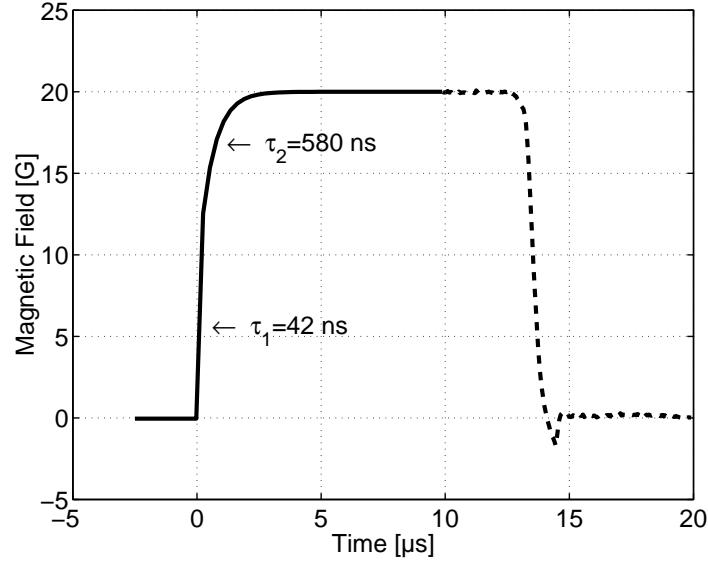


**Figure 50:** Profile of the transverse magnetic field pulse as recorded by the DSO. The rising edge (full line) follows a double exponential as given in equation (45) with two very different time constants. Since the observation time is limited to  $\sim 10 \mu\text{s}$ , the shape of the falling edge (dashed line) is of no concern.

The metallic flat loop with its very low inductance allows a prompt response of the whole pulsed current device. Moreover, the rather large diameter to thickness ratio for the quartz slab ( $\sim 40/0.1$ ), guarantees negligible fringe fields and therefore a uniform magnetic field.

## 7.4 Measurements and data analysis

The device is first calibrated to find the correct delay for synchronising the current pulse with the muon pulse arrival. The knowledge of the accelerator pulse signal allows a preliminary coarse tuning, that is next refined by a subsequent online tuning. The latter consists in maximising the asymmetry signal upon fine variations of delay. The optimal delay value is then kept fixed for all the subsequent measurements.

The first set of experiments was performed in zero longitudinal field and consisted in varying the *time delay* after which the transverse field was switched on with respect to the arrival of the muon pulse. The case  $B_{\parallel} = 0$ , as can be seen from equation (43), is the only special case where the precession cone angle is maximum (being  $\pi/2$  for both Mu and  $\mu^+$ , thus implying a maximum asymmetry signal) and is independent of the rate  $\dot{B}_{\perp}(t)$ . The geometrical precession cone angle and those for Mu and  $\mu^+$  coincide (being all  $\pi/2$ ) and the asymmetry signal for the two muon species reaches its maximum value. Indeed, when  $B_{\parallel} = 0$  the total field  $\mathbf{B}$  would not change in direction, implying an infinite value for  $\Omega_{\mathbf{B}}$  which, as can be seen from condition (40), predicts a maximum cone precession angle of  $\pi/2$ .

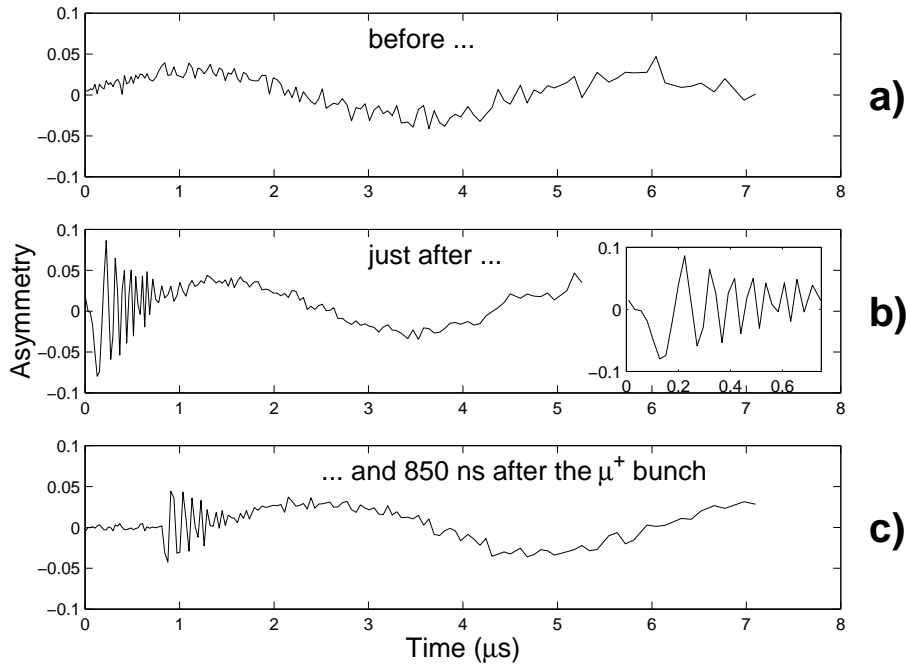


**Figure 51:** Asymmetry signal for different delays of the pulsed transverse field. For magnetic fields switched on *before* the muon pulse arrival (a), Mu atoms precess out of phase and the respective signal cannot be observed. For fields switched on *after* the muon pulse arrival (b, c) no dephasing occurs and the coherent precession signal is recovered. The initial variable frequency signal, due to the gradual increase of the transverse field, is shown in the inset.

A pulsed field which reaches its steady value *before* the muon pulse arrives, as in figure 51.a, is equivalent to a constantly applied field and, since the muonium frequency in 18.8 G (26.2 MHz) exceeds the passband limit, the Mu signal is lost due to dephasing. Unlike Mu,  $\mu^+$  precesses at a frequency well within the bandwidth and its signal is still observable. If, on the other hand, the pulse is started *after* the arrival of muons, no dephasing will occur and the full asymmetry is measured also for muonium, regardless of the amplitude  $B_{\perp}$ . In particular, in figure 51.b  $B_{\perp}$  is delayed by  $\sim 100$  ns, enough to allow the entire muon pulse ( $\sim 80$  ns) to be implanted before any precession takes place.

The measurement of the adiabatic cross-over for Mu and  $\mu^+$ , performed with both the transverse and the longitudinal fields present, yield results qualitatively similar to those shown in figure 51.b. The initial signal amplitude will now vary accordingly to the variation of the  $B_{\parallel}$  parameter. During the measurements the pulsed transverse field reaches a maximum value of  $\sim 18.8$  G, whereas the longitudinal field can be set to any value in the range from zero to 20 G. Changes in  $A_{\text{Mu}}$  are far more dramatic than those in  $A_{\mu}$  due to two orders of magnitude in their gyromagnetic ratios  $\gamma$ . The observation of Mu signals at  $\gamma_{\text{Mu}} B \sim 35$  MHz is again, a *clear evidence of the possibility to take measurements at frequencies well above the normal cut-off of the pulsed beam.*

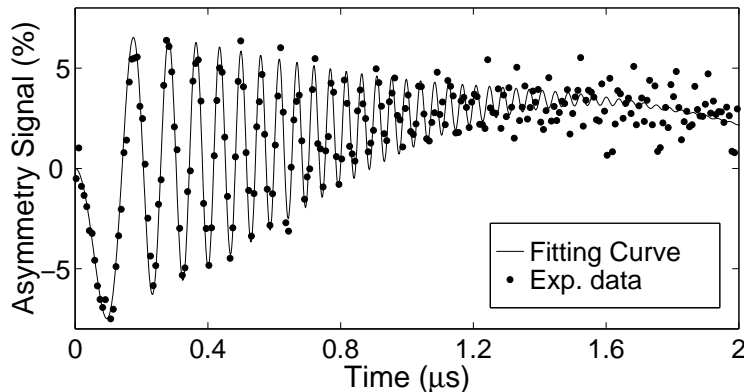


**Figure 52:** Asymmetry signal for  $B_{\parallel} = 2$  G and  $B_{0\perp} = 18.8$  G;  $\bullet$ , experimental data; —, fitting curve. The initial amplitude of the signal is the parameter of interest.

Finally, the Mu signal in quartz shows an intrinsic damping of  $\tau = 0.435 \mu\text{s}^{-1}$  [104] which is easily measured in a 2 G field. At higher fields, the observed signal appears more damped due to the larger splitting of the muonium triplet frequencies.

The procedure to extract the essential information from the raw data includes:

2 (a) – determining the signal amplitude, (b) – normalising the signal amplitude for its “geometrical” change as a function of the longitudinal field, (c) – converting the signal amplitude in a cone-angle value and normalising it to the corresponding  $B_{\parallel} = 0$  value (equal to  $\pi/2$ ).

Particularly for the muonium signal, as it can be readily seen from the inset of figure 51.b, one has a time-dependent frequency which cannot be fitted by standard  $\mu\text{SR}$  data analysis routines. However, the law which governs the change in frequency with time is known: it is given by the shape of the pulsed field as in (45). Therefore it is possible to use a *heterodyne* type of conversion of the raw data by mixing them with the reference signal generated from formula (45). In this heterodyne procedure, the reference signal can be finely tuned in amplitude, initial time, phase shift and even the parameters controlling the shape of the pulse itself can be changed. These degrees of freedom will be useful in discussing minor differences between the “real” pulse and the recorded one.

The fit of the asymmetry signal for the particular case when  $B_{\parallel} = 2$  G is shown in figure 52. The fitting curve, based on both Mu and  $\mu^+$  spin precessions in the presence of the time-dependent magnetic field, follows quite closely the raw data and from it one can extract the initial value of the asymmetry signal.

The signal amplitudes thus obtained decrease as the longitudinal field is increased, both as a result of the adiabatic change-over and because of the geometrical reduction of the cone angle. After the correction of the measured amplitudes by the factor  $1/\sin \phi_{\text{sp}} = \sqrt{1 + (B_{\parallel}/B_{\perp})^2}$  and the normalisation to the  $B_{\parallel} = 0$  value, one obtains the suddenness

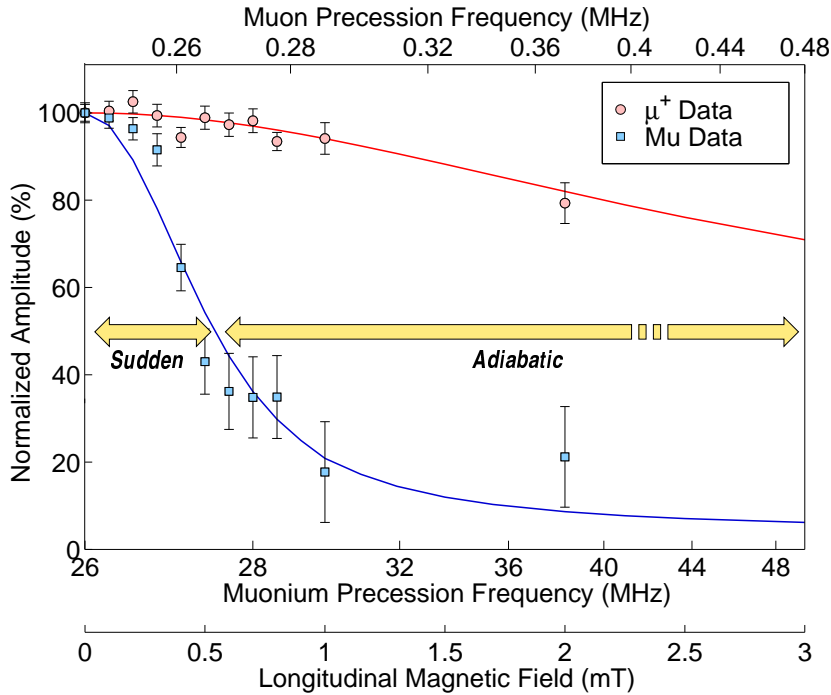


**Figure 53:** Experimental results for the adiabatic cross-over of Mu ( $\square$ ) and  $\mu^+$  ( $\circ$ ) normalised and corrected for  $1/\sin \phi_{sp}$  (see text) as a function of the longitudinal magnetic field. Lines represent the results of numerical calculations. The frequency scales for Mu and  $\mu^+$  refer to the corresponding precession in the steady-state total field  $B$ .

factor defined by equation (44) and the results are shown in figure 53.

For muonium, one can see that the sudden to adiabatic cross-over occurs in the range  $B_{\parallel} = 3 - 6$  G while, as expected, for  $\mu^+$  the same transition takes place at much higher fields – by extrapolation – close to 100 G. Note that the drop of the measured asymmetry is not a passband effect (there is no intrinsic frequency resolution limitation) but just the effect of the finite switching speed for the field  $\dot{B}_{\perp}$ .

The numerical solution of the equation  $\dot{\mathbf{s}} = \mathbf{s} \times (\gamma \mathbf{B})$  describing the muon spin evolution, with the experimental conditions (i.e. parameters  $B_{\parallel}$ ,  $B_{\perp}$ ,  $c$ ,  $\tau$ , detector positions, etc.) thoroughly taken into account, provides an immediate visualisation of the spin precession and, more importantly allows a comparison with the experimental values.

Such a simulated solution, for the particular case  $B_{\parallel} = 4$  G and  $B_{0\perp} = 18.8$  G, is shown in figure 54. The  $\mu^+$  spin, initially dragged by the fast changing  $\mathbf{B}$ , enters an adiabatic regime and eventually stabilises on the asymptotic precession cone as  $\mathbf{B}$  approaches its final value. The components of the precessing spin along the three main directions  $\hat{x}$ ,  $\hat{y}$  and  $\hat{z}$ , shown in figure 54.a, are proportional to the asymmetry signal in appropriate detectors. In particular, the  $y$ -projection is strictly related to the precession cone angle and is not sensitive to the change in direction of  $\mathbf{B}$ , which takes place in the  $0xz$  plane. Hence, as shown also in figure 47, the preferred choice of the telescopes from which the experimental asymmetry

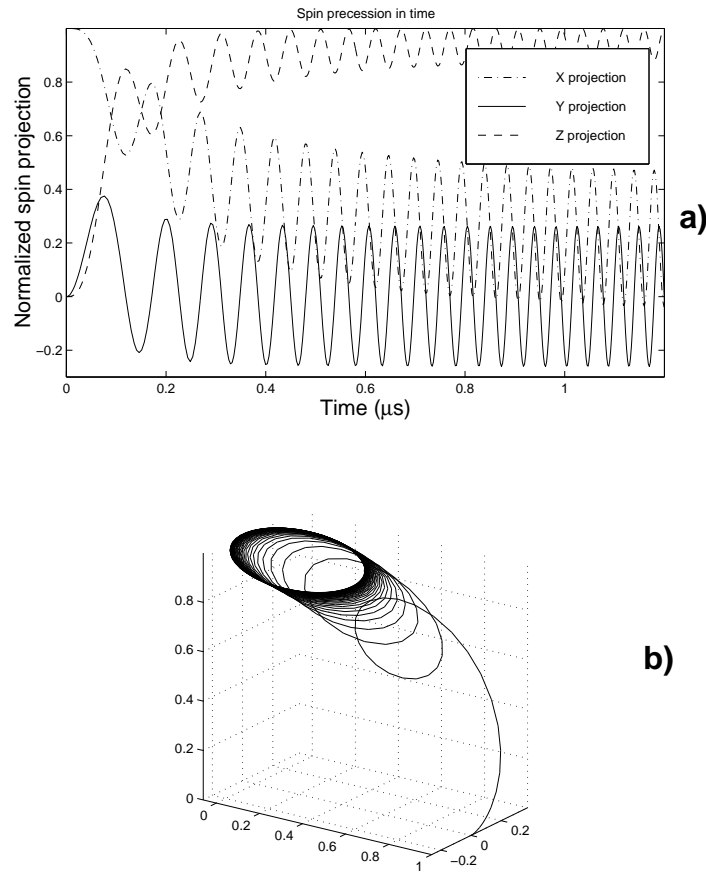


**Figure 54:** a) Simulated spin precession for  $B_{\parallel} = 4\text{ G}$  and  $B_{0\perp} = 18.8\text{ G}$ . Since the spin is initially aligned along the  $\hat{x}$  direction its  $x$ -projection is maximum at the beginning. The  $y$ -projection is strictly related to the cone of precession and is not sensitive to the change in direction of  $\mathbf{B}$  which takes place in the  $0xz$  plane.

b) 3D view of the same precession. During the initial fast rise of the transverse field the spin behaves almost non adiabatically, but when the field  $\mathbf{B}$  approaches its final direction the spin follows it more and more closely and eventually stabilises on the asymptotic precession cone (not shown).

was calculated, is that whose axis coincides with the  $\hat{y}$  direction. The similarity between the simulated  $y$ -projection (full curve in figure 54.a) and the measured signal (see e.g. figure 51.b) is noticeable.

From the numerical solution of the muon spin evolution we obtain the solid curves shown in figure 53, corresponding to the following values of the experimental parameters:  $B_{0\perp} = 18.9(2)\text{ G}$ ,  $\tau_1 = 0.06(2)\text{ μs}$ ,  $\tau_2 = 0.4(1)\text{ μs}$ ,  $c_1 = 0.9(5)$ ,  $c_2 = 1.1(6)$ . These values are generally in good agreement with the results of direct measurement of the pulse shape as given by (45), even though they predict a cross-over at slightly larger longitudinal fields. It would seem sensible to simulate “slower” fields and calculate the cross-over again, were it not for the fact that four independent parameters are involved:  $c_1$ ,  $c_2$ ,  $\tau_1$  and  $\tau_2$  (see formula (45)). As a guided guess we assume that the most crucial parameter is the short time constant  $\tau_1$  which is

made longer in the remaining three curves. It appears, by comparison with the experimental data, that  $\tau_1$  alone suffices to induce a much better agreement.

Other causes can be pointed out as a source of minor systematic discrepancies between the present experiment and the theory:

- Muonium relaxation in quartz:  
The natural Mu relaxation in quartz (Lorentzian with  $\tau_L = 0.435 \mu\text{s}^{-1}$ ) reduces the measurement time for muonium. This forces the cone angle to be extracted from the muonium signal amplitude at  $t = 0$ . This constraint is normally irrelevant for the correctness of the procedure, except near the cross-over interval from adiabatic to sudden regimes where, even in the present transverse experimental geometry, the  $t = 0$  amplitude slightly overestimates the cone angle in the “sudden” side of the transition.
- The beating between the two Mu triplet frequencies (see figure 33.b) becomes more relevant at high fields [104] since for them the frequency splitting, given by  $\Delta\nu = \nu_{12} - \nu_{23}$ , increases. Here  $\nu_{12} = \nu_- - \Omega$ ,  $\nu_{23} = \nu_- + \Omega$ ,  $\nu_- = 1/2 \cdot (\nu_{e^-} - \nu_{\mu^+})$ ,  $\Omega = 1/2 \cdot (\sqrt{(\nu_{e^-} + \nu_{\mu^+})^2 + A^2} - A)$ , where  $A = 4.4633$  GHz is the hyperfine frequency, whereas  $\nu_{e^-}$  and  $\nu_{\mu^+}$  are the Larmor frequencies of the electron and muon respectively. As an illustrative example, for an applied field of 20 G one finds a splitting of  $\Delta\nu \simeq 0.3$  MHz. Because of this splitting the heterodyne conversion, performed by beating with a single frequency followed by a high frequency filtering, introduces a loss in amplitude which becomes bigger the larger the value of  $B$ , i.e. on the “adiabatic” side of the cross-over.

## 7.5 Discussion and conclusions

We have shown that in a pulsed muon beam characterised by periodic packets of muons having a time spread  $\delta t$ , the intrinsic frequency bandwidth can be extended by pulsing the external magnetic field *after* the muons have thermalised in the host material. For the ISIS time spread of  $\sim 80$  ns the frequency bandwidth is  $\sim 6$  MHz. In the present experiment the time resolution of the electronics (8 ns) limited the observable frequencies to  $\sim 40$  MHz, which by no means is an intrinsic limit.

We also studied directly in the “laboratory frame of reference” the cross-over between sudden and adiabatic regimes by measuring the amplitude of the Larmor precession in the instantaneous magnetic field. The experiment performed on a quartz sample offers two independent spin probes: free muons and muons in muonium atoms, differing by a factor  $\sim 100$  in their relative gyromagnetic ratios. We have shown how this factor effectively sets the scale for the transition between sudden and adiabatic regimes.

The technique demonstrated in this chapter opens new perspectives for a straightforward detection of the *delayed* paramagnetic species which account for missing muon fractions in many materials. By means of faster pulsed power supplies the kinematics of delayed formation may be studied directly, therefore allowing detailed investigations of the epithermal muon generation processes.

For the envisaged applications of this pulsed procedure, the sudden regime is the most interesting since it allows switching to a precession mode with a large precession cone at the desired time. The presence of a static longitudinal field to preserve a large initial muon spin polarisation can be very important typically in two cases:

- a) when local random static fields present in the host material, such as nuclear dipole fields, would relax the spin polarisation in the time lapse between the muon thermalisation and the switching on of the transverse magnetic field;
- b) when muonium radicals subject to transferred hyperfine interaction with host nuclei are formed, since the latter must be decoupled from the muon spin by a sufficiently large field to preserve the muon spin polarisation.

For muonium, and probably for a variety of radical states, the sudden regime holds up to a few gauss, given the intensity and the rise time of the transverse field used in this experiment. However, the cross-over field can be shifted to larger values of  $B_{\parallel}$  by increasing  $B_{\perp}$  and by reducing its rise time. From the present experiment, we know that  $B_{\perp}$  as high as 100 G are obtained without modifying the switching device. The problem concerning the rise time is the one more open to further improvements and tests. As previously shown, the rising edge of the field pulse is characterised by two time constants. This seems related to the existence of two regimes in the switching MOS transistor, which differ significantly in the value of the gate-to-drain capacitance. On the other hand, comparisons between the current pulse and the magnetic field pulse indicate that only the fastest time constant  $\tau_1$  is modified. This suggests that possible improvements are to be sought in the direction of further reduction of the flat loop inductance, the reduction of stray inductance of the switching circuit and the minimization of the frequency dependent losses in the conductors.

## Chapter 8

# Conclusions and outlook

The work described in the present thesis was part of a collaborative effort, whose final goal was the further extension of the potentialities offered by the conventional  $\mu$ SR method to the low energy range, i.e. to the study of thin films, surfaces and interfaces.

Two main subjects were touched upon. One regarded the generation of epithermal muons, the setup and properties of the pulsed slow muon beam as well as measurements in thin films and nanostructures. The other was concerned with the developments relying on the synchronous application of pulsed magnetic fields, useful for investigations in low dimensionality systems.

The production of spin polarised epithermal muons was achieved at the ISIS pulsed muon source, at the Rutherford Appleton Laboratory (UK), using the method of muon moderation in rare gas solids. Successively, in the search for an optimal beam setup, several factors which affect the slow muon yield were carefully studied including: the moderator film thickness, its growing pressure and temperature, the deposition rate, the heat treatment, etc. The overall production efficiency is about  $10^5$  slow muons per incoming fast muon. Besides on solid rare gases, measurements of moderation efficiencies were performed also for different moderating materials including solid nitrogen and carbon dioxide, and even aluminium and diamond. They confirm the noble gases (in particular Ar) as the best muon moderators.

For the first time the initial energy distribution of slow muons could be measured by applying retarding potentials to the substrate. Detailed analyses show a 25 eV wide (FWHM) distribution in case of argon, consistent with the present theories on particle moderation, which predict a muon energy distribution of the same order as the energy gap of the material.

The pulsed feature of the present slow muon beam provides an excellent energy resolution. This, together with the possibility of beam energy tuning, permitted two interesting applications to be demonstrated. One regarded the study of epithermal muon implantation profile in a copper on quartz sample. Not only could we map the stopping profile, but also evidence about the presence of a 2 nm copper oxide surface layer was found. The study of magnetic

thin films instead was concerned with a hexagonal cobalt film on a copper substrate.

The second part of the thesis was dedicated to the practical implementation of the synchronously applied magnetic fields, focusing mainly on two of its uses: the projected range imaging and the study of adiabatic to non-adiabatic crossover, both in view of future LE- $\mu$ SR applications. The external pulsed magnetic field and/or field gradient were generated by a laminar current-loop method. The use of field gradients permitted the imaging of the implantation profile of positive muons in thin metal foils. The use of spatially uniform pulsed fields instead, proved an interesting method for the direct measurement of the sudden-to-adiabatic cross-over, which could be applicable to the problem of the delayed muonium formation.

Several problems, both of theoretical and of experimental character, are to be faced in the near future. Among the theoretical questions, the most important one is that concerned with the deeper understanding of the basic processes responsible for epithermal muon generation. This would have important implications for a decisive improvement in the slow muon yield. The main difficulties are represented by the very scarce experimental data presently available in the low energy range and by the need to take into account mechanisms involving many body effects, essential in these regimes.

On the experimental side, the presently developed beam at ISIS represents the precursor of the future pulsed epithermal muon beams, which when installed on high intensity sources of the next generation, like e.g. the ESS (European Spallation Source), would provide a new powerful tool for nanoscale studies.

The present beam could be improved by sensibly reducing its beam spot size, both with a reduction in the size of the original surface muon beam and, more importantly, through an improved design of the electrostatic transport system. For instance, just the symmetrical positioning of the last focusing lens is supposed to give a significantly better beam image. Other possibilities have also been considered [108].

A more complex sample station, which will allow studies in a variety of physical conditions, is also foreseen. Measurements on a wide temperature range, from liquid helium temperature up to some hundreds of degrees could then be performed. The future sample station will be provided also with *in situ* sample preparation, cleaning and characterisation instruments, an important requirement when working with surfaces and thin films.

Finally, the two methods based on the application of pulsed magnetic fields, could be put into use, once an epithermal muon beam of sufficiently high intensity would be available on a routine basis.

# Appendix A

## Energies in pion and muon decays

In this appendix we calculate in detail the maximum energy for decay positrons, the energy of surface muons and the threshold energy for single pion production. These values were mentioned in the introductory and in the second chapter.

We start from the well known formulae for the relativistic energy (see e.g. [118]):

$$E_0^2 = E^2 - p^2 c^2 \quad (46)$$

$$E_0 = E - T, \quad (47)$$

where  $E$  and  $T$  represent respectively the total and the kinetic energy of a particle in a given frame of reference,  $p$  is its spatial momentum, whereas  $E_0 = m_0 c^2$  is the Lorentz-invariant particle energy in its rest reference frame. With some simple rearrangements one obtains:

$$p^2 c^2 = T^2 + 2TE_0 \quad (48)$$

### A.1 Maximum energy for decay positrons

Let's consider first the decay:

$$\mu^+ \longrightarrow e^+ + \nu_e + \bar{\nu}_\mu \quad (49)$$

From the energy conservation law it follows:

$$E_\mu = E_e + E_{\nu, \bar{\nu}} \quad (50)$$

The decay positron will carry the maximum available kinetic energy  $T = T_{\max}$ , when both neutrinos travel together in opposite direction with respect to its. From the momentum conservation law one can write:

$$p_{\nu, \bar{\nu}} = p_e \quad (51)$$

Taking into account equation (50), the fact that  $m_\nu \equiv 0$  and the last relation, one finds:

$$E_\mu = E_e + p_e c = (E_{0e} + T_e) + p_e c \quad (52)$$

which can also be written:

$$(E_\mu - E_{0e} - T_e)^2 = p_e^2 c^2 = T_e^2 + 2T_e E_{0e} \quad (53)$$

where relation (48) was used. After some simple rearrangements the final result is obtained:

$$T_e = \frac{1}{2} m_\mu c^2 \left[ 1 + \left( \frac{m_e}{m_\mu} \right)^2 \right] - m_e c^2 \quad (54)$$

Substitution of the numerical values  $m_\mu = 105.66 \text{ MeV}/c^2$  and  $m_e = 0.511 \text{ MeV}/c^2$  yields the maximum kinetic energy of the emitted decay positrons:  $T_e^{\text{max}} = 52.831 \text{ MeV}$ .

## A.2 Energy of surface muons

Analogous considerations to those shown above can be used to determine the energy of “surface” muons. In this last case the relevant decay is:

$$\pi^+ \longrightarrow \mu^+ + \nu_\mu \quad (55)$$

It is easily seen that here the role of muons and positrons involved in decay (49) is played respectively by pions and muons. Thus the formal substitution of their masses into equation (54) gives:

$$T_\mu = \frac{1}{2} m_\pi c^2 \left[ 1 + \left( \frac{m_\mu}{m_\pi} \right)^2 \right] - m_\mu c^2 \quad (56)$$

By taking into account that pion mass is  $m_\pi = 139.57 \text{ MeV}/c^2$ , the energy of “surface” muons turns out to be  $T_\mu = 4.119 \text{ MeV}$ . Note that here the muons are monoenergetic since they originate from a two body decay.

## A.3 Energy threshold for single pion production

Finally we calculate the energy threshold for *single* pion production due to reactions like:

$$p + p \longrightarrow p + p + \pi^0 \quad (57)$$

In this case the energies and momenta appearing in (46) represent those of the system as a whole and  $E_0$  corresponds to  $E_{CM}$ , the total energy in the centre of momentum (CM)

reference frame.

Before the collision the relation:

$$E_{CM}^2 = E^2 - p^2 c^2 \quad (58)$$

$$= (E_1 + E_2)^2 - (p_1 + p_2)^2 c^2 \quad (59)$$

$$= m_1^2 c^4 + m_2^2 c^4 + 2 E_1 E_2 (1 - \beta_1 \beta_2 \cos \theta) \quad (60)$$

holds, where  $\beta \equiv \frac{v}{c} = \frac{pc}{E}$ ,  $\theta$  is the collision angle and  $m_i$  denote the rest masses of particles. Since in the laboratory frame  $E_1 = E_{1\text{Lab}} = E_{\text{Lab}}$  and  $p_2 \equiv 0$  (which implies  $E_2 = m_2 c^2$ ), it follows that:

$$E_{CM}^2 = m_1^2 c^4 + m_2^2 c^4 + 2 E_{\text{Lab}} m_2 c^2 \quad (61)$$

After the collision on the other hand, considering that in the CM frame  $\sum \vec{p}_i = 0$ , one has:

$$E_{CM} = (m_1 + m_2 + m_\pi) c^2 \quad (62)$$

Now it is straightforward to obtain the total energy in the laboratory frame from the last two equations:

$$E_{\text{Lab}} = m_p c^2 \left[ 2 \left( 1 + \frac{m_\pi}{2m_p} \right)^2 - 1 \right] \quad (63)$$

By substituting  $m_p = 938.27 \text{ MeV}/c^2$  for the proton rest mass and by using the relation (48) one readily obtains:

$$E_{th} = T = E_{\text{Lab}} - m_p c^2 = 280 \text{ MeV} \quad (64)$$

as the threshold kinetic energy for single pion production. One must note however that  $\pi^0$  does not decay into a muon, so the useful threshold is that for  $\pi^+$  or  $\pi^-$  production, which turns out to be at slightly higher energies,  $E_{th} = 291 \text{ MeV}$ .

## Appendix B

# Some formulae for the fits

In this appendix we deduce some of the formulae which were used to fit the experimental data of range and straggling reported in chapter 6. We make use of physically based considerations to obtain fit functions which one could reasonably expect data would follow.

The straggling of energetic particles into a given material [103] depends upon several factors, but only two of them play a dominant role:

- the energy distribution of the implanted particles and,
- the type of material medium with which they interact.

In the ideal condition of a completely monoenergetic particle beam, the straggling would be entirely determined by the characteristics of the material. Inside the stopping target the particles will lose their energy in small discrete amounts. Nevertheless, since their energy is quite high as compared to the ionisation energy transferred to the material in a single collision event, it is easy to realize that before a particle stops it will undergo a *large* number of collisions which *fluctuates* around a certain mean value. This phenomenology is well described by a *Gaussian* distribution of the ranges  $R$  around a mean range  $R_0$  and by a straggling parameter  $\sigma$ . By calling  $g(x)$  this distribution function, that for simplicity we assume to be normalized, one has:

$$g(x) = \frac{1}{\sqrt{2\pi}\sigma} \exp\left[-\frac{(x - R_0)^2}{2\sigma^2}\right], \quad \text{with} \quad \int_{-\infty}^{\infty} g(x) dx = 1. \quad (65)$$

Considering the beam to be perfectly monochromatic is however a rather unreal assumption, so in a more realistic picture one characterizes the beam also by the straggling of momenta of its particles  $\Delta p/p$  (called also momentum “bite”).

Therefore one could imagine the real beam as if it were composed of a large number of particle *ensembles* all having well defined momenta. Once inside the material, each of these ensembles will give rise to a straggling which depends only on *intrinsic* characteristics of the medium.

Now, it is evident that the *total* straggling  $\sigma$  is nothing else but a weighted sum of all the intrinsic stragglings.

The choice of the weighting function  $w(p)$  is really an arduous task, unless one knows *a priori* the energetic spectrum of the beam. We can assume e.g. that the function  $w(p)$  has the shape of a square or a Gaussian window. In the first case we can write:

$$w(p) = \begin{cases} 1, & \text{if } |p - d| \leq b; \\ 0, & \text{if } |p - d| > b. \end{cases} \quad (66)$$

The theoretical fitting function  $f(x)$  will be therefore given by a convolution of the two functions:

$$f(x) = g(x) * w(p) = \int_{-\infty}^{\infty} g(x - \xi) w(\xi) d\xi \quad (67)$$

The calculation of the integral is made easier by the fact that the function  $w(p)$  is zero outside the interval  $[d - b, d + b]$ :

$$f(x) = \int_{d-b}^{d+b} \frac{1}{\sqrt{2\pi}\sigma} \exp\left[-\frac{((x - \xi) - R_0)^2}{2\sigma^2}\right] d\xi = \frac{1}{2} \operatorname{erf}\left(\frac{R_0 + \xi - x}{\sqrt{2}\sigma}\right) \Bigg|_{\xi=d-b}^{\xi=d+b} \quad (68)$$

which yields the shape of the straggling curve, comprising both the intrinsic straggling and the  $\Delta p/p$  of the beam:

$$f(x) = g(x) * w(p) = \frac{1}{2} \left[ \operatorname{erf}\left(\frac{R_0 + d + b - x}{\sqrt{2}\sigma}\right) - \operatorname{erf}\left(\frac{R_0 + d - b - x}{\sqrt{2}\sigma}\right) \right] \quad (69)$$

However the experiment allows one to measure only the variations of the asymmetry signal as a function of the degrader thickness, which means that the experimental data will lie on a curve  $F(x)$  representing just the integral of the function  $f(x)$ :

$$F(x) = \int f(x) dx$$

Once carried out the simple, though cumbersome, calculations, the fitting function has the following analytical form:

$$F(x) = \frac{1}{2} \left\{ \frac{-\sigma}{\sqrt{2\pi}} \exp\left[-\frac{(R_0 + d + b - x)^2}{2\sigma^2}\right] - \frac{R_0 + d + b - x}{2} \operatorname{erf}\left(\frac{R_0 + d + b - x}{\sqrt{2}\sigma}\right) + \frac{\sigma}{\sqrt{2\pi}} \exp\left[-\frac{(R_0 + d - b - x)^2}{2\sigma^2}\right] + \frac{R_0 + d - b - x}{2} \operatorname{erf}\left(\frac{R_0 + d - b - x}{\sqrt{2}\sigma}\right) \right\} \quad (70)$$

This is the function which was used to obtain the results reported in chapter 6.

In a completely analog way, in case the weighting function is assumed to be a Gaussian, one has:

$$w(p) = \frac{1}{\sqrt{2\pi}b} \exp\left[-\frac{(x - d)^2}{2b^2}\right] \quad (71)$$

and, recalling that the convolution of two Gaussian curves is still a Gaussian and that the integral of a Gaussian yields the *error function*, one finds for  $F(x)$ :

$$F(x) = \frac{1}{2} \operatorname{erf} \left[ -\frac{(x - R_0 - d)^2}{\sqrt{2(b^2 + \sigma^2)}} \right] \quad (72)$$

One observes from the formulae (70) and (72) that the quantities  $d$  and  $R_0$  appear only in the form of the sum  $R_0 + d$ . This means that during the fits it is possible to assign them to a single variable, or equivalently we can suppose  $d \equiv 0$  and replace  $R_0 + d$  with  $R_0$ . With this last substitution the fit formulae are somewhat simplified respectively in:

$$F(x) = \frac{1}{2} \left\{ \frac{-\sigma}{\sqrt{2\pi}} \exp \left[ -\frac{(R_0 + b - x)^2}{2\sigma^2} \right] - \frac{R_0 + b - x}{2} \operatorname{erf} \left( \frac{R_0 + b - x}{\sqrt{2}\sigma} \right) \right. \\ \left. + \frac{\sigma}{\sqrt{2\pi}} \exp \left[ -\frac{(R_0 - b - x)^2}{2\sigma^2} \right] + \frac{R_0 - b - x}{2} \operatorname{erf} \left( \frac{R_0 - b - x}{\sqrt{2}\sigma} \right) \right\} \quad (73)$$

for the case of a square distribution of momenta, and

$$F(x) = \frac{1}{2} \operatorname{erf} \left[ -\frac{(x - R_0)^2}{\sqrt{2(b^2 + \sigma^2)}} \right]. \quad (74)$$

for a Gaussian distribution of momenta.

# References

- [1] ABRAGAM, A. *The Principles of Nuclear Magnetism*. No. 32 in The International Series of Monographs on Physics. Clarendon Press, Oxford, 1983.
- [2] ADAIR, R. K., AND KASHA, H. Cosmic-Ray Muons. In *Muon Physics*, V. W. Hughes and C. S. Wu, Eds., vol. 1 (Electromagnetic Interactions). Academic Press, Inc., New York, 1977, pp. 324–385.
- [3] AHN, H. E. *Angular Distribution Measurement of Beam-Foil Muonium*. PhD thesis, Yale University, 1992.
- [4] BACHER, R., BLÜM, P., GOTTA, D., HEITLINGER, K., SCHNEIDER, M., MISSIMER, J., AND SIMONS, L. M. Relevance of ionization and electron refilling to the observation of the  $M1$  transition ( $\gamma M1: 2s-1s$ ) in light muonic atoms. *Physical Review A* 39, 4 (February 1989), 1610–1620.
- [5] BACHER, R., BLÜM, P., GOTTA, D., HEITLINGER, K., SCHNEIDER, M., MISSIMER, J., SIMONS, L. M., AND ELSENER, K. Degree of ionization in antiprotonic noble gases. *Physical Review A* 38, 9 (1988), 4395–4404.
- [6] BADERTSCHER, A., EGAN, P. O., GLADISCH, M., GREENE, M., HUGHES-VW, V. W., MARIAM, F. G., LU, D. C., ZU PUTLITZ, G., RITTER, M. W., SANDERS, G., SOUDER, P. A., AND WERBECK, R. Development of ‘subsurface’ positive muon beam at LAMPF. *Nuclear Instruments & Methods in Physics Research A* 238, 2-3 (August 1985), 200–205.
- [7] BAILEY, J., BORER, K., COMBLEY, F., DRUMM, H., KRIENEN, F., LANGE, F., PICASSO, E., VON RUDEN, W., FARLEY, F. J. M., FIELD, J. H., FLEGEL, W., AND HATTERSLEY, P. M. Measurements of relativistic time dilatation for positive and negative muons in a circular orbit. *Nature* 268, 5618 (28 July 1977), 301–305.
- [8] BEER, G. A., MARSHALL, G. M., MASON, G. R., OLIN, A., GELBART, Z., KENDALL, K. R., BOWEN, T., HALVERSON, P. G., PIFER, A. E., FRY, C. A., WARREN, J. B., AND KUNSELMAN, A. R. Emission of muonium into vacuum from a silica powder layer. *Physical Review Letters* 57, 6 (August 1986), 671–674.
- [9] BETHE, H. A., AND ASHKIN, J. Passage of radiation through matter. In *Experimental Nuclear Physics*, E. Segrè, Ed., vol. 1. John Wiley & Sons, Inc., New York, 1953-1959.
- [10] BEVINGTON, P. R. *Data Reduction and Error Analysis for the Physical Sciences*. McGraw-Hill, New York, 1969.
- [11] BIRSACK, J. P. Ion ranges and energy deposition in insulators. In *Ion Beam Modification of Insulators*, P. Mazzoldi and G. W. Arnold, Eds. Elsevier Publishers, Amsterdam, 1987.
- [12] BINDER, K., AND HEERMANN, D. W. *Monte Carlo Simulation in Statistical Physics: An Introduction*. Springer Verlag, New York, December 1997.
- [13] BLUNDELL, S. J. Spin-polarized muons in condensed matter physics. *Contemporary Physics* 40, 3 (1999), 175–192.
- [14] BOHM, D. *Quantum theory*. Prentice-Hall physics series. Prentice-Hall, Englewood Cliffs, New Jersey, 1960.

- [15] BORDEN, A. I., CARNE, A., CLARKE-GAYTHER, M., EATON, G. H., JONES, H. J., THOMAS, G., HARTMANN, O., AND SUNDQVIST, T. UPPSET: a pulsed electrostatic kicker to improve the  $\mu$ SR frequency response in the ISIS pulsed muon beam. *Nuclear Instruments & Methods in Physics Research, A* 292, 1 (June 1990), 21–29.
- [16] BOWEN, T. The surface muon beam. *Physics Today* (July 1985), 22–34.
- [17] BRADT, H. V., AND CLARK, G. W. Polarization of cosmic-ray  $\mu$  mesons. *Physical Review B* 132 (1963), 1306.
- [18] BREITRÜCK, A. Charakterisierung eines gepulsten Strahles ultrakalter polarisierter Myonen. Diplomarbeit, Ruprecht Karls Universität, Heidelberg, 1998.
- [19] BREWER, J. H. Muon spin rotation, relaxation and resonance. In *Encyclopedia of Applied Physics*, G. L. Trigg, Ed., vol. 11. VCH Publishers, Inc., New York, 1994, pp. 23–53.
- [20] BREWER, J. H. A Brief History of  $\mu$ SR, 20 August 2000. <http://musr.org/intro/musr/-history.htm>.
- [21] BREWER, J. H., CROWE, K. M., GYGAX, F. N., AND SCHENCK, A. Positive muons and muonium in matter. In *Muon Physics*, V. W. Hughes and C. S. Wu, Eds., vol. 3 (Chemistry and Solids). Academic Press, Inc., New York, 1975.
- [22] BREWER, J. H., AND CYWINSKI, R.  $\mu$ SR: an introduction. In *Muon Science: Muons in Physics, Chemistry and Materials* (Bristol and Philadelphia, 1999), S. L. Lee, S. H. Kilcoyne, and R. Cywinski, Eds., vol. 51 of *SUSSP Proceedings*, NATO ASI, Institute of Physics Publishing, pp. 211–237.
- [23] BUCK, B., AND MACAULAY, V. A., Eds. *Maximum Entropy in Action*. Clarendon Press, Oxford, 1991.
- [24] CAHN, R. N., AND GOLDHABER, G. *The Experimental Foundations of Particle Physics*. Cambridge University Press, Cambridge, 1989.
- [25] CERN. *Cyclotron Handbook*. Genève, 1976.
- [26] CERN. Physics Analysis Workstation – PAW, September 2000. <http://wwwinfo.cern.ch/asd/paw/>.
- [27] CHAPPERT, J., AND GRYSZPAN, R. I., Eds. *Muons and Pions in Materials Research*. North-Holland, Amsterdam, 1984.
- [28] CHIA, V. K. F., MOUNT, G. R., EDGELL, M. J., AND MAGEE, C. W. Recent advances in secondary ion mass spectrometry to characterize ultralow energy ion implants. *Journal of Vacuum Science & Technology B* 17, 5 (September 1999), 2345–2351.
- [29] CORLETT, J. N., LI, D., MACGILL, R. A., GREEN, M., TURNER, W. C., HARTMAN, N., HOLTKAMP, N., MORETTI, A., KIRK, H., PALMER, R. B., ZHAO, Y., AND SUMMERS, D. RF accelerating structures for the muon cooling experiment. In *Proceedings of the 1999 Particle Accelerator Conference* (Piscataway, New Jersey, 1999), IEEE, Ed., vol. 5, pp. 3149–3151.
- [30] COTTINGHAM, W. M., GREENWOOD, D. A., AND COTTINGHAM, W. N. *Introduction to the Standard Model of Particle Physics*. Cambridge University Press, Cambridge, January 1999.
- [31] COTTRELL, S. P., COX, S. F. J., LORD, J. S., AND SCOTT, C. A. Radio-Frequency  $\mu$ SR Experiments at the ISIS Pulsed Muon Facility. *Applied Magnetic Resonance* 15, 3-4 (1998), 469–476.
- [32] COX, S. F. J. Implanted Muon Studies in Condensed Matter Science. *Journal of Physics C: Solid State Physics* 20 (1987), 3187.
- [33] COX, S. F. J., DE RENZI, R., HARTMANN, O., AND BUCCI, C. Muon spectroscopy in solid-state, atomic and molecular physics: Considerations for a facility at the spallation neutron source. Tech. Rep. RAL-TR-83-015, Rutherford Appleton Laboratory, 1983.

- [34] DE CECCO, P., HAUSER, P., HORVÁTH, D., KOTTMANN, F., MISSIMER, J., SIMONS, L. M., TAQQU, D., ABBOT, D., BACH, B., SIEGEL, R. T., AND VIEL, D. Low-energy  $\mu^-$  beam from the PSI anticyclotron. *Hyperfine Interactions* 76, 1-4 (April 1993), 275–280.
- [35] DE CECCO, P., HAUSER, P., HORVÁTH, D., KOTTMANN, F., SIMONS, L. M., AND TAQQU, D. A new method to produce a negative muon beam of keV energies. *Nuclear Instruments and Methods in Physics Research A* 394, 3 (July 1997), 287–294.
- [36] DE RENZI, R.  $\mu$ SR and NMR: fundamental concepts and selected examples. In *Muon Science: Muons in Physics, Chemistry and Materials* (Bristol and Philadelphia, 1999), S. L. Lee, S. H. Kilcoyne, and R. Cywinski, Eds., vol. 51 of *SUSSP Proceedings*, NATO ASI, Institute of Physics Publishing, pp. 211–237.
- [37] DELCHAR, T. A. *Vacuum physics and techniques*. No. 6 in *Physics and its applications*. Chapman and Hall, London, 1993.
- [38] DICKSON, W. R. *Maximum Entropy Signal Analysis (MESA) User Manual*. CLRC, 1996.
- [39] EATON, G. H. The ISIS Pulsed Muon Facility. In *Lecture Notes from the Training Course in Pulsed  $\mu$ SR Techniques* (March 1996), S. H. Kilcoyne, Ed., Rutherford Appleton Laboratory. Tech. Rep. RAL-TR-96-007.
- [40] EATON, G. H. Muon facilities and experiments: now and in the new millennium. Tech. Rep. RAL-TR-98-019, Rutherford Appleton Laboratory, August 1998.
- [41] EATON, G. H., CARNE, A., COX, S. F. J., DAVIES, J. D., DE RENZI, R., HARTMANN, O., KRATZER, A., RISTORI, C., SCOTT, C. A., STIRLING, G. S., AND SUNDQVIST, T. Commissioning of the Rutherford Appleton Laboratory Pulsed Muon Facility. *Nuclear Instruments and Methods in Physics Research A* 269 (1988), 483.
- [42] EATON, G. H., CLARKE-GAYTHER, M. A., SCOTT, C. A., UDEN, C. N., AND WILLIAMS, W. G. Fast E-field switching of a pulsed surface muon beam: the commissioning of the European Muon Facility at ISIS. *Nuclear Instruments & Methods in Physics Research, A* 342, 2-3 (March 1994), 319–331.
- [43] EATON, G. H., SCOTT, C. A., AND WILLIAMS, W. G. Development of the pulsed muon facility at ISIS. *Hyperfine Interactions* 87, 1-4 (1994), 1099–1104.
- [44] ECHENIQUE, P. M., FLORES, F., AND RITCHIE, R. H. Dynamic screening of ions in condensed matter. In *Solid State Physics*, H. Ehrenreich and D. Turnbull, Eds., vol. 43. Academic Press, Inc., New York, 1990, ch. 3, pp. 229–308.
- [45] FEYNMAN, R. P., LEIGHTON, R. B., AND SANDS, M. *The Feynman Lectures on Physics*, vol. 2: Electromagnetism and Matter. Addison-Wesley, New York, 1984, ch. 29-4.
- [46] FEYNMAN, R. P., LEIGHTON, R. B., AND SANDS, M. *The Feynman Lectures on Physics*, vol. 3: Quantum Mechanics. Addison-Wesley, New York, 1984, ch. 12.
- [47] FORD, G. W., AND MULLIN, C. J. Scattering of polarized Dirac particles on electrons. *Physical Review* 108 (1957), 477.
- [48] GAO, R. S., GIBNER, P. S., NEWMAN, J. H., SMITH, K. A., AND STEBBINGS, R. F. Absolute and angular efficiencies of a microchannel-plate position-sensitive detector. *Review of Scientific Instruments* 55, 11 (November 1984), 1756–1759.
- [49] GARWIN, R. L., LEDERMANN, L. M., AND WEINRICH, M. Observations of the failure of parity and charge conjugation in meson decays: the magnetic moment of the free muon. *Physical Review* 105 (January 15 1957), 1415–1417.
- [50] GLÜCKLER, H., MORENZONI, E., PROKSCHA, T., BIRKE, M., FORGAN, E. M., HOFER, A., JACKSON, T. J., LITTERST, J., LUETKENS, H., NIEDERMAYER, C., PLEINES, M., RISEMAN, T. M., AND SCHATZ, G. Range studies of low-energy muons in a thin Al film. *Physica B* 289-290 (2000), 658–661.

- [51] GONIN, M., KALLENBACH, R., AND BOCHSLER, P. Charge exchange of hydrogen atoms in carbon foils at 0.4–120 keV. *Review of Scientific Instruments* 65, 3 (March 1994), 648–652.
- [52] GROOM, D. E., AND ET AL. Review of particle properties. *The European Physical Journal C* 15 (2000), 1.
- [53] GROTZ, K., AND KLAPDOR, H. V. *The Weak Interaction in Nuclear, Particle and Astrophysics*. Adam Hilger, Bristol, 1990.
- [54] GROUP, A. S. *MINUIT – Function Minimization and Error Analysis (Reference Manual)*. CERN, Genève, 1992.
- [55] GULLIKSON, E. M., AND MILLS, A. P. Positron dynamics in rare-gas solids. *Physical Review Letters* 57, 3 (July 1986), 376–379.
- [56] HARSHMAN, D. R., MILLS JR., A. P., BEVERIDGE, J. L., KENDALL, K. R., MORRIS, G. D., SENBA, M., WARREN, J. B., RUPAAL, A. S., AND TURNER, J. H. Generation of slow positive muons from solid rare-gas moderators. *Physical Review B* 36, 16 (December 1987), 8850–8853.
- [57] HARSHMAN, D. R., WARREN, J. B., BEVERIDGE, J. L., KENDALL, K. R., KIEFL, R. F., ORAM, C. J., MILLS JR., A. P., CRANE, W. S., RUPAAL, A. S., AND TURNER, J. H. Observation of low-energy  $\mu^+$  emission from solid surfaces. *Physical Review Letters* 56, 26 (June 1986), 2850–2853.
- [58] HARTMANN, O., NORLIN, L. O., YAOUANC, A., LE HERICY, J., KARLSSON, E., AND NINIKOSKI, T. O. Low temperature studies of muon localization in copper. *Hyperfine Interactions* 8, 4-6 (1981), 533–538.
- [59] HEITLINGER, K., BACHER, R., BADERTSCHER, A., BLÜM, P., EADES, L., EGGER, J., ELSENER, K., GOTTA, D., MORENZONI, E., AND SIMONS, L. M. Precision measurement of antiprotonic hydrogen and deuterium X-rays. *Zeitschrift für Physik A* 342, 3 (1992), 359–368.
- [60] HUGHES, V., AND ZU PUTLITZ, G. Muonium. In *Quantum electrodynamics*, T. Kinoshita, Ed., vol. 7 of *Advanced series on directions in high energy physics*. World Scientific Press, Singapore, 1990.
- [61] JACKSON, T. J., RISEMAN, T. M., FORGAN, E. M., GLUCKLER, H., PROKSCHA, T., MORENZONI, E., PLEINES, M., NIEDERMAYER, C., SCHATZ, G., LUETKEUS, H., AND LITTERST, J. Depth-resolved profile of the magnetic field beneath the surface of a superconductor with a few nm resolution. *Physical Review Letters* 84, 21 (May 2000), 4958–4961.
- [62] JAMES, F., AND ROOS, M. Minuit—a system for function minimization and analysis of the parameter errors and correlations. *Computer Physics Communications* 10, 6 (December 1975), 343–367.
- [63] KALLENBACH, R., GONIN, M., BÜRGI, A., AND BOCHSLER, P. Charge exchange of hydrogen ions in carbon foils. *Nuclear Instruments & Methods in Physics Research B* 83, 1-2 (October 1993), 68–72.
- [64] KALOS, M. H., AND WHITLOCK, P. A. *Monte Carlo Methods: Basics*, vol. 1. John Wiley & Sons, Inc., New York, October 1986.
- [65] KANE, G. *Modern Elementary Particle Physics: The Fundamental Particles and Forces*. Perseus Press, New York, April 1993.
- [66] KAPLAN, N., KREITZMAN, S. R., SCHNEIDER, J. W., BREWER, J. H., AND HITTI, B. Non-resonant zeugmatography with muons ( $\mu$ SI) and radioactive isotopes. *Hyperfine Interactions* 87, 1-4 (1994), 1031–1041.
- [67] KARLSSON, E. B. *Solid State Phenomena: As Seen by Muons, Protons, and Excited Nuclei*. Clarendon Press, Oxford, 1995.

- [68] KILCOYNE, S. H. Lecture notes from the training course in pulsed  $\mu$ SR techniques. Tech. Rep. RAL-TR-96-007, Rutherford Appleton Laboratory, March 1996.
- [69] KLEIN, M. L., AND VENABLES, J. A., Eds. *Rare Gas Solids*, vol. 1. Academic Press, Inc., New York, 1976.
- [70] KOST, C. J., AND JONES, F. W. *RELAX3D User's Guide and Reference Manual*, 3<sup>rd</sup> ed. TRIUMF, Vancouver, B.C., Canada, January 1992.
- [71] KREITZMAN, S. R., WILLIAMS, D., KAPLAN, N., KEMPTON, J. R., AND BREWER, J. H. Spin echoes for  $\mu^+$ -spin spectroscopy. *Physical Review Letters* 61, 25 (December 1988), 2890–2893.
- [72] KUANG, Y., ARNOLD, K. P., CHMELY, F., ECKHAUSE, M., HUGHES, V. W., KANE, J. R., KETTELL, S., KIM, D. H., KUMAR, K., LU, D. C., MATTHIAS, B., NI, B., ORTH, H., ZU PUTLITZ, G., SCHAEFER, H. R., SOUDER, P. A., AND WOODLE, K. Formation of the negative muonium ion and charge-exchange processes for positive muons passing through thin metal foils. *Physical Review A* 39, 12 (June 1989), 6109–6123.
- [73] KUNO, Y., AND OKADA, Y. Muon decays and physics beyond the standard model. *Reviews of Modern Physics* 73 (January 2001), 151–202.
- [74] KUNZE, P. Untersuchung der Ultrastrahlung in der Wilsonkammer. *Zeitschrift für Physik* 83 (1933), 1–18.
- [75] LANDAU, D. P., AND BINDER, K. *A Guide to Monte Carlo Simulations in Statistical Physics*. Cambridge University Press, Cambridge, May 2000.
- [76] LANDAU, L. D., AND LIFSHITZ, E. M. *Quantum Mechanics. Non-Relativistic Theory*, vol. 3 of *Course of Theoretical Physics*. Pergamon Press, London, 1958.
- [77] LATTES, C. M. G., MUIRHEAD, H., POWELL, C. F., AND OCCHIALINI, G. P. Processes involving charged mesons. *Nature* 159 (May 1947), 694–697.
- [78] LAUTERBUR, P. C. Image formation by induced local interactions: Examples employing nuclear magnetic resonance. *Nature* 242 (1973), 190.
- [79] LEO, W. R. *Techniques for Nuclear and Particle Physics Experiments*, 2<sup>nd</sup> ed. Springer Verlag, Berlin, March 1994.
- [80] LINDHARD, J., NIELSEN, V., AND SCHARFF, M. Approximation method in classical scattering by coulomb fields. *Matematisk-Fysiske Meddelelser (Kongelige Danske Videnskabernes Selskab)* 38, 10 (1968).
- [81] MAGEE, C. W., COHEN, S. A., VOSS, D. E., AND BRICE, D. K. Depth distributions of low energy deuterium implanted into silicon as determined by SIMS. *Nuclear Instruments and Methods* 168, 1-3 (January 1980), 383–387.
- [82] MANDL, F., AND SHAW, G. *Quantum Field Theory*, Revised ed. John Wiley & Sons Inc., New York, 1993.
- [83] MARTIN, B. R., AND SHAW, G. *Particle Physics*, 2<sup>nd</sup> ed. John Wiley & Sons Ltd., Chichester, 1997.
- [84] MARTYN, H. U. Test of QED by High Energy Electron-positron Collisions. In *Quantum electrodynamics*, T. Kinoshita, Ed., vol. 7 of *Advanced series on directions in high energy physics*. World Scientific Press, Singapore, 1990, p. 92.
- [85] MAYER, M., AND ECKSTEIN, W. Monte Carlo calculations of hydrogen and deuterium range distributions in light target materials. *Nuclear Instruments & Methods in Physics Research B* 94, 1-2 (October 1994), 22–26.
- [86] MERKEL, J. *Development of an Ultraslow Polarized Muon Beam*. Dissertation, Ruprecht Karls Universität, Heidelberg, June 1998.

- [87] MESSIAH, A. *Mécanique quantique*, vol. 2. Dunod, Paris, 1959-1960.
- [88] MILLS JR., A. P., AND GULLIKSON, E. M. Solid neon moderator for producing slow positrons. *Applied Physics Letters* 49, 17 (October 1986), 1121-1123.
- [89] MILLS JR., A. P., IMAZATO, J., SAITOH, S., UEDONO, A., KAWASHIMA, Y., AND NAGAMINE, K. Generation of thermal muonium in vacuum. *Physical Review Letters* 56, 14 (April 1986), 1463-1466.
- [90] MØGENSEN, O. E. Spur reaction model of positronium formation. *Journal of Chemical Physics* 60, 3 (February 1974), 998-1004.
- [91] MØGENSEN, O. E., AND PERCIVAL, P. W. Muonium formation in nonpolar liquids. *Radiation Physics and Chemistry* 28, 1 (1986), 85-89.
- [92] MÖHL, D., PETRUCCI, G., THORNDahl, L., AND VAN DER MEER, S. Physics and technique of stochastic cooling. *Physics Reports* 58 (1980), 73-119.
- [93] MORENZONI, E. Very slow positive muons. *Zeitschrift für Physik C* 56 (1992), 243.
- [94] MORENZONI, E. Low-energy muons as probes of thin films and surfaces. *Applied Magnetic Resonance* 13, 1-2 (1997), 219-229.
- [95] MORENZONI, E. Physics and applications of low energy muons. In *Muon Science: Muons in Physics, Chemistry and Materials* (Bristol and Philadelphia, 1999), S. L. Lee, S. H. Kilcoyne, and R. Cywinski, Eds., vol. 51 of *SUSSP Proceedings*, NATO ASI, Institute of Physics Publishing, pp. 343-404.
- [96] MORENZONI, E., KOTTMANN, F., MADEN, D., MATTHIAS, B., MEYBERG, M., PROKSCHA, T., WUTZKE, T., AND ZIMMERMANN, U. Generation of very slow polarized positive muons. *Physical Review Letters* 72, 17 (25 April 1994), 2793-2796.
- [97] MORENZONI, E., PROKSCHA, T., HOFER, A., MEYBERG, M., WUTZKE, T., BIRKE, M., GLÜCKLER, H., LITTERST, J., NIEDERMAYER, C., AND SCHATZ, G. Characteristics of condensed gas moderators for the generation of very slow polarized muons. PSI Report PR-96-37, Paul Scherrer Institut, Villigen, Switzerland, November 1996.
- [98] MORGAN, J. The Antiproton Source Rookie Book - Chapter 5: Stochastic cooling, September 2000, Fermilab, Batavia (IL), USA. [http://www-bdnew.fnal.gov/operations/rookie\\_books/Pbar\\_Rookie\\_Book.pdf](http://www-bdnew.fnal.gov/operations/rookie_books/Pbar_Rookie_Book.pdf).
- [99] MORRIS, G. D. Epithermal muons from solid rare-gas moderators. Master's thesis, University of British Columbia, Vancouver, BC, 1990.
- [100] MÜHLBAUER, M., DANIEL, H., HARTMANN, F. J., HAUSER, P., KOTTMANN, F., MEIERL, C., MARKUSHIN, V., PETIJEAN, C., SCOTT, W., TAQQU, D., AND WOJCIECHOWSKI, P. Frictional cooling: latest experimental results and first application. *Nuclear Instruments & Methods in Physics Research B A* 51 (November 1996), 135-142.
- [101] NAGAMINE, K., MIYAKE, Y., SHIMOMURA, K., BIRRER, P., MARANGOS, J. P., IWASAKI, M., STRASSER, P., AND KUGA, T. Ultraslow positive-muon generation by laser ionization of thermal muonium from hot tungsten at primary proton beam. *Physical Review Letters* 74, 24 (June 12 1995), 4811-4814.
- [102] NEDDERMEYER, S. H., AND ANDERSON, C. D. Note on the Nature of Cosmic-Ray Particles. *Physical Review* 51 (1937), 884-886.
- [103] NICHOLS, D. K., AND VAN LINT, V. A. J. Energy Loss and Range of Energetic Neutral Atoms in Solids. In *Solid State Physics*, H. Ehrenreich and D. Turnbull, Eds., vol. 18. Academic Press, Inc., New York, 1966, ch. 1, pp. 1-54.

- [104] NISHIDA, N., NAGAMINE, K., HAYANO, R. S., YAMAZAKI, T., FLEMING, D., DUNCAN, R., BREWER, J., AHKTAR, A., AND YASUOKA, H. The local magnetic fields probed by  $\mu^+$  in HCP ferromagnets: Co and Gd. *Journal of the Physical Society of Japan* 44, 4 (April 1978), 1131–1141.
- [105] NOAKES, D. R., BREWER, J. H., HARSHMAN, D. R., ANSALDO, E. J., AND HUANG, C. Y. Electron, muon, and nuclear spin dynamics in  $\text{SmRh}_4\text{B}_4$  and  $\text{ErRh}_4\text{B}_4$ . *Physical Review B* 35, 13 (May 1 1987), 6597–6607.
- [106] OEN, O. S., AND ROBINSON, M. T. Computer studies of the penetration depth of low-energy light ions in solids. In *Applications of ion beams to materials* (London, 1976), Institute of Physics, pp. 329–333.
- [107] OKUN, L. B. *Weak Interactions of Elementary Particles*. Pergamon Press, Oxford, 1965.
- [108] PACHL, B. J. Anwendungen gepulster polarisierter langsamer Myonen. Diplomarbeit, Ruprecht Karls Universität, Heidelberg, 1999.
- [109] PALMER, R. B. Muon collider: introduction and status. In *AIP Conference Proceedings* (1998), AIP, Ed., vol. 435, pp. 11–36.
- [110] PARTICLE DATA GROUP. Leptons – 2000 update, 20 August 2000. <http://pdg.lbl.gov/2000-lxxx.html>.
- [111] PERCIVAL, P. W., WALKER, D. C., JEAN, Y. C., AND FLEMING, D. C. The time-scale of intraspur muonium formation. *Journal of Chemical Physics* 72, 4 (February 1980), 2902–2904.
- [112] PIFER, A. E., BOWEN, T., AND KENDALL, K. R. A high stopping density  $\mu^+$  beam. *Nuclear Instruments and Methods in Physics Research* 135 (1976), 39.
- [113] PÓCSIK, I., VÁZSONYI, B. É., AND KOÓS, M., Eds. *Proceedings of the International Conference on Complex Geometry in Nature* (Budapest, 1993).
- [114] PROKSCHA, T. *Erzeugung niederenergetischer, polarisiert Myonen und von Myonium an dünnen, gefrorenen Edelgas- und Stickstoffschichten*. Dissertation, Ruprecht Karls Universität, Heidelberg, 1995.
- [115] PURCELL, E. M. *Berkeley Physics Course (Electricity and Magnetism)*, vol. 2. McGraw-Hill, New York, 1963, p. 207.
- [116] RAINFORD, B. D. Aspects of data treatment for transverse  $\mu\text{SR}$ . In *Lecture Notes from the Training Course in Pulsed  $\mu\text{SR}$  Techniques* (March 1996), S. H. Kilcoyne, Ed., Rutherford Appleton Laboratory. Tech. Rep. RAL-TR-96-007.
- [117] RAINFORD, B. D., AND DANIELL, G. J.  $\mu\text{SR}$  frequency spectra using the maximum entropy method. *Hyperfine Interactions* 87, 1-4 (1994), 1129–1134.
- [118] RINDLER, W. *Introduction to Special Relativity*, 2<sup>nd</sup> ed. Clarendon Press, Oxford, July 1991.
- [119] RISEMAN, T. M., BREWER, J. H., AND ARSENEAU, D. J. Corrected asymmetry plots. *Hyperfine Interactions* 87, 1-4 (1994), 1135–1140.
- [120] RITCHIE, R. H. Interaction of charged particles with a degenerate Fermi-Dirac electron gas. *Physical Review* 114 (1959), 644.
- [121] ROBINSON, P. D. Hypervirial theorems and perturbation theory in quantum mechanics. *Proc. R. Soc. London* 283 (1965), 229–237.
- [122] ROSS, G. G., AND TERREAU, B. M. ERD Measurement of the Mean Ranges and Variances of 0.75–2.0 keV Deuterium Ions in Be, C and Si. *Nuclear Instruments & Methods in Physics Research B* 45 (1990), 190.
- [123] ROSSI, B., AND HALL, D. B. Variation of the Rate of Decay of Mesotrons with Momentum. *Physical Review* 59 (February 1941), 223–228.

- [124] SCHECK, F. Muon physics. *Physics Reports* 44, 4 (August 1978), 187–248.
- [125] SCHENCK, A. *Muon Spin Rotation Spectroscopy: Principles and Applications in Solid State Physics*. Adam Hilger, Bristol, 1985.
- [126] SCHNEIDER, M., BACHER, R., BLÜM, P., GOTTA, D., HEITLINGER, K., KUNOLD, W., ROHMANN, D., EGGER, J., SIMONS, L. M., AND ELSENER, K. X-rays from antiprotonic  $^3\text{He}$  and  $^4\text{He}$ . *Zeitschrift für Physik A* 338, 2 (1991), 217–222.
- [127] SCHOTT, M., DANIEL, H., HARTMANN, F. J., AND NEUMANN, W. Measurement of the stopping power of Au and  $\text{MgF}_2$  for slow muons. *Zeitschrift für Physik A* 346 (1993), 81.
- [128] SCHREIDER, Y. A., Ed. *The Monte Carlo Method: The Method of Statistical Trials*. Pergamon Press Ltd., Oxford, 1966.
- [129] SCHULTZ, P. J., AND LYNN, K. G. Interaction of positrons beams with surfaces, thin films, and interfaces. *Reviews of Modern Physics* 60, 3 (July 1988), 701–779.
- [130] SENBA, M. Charge exchange collisions in gases in the presence of competing processes. *Journal of Physics B (Atomic, Molecular and Optical Physics)* 21, 18 (September 1988), 3093–3111.
- [131] SENBA, M. Charge exchange collisions in the presence of competing processes: an integral equation approach. *Journal of Physics B (Atomic, Molecular and Optical Physics)* 22, 12 (June 1989), 2027–2040.
- [132] SHIROKA, T. Studi sulla Produzione dei Muoni Epitermici: Indagini Preliminari e Prospettive per le Applicazioni in LE- $\mu\text{SR}$ . Tesi di Laurea, Università degli Studi di Parma, Parma, 1997.
- [133] SHIROKA, T., BUCCI, C., DE RENZI, R., GALLI, F., GUIDI, G., EATON, G. H., KING, P. J. C., AND SCOTT, C. A. Synchronous pulsed magnetic fields in muon spin rotation. *Physica B* 289 (August 2000), 684–688.
- [134] SHIROKA, T., BUCCI, C., DE RENZI, R., GUIDI, F. G. G., EATON, G. H., KING, P. J. C., AND SCOTT, C. A. Polarized muon spins in pulsed magnetic fields: a new method to study delayed muonium formation. *Physical Review Letters* 83, 21 (November 1999), 4405–4408.
- [135] SHIROKA, T., BUCCI, C., DE RENZI, R., GUIDI, G., EATON, G. H., KING, P. J. C., AND SCOTT, C. A. Studies of range and straggling of muons in metals by the Projected Range Imaging (PRI) technique. *Nuclear Instruments & Methods* 152, 2-3 (May 1999), 241–251.
- [136] SIEBBELES, L. D. A., PIMBLOTT, S. M., AND COX, S. F. J. Simulation of muonium formation in liquid hydrocarbons. *Journal of Chemical Physics* 111, 16 (October 1999), 7493–7500.
- [137] SIGG, D., BADERTSCHER, A., BOGDAN, M., GOUDSMIT, P. F. A., LEISI, H. J., MATSINOS, E., SCHRÖDER, H.-C., ZHAO, Z. G., CHATELLARD, D., EGGER, J.-P., JEANNET, E., ASCHENAUER, E. C., GABATHULER, K., SIMONS, L. M., AND RUSI EL HASSANI, A. J. Strong interaction shift and width of the 1s level in pionic hydrogen. *Physical Review Letters* 75, 18 (October 1995), 3245–3248.
- [138] SIMONS, L. M. Die zyklotronfalle. *Physikalische Blätter* 48 (1992), 261.
- [139] SLICHTER, C. P. *Principles of Magnetic Resonance*, 3<sup>rd</sup> ed. No. 1 in Springer series in solid-state sciences. Springer Verlag, Berlin, 1990.
- [140] SQUIRES, G. L. *Practical Physics*, 3<sup>rd</sup> ed. Cambridge University Press, Cambridge, 1985.
- [141] STERNHEIMER, R. M. Interaction of radiation with matter. In *Methods of Experimental Physics*, L. C. L. Yuan and C. S. Wu, Eds., vol. 5A. Academic Press, Inc., New York, 1961, ch. 1.1, pp. 1–89.
- [142] STORCHAK, V., BREWER, J. H., AND MORRIS, G. D. Fast and slow electrons in liquid neon. *Physical Review Letters* 76, 16 (April 1996), 2969–2972.

- [143] STORCHAK, V., BREWER, J. H., MORRIS, G. D., ARSENEAU, D. J., AND SENBA, M. Muonium formation via electron transport in solid nitrogen. *Physical Review B* 59, 16 (April 1999), 10559–10572.
- [144] STORCHAK, V., COX, S. F. J., COTTRELL, S. P., BREWER, J. H., MORRIS, G. D., ARSENEAU, D. J., AND HITTI, B. Muonium formation via electron transport in silicon. *Physical Review Letters* 78, 14 (April 1997), 2835–2838.
- [145] SYDENHAM, P. H., Ed. *Handbook of Measurement Science (Theoretical Fundamentals)*, vol. 1. John Wiley & Sons Ltd, New York, 1982.
- [146] TAQQU, D. Phase space compression of muon beams. *Nuclear Instruments & Methods in Physics Research A* 247, 2 (15 June 1986), 288–300.
- [147] TAQQU, D. Frictional accumulation of negative muons and its application. *Hyperfine Interactions* 102 (1996), 633–640.
- [148] TRÄGER, K. *Development of a Slow Polarized Muon Beam at the Rutherford Appleton Laboratory*. Dissertation, Ruprecht Karls Universität, Heidelberg, February 1999.
- [149] TRÄGER, K., BREITRUCK, A., TRIGO, M. D., GROSSMANN, A., JUNGMANN, K., MERKEL, J., MEYER, V., NEUMAYER, P., PACHL, B., ZU PUTLITZ, G., SANTRA, R., WILLMANN, L., ALLODI, G., BUCCI, C., GALLI, F., GUIDI, G., SHIROKA, T., EATON, G. H., KING, P. J. C., SCOTT, C. A., WILLIAMS, W. G., RODUNER, E., SCHEUERMANN, R., CHARLTON, M. C., DONNELLY, P., PARETI, L., AND TURILLI, G. Production of pulsed ultra slow muons and first  $\mu$ SR experiments on thin metallic and magnetic films. *Physica B* 289 (August 2000), 662–665.
- [150] TRIUMF.  $\mu$ SR facilities, August 2000. [http://musr.org/musr\\_facilities.html](http://musr.org/musr_facilities.html).
- [151] TROWER, W. P. Range-momentum and  $dP/dx$  plots of charged particles in matter. LBL Report No. UCRL-2426, Vol.4, July 1966.
- [152] VOLINO, F. Spins: Larmor precession, linewidth, relaxation. In *Muons and Pions in Materials Research*, J. Chappert and R. I. Grynspan, Eds. North-Holland, Amsterdam, 1984.
- [153] WALKER, D. C. *Muon and Muonium Chemistry*. Cambridge University Press, Cambridge, 1983.
- [154] WIEDEMANN, H. *Particle Accelerator Physics II: Nonlinear and Higher-Order Beam Dynamics*, 2<sup>nd</sup> ed., vol. 2. Springer Verlag, September 1998.
- [155] WIEDEMANN, H. *Particle Accelerator Physics I: Basic Principles and Linear Beam Dynamics*, 2<sup>nd</sup> ed., vol. 1. Springer Verlag, April 1999.
- [156] YAMAZAKI, T., NAKAI, K., AND NAGAMINE, K., Eds. *Perspectives of Meson Science*. Elsevier, Amsterdam, 1992.
- [157] YUKAWA, H. On the Interaction of Elementary Particles. *Proc. Phys.-Math. Soc. Japan* 17 (1935), 48.
- [158] ZIEGLER, J. F. The Stopping and Range of Ions in Matter (SRIM-2000), 20 August 2000. <http://www.SRIM.org/>.
- [159] ZIEGLER, J. F., BIERSACK, J. P., AND LITTMARK, U. *The Stopping and Range of Ions in Matter*, vol. 2-6. Pergamon Press, New York, 1977-1985.
- [160] ZIEGLER, J. F., BIERSACK, J. P., AND LITTMARK, U. *The Stopping and Range of Ions in Solids*, 2<sup>nd</sup> ed., vol. 1. Pergamon Press, New York, 1996.

# Acknowledgements

I would like to express my thanks to my advisor, Prof. Cesare Bucci, for his continuous support and guidance throughout this work and for providing me the opportunity to work on the challenging project on Slow Muon production.

I am grateful to all the members of the NMR –  $\mu$ SR group of Parma: Dr G. Allodi, Prof. R. De Renzi co-advisor of the present thesis, F. Galli, Prof. G. Guidi and Dr M. Riccò for the friendly atmosphere and many helpful discussions.

It was a pleasure to work with the members of the *Myongruppe* of Universität Heidelberg: Dr K. Träger, A. Breitrück, M. Diaz Trigo, Dr A. Grossmann, Prof. K.P. Jungmann, Dr J. Merkel, Dr V. Meyer, P. Neumayer, B. Pachl, Prof. G. zu Putlitz, Dr I. Reinhard, R. Santra and Dr L. Willmann, as well as with the rest of the collaboration: Dr M. Charlton, Prof. S.F.J. Cox, P. Donnelly, Prof. E. Roduner, Dr R. Scheuermann and Dr W.G. Williams. I do acknowledge the efforts and the commitment of all of them, which were decisive in the success of this work.

The permission to reproduce some of the original diagrams of the slow muon apparatus and of its components is kindly acknowledged to K. Träger and J. Merkel.

I take the opportunity to thank also the *instrument scientists* of ISIS Pulsed Muon Facility at the Rutherford Appleton Laboratory, as well as members of the collaboration: Dr G.H. Eaton, Dr P.J.C. King and Dr C.A. Scott for the excellent technical support during all the stages of the experiments.

Finally, special thanks go to Prof. P. Podini and Mr G. Lenzi for helpful suggestions during the design and test of the switching device and to Dr L. Pareti and Dr G. Turilli of the MASPEC Institute for kindly providing us with samples.

# Publication list

- T. Shiroka, C. Bucci, R. De Renzi, G. Guidi, G.H. Eaton, P.J.C. King, C.A. Scott, “Studies of Range and Stragglings of Muons in Metals through the Projected Range Imaging (PRI) Technique”, Nucl. Instr. and Methods **B 152**, (2–3) (1999), 241-251.
- T. Shiroka, C. Bucci, R. De Renzi, F. Galli, G. Guidi, G.H. Eaton, P.J.C. King, C.A. Scott, “Polarized Muon Spins in Pulsed Magnetic Fields: A New Method to Study Delayed Muonium Formation”, Phys. Rev. Letters, **83**, (1999), 4405-4408.
- R. De Renzi and T. Shiroka, “Muons at ISIS”, Notiziario Neutroni & Luce di Sincrotrone **4**, (1999) 23-30.
- T. Shiroka, C. Bucci, R. De Renzi, F. Galli, G. Guidi, G.H. Eaton, P.J.C. King and C.A. Scott, “Synchronous pulsed magnetic fields in muon spin rotation”, Physica B: Condensed Matter, **289-290** (1–4), (2000) 684-688.
- K. Träger et al., “Production of pulsed ultra slow muons and first  $\mu$ SR experiments on thin metallic and magnetic films”, Physica B: Condensed Matter, **289-290** (1–4), (2000) 662-665.
- T. Shiroka, C. Bucci, R. De Renzi, F. Galli, G. Guidi, G.H. Eaton, P.J.C. King, C.A. Scott, “Muon Spin Rotation ( $\mu$ SR) with pulsed sources: Fundamental and application oriented aspects of synchronous pulsed magnetic fields”, Appl. Magn. Reson. **19** (3–4), (2000).
- T. Shiroka et al., “Production of pulsed ultra slow muons and first  $\mu$ SR experiments on thin metallic and magnetic Films”, Appl. Magn. Reson. **19** (3–4), (2000).
- M. Riccò, T. Shiroka, A. Sartori, F. Bolzoni, “Weak type II superconductivity in  $(\text{NH}_3)_x\text{NaK}_2\text{C}_{60}$ ”, in Proceedings of the 197<sup>th</sup> Meeting of The Electrochemical Society, Toronto, May 14–18, 2000.
- M. Tomaselli, B.H. Meier, M. Riccò, T. Shiroka, A. Sartori, “A  $^7\text{Li}$  multiple-quantum and  $^{13}\text{C}$  NMR study of interstitial Li clusters in  $\text{Li}_x\text{C}_{60}$ ”, submitted to Phys. Rev. B.
- M. Riccò, T. Shiroka, A. Sartori, F. Bolzoni, “Weak type II superconductivity in  $(\text{NH}_3)_x\text{NaK}_2\text{C}_{60}$ ”, submitted to Europhysics Letters.